Doctoral Dissertation
Doctoral Program in Electrical, Electronics and Communication Engineering
(36^{th}cycle)

Memristive devices based on NbO$_\text{x}$

Giuseppe Leonetti

******

Supervisor(s):
Prof. Fabrizio Candido Pirri, Supervisor
Dr. Gianluca Milano, Co-Supervisor
Dr. Natascia De Leo, Co-Supervisor

Doctoral Examination Committee:
Prof. Enrique Miranda, Referee, Universidad Autònoma de Barcelona (UAB), Barcelona, Spain.
Prof. Dr.-Ing. Stefan Tappertzhofen, Referee, TU Dortmund University, Dortmund, Germany
Dr. Luca Boarino, Istituto Nazionale di Ricerca Metrologica (INRiM), Turin, Italy
Prof. Andrea Lamberti, Politecnico di Torino, Turin, Italy
Prof. Samuele Porro, Politecnico di Torino, Turin, Italy

Politecnico di Torino
July 26, 2024

Declaration

I hereby declare that, the contents and organization of this dissertation constitute my own original work and does not compromise in any way the rights of third parties, including those relating to the security of personal data.

<div align="right">

Giuseppe Leonetti

July 26, 2024

</div>

I would like to dedicate this thesis to my loving family

Acknowledgements

I would like to dedicate this short part of the thesis to express my sincere acknowledgments to whom supported me during these years.

First of all, I would like to thanks my family, especially for the economical support, essential to live in a big city like Turin, in which the cost of life are increasing year by year.

A big thanks should go to my friends Elena and Alessandra, for the emotional support without which probably I would not be able to face these years of difficulties.

Another big thank should go to Tiziano, one of my best friend for the years spent here in Turin, with which I shared both the happy and the sad moments: thanks for make me laugh everyday even when things go wrong.

I would like to thank Federico, Asia, Alessandro, Angelica, Gianmarco and Roberto for the happy moments shared together and for having endured me in my craziness moments.

I would like to thank Simone for being my healthy guide and thank to which I was able to conciliate work and physical activity, essential to break the every day life stress.

I would like to thank Annalisa, Giannicola and Maddalena for the brief but happy moments spent together in this years when I was not coming to much often at home, It always make me happy to see you have always pleasure into see me.

I would like to acknowledge my academic tutor, Professor Candido Fabrizio Pirri, for his invaluable supervision and support during the course of my PhD degree. It is worth to acknowledge my family in INRiM, in particular my tutors Natascia and Gianluca that always sustained me. I would like to thank Matteo for the having taught me all that I know in the fabrication. I would like to thank my colleagues and ex-colleagues Ivan, Irdi, Marwan, Nicoletta,

Abstract

With the Moore's Law coming to an end, the continuous growth of data in the era of Internet of Things requires the development of new technologies to overcome Von Neumann bottleneck that limits current computing technologies. In this framework, memristive devices in form of Redox Random Access Memories (ReRAMs) have recently attracted great attention for the development of next-generation memory storage and for the in-memory computing (CIM). The working principle of these devices relies on the so-called resistive switching mechanism, e.g. the passage between two resistance states, the High resistance state (HRS) and the Low resistance state (LRS) through the application of an external voltage stimulus. These two resistance states can be ascribed to the "0" and "1" outputs of the conventional CMOS transistor-based memories. Despite demonstration of efficient processing of information and computational capabilities, details underlying physicochemical mechanisms in memristive devices still needs to be explored.

In the present work, Metal-Insulator-Metal (MIM) devices based on anodic NbO_x are proposed to study how the different materials involved in the fabrication affect the RS properties of the aforementioned devices. After a first general introduction on the memristive devices, in the second chapter the attention will be focused on the characterisation of the oxide layer properties, from the study of the structural to the chemical analysis, then, through suitable electrical measurements, connection between the material properties and the switching capabilities will be discussed. In the third chapter, the attention will be devoted on the study of different metal electrode materials and correlations between the choice of the Top Electrode (TE) metal and the switching capabilities of the realised devices will be described. The choice of the TE metal in the VCM devices plays an important role in the switching capability of the NbO_x. In particular, these results will be used as guide line to delineate a possible selec-

tion rule for the realisation of NbO_x-based memristive devices. Alongside to the switching properties, even the possibility to observe quantum conductance capabilities will be shown. Finally, conclusions and perspectives of the NbO_x devices will be discussed.

Contents

List of Figures

List of Tables

Chapter 1

Introduction

1.1 Background

Nowadays, the always increasing demand of smart devices and the fast developments in electronics are pushing the hardware capabilities towards its physical boundaries. The answer to this continuous growing demand has been satisfied with the device scaling. With the miniaturization it has been possible to increase the density of devices, improving costs and computational speed. From an historical point of views, the rules governing the trend in electronics evolution starting from the device realisation, the production costs and the device performances are known as Moore's laws [1, 2]. Up to now, we are in a critical point in the device evolution because the Moore's laws are approaching their limit. This means that, the hardware technologies will be no more compatible with the current one, making the development of new computational architectures necessary. The major challenge encountered in this framework is related to the memory bottle-neck, also known as the Von Neumann bottle-neck [3], which relates to the data transfer between two fundamental units, the memory and the processor. Usually, the amount of data coming from the memory is too large with respect to computational capability of the processor and for conventional transistors, which actually are the widest used fundamental devices in this approach, the main limitation encountered lay in heat wall, the memory wall and the Moore's law. To overcome these problems, it is necessary to develop new approaches in the data storage technologies and computation.

A help could come from memristors, which, alongside the possibility to have a high density integration on chip, allow to reduce the bottle-neck in computation with in-memory computing, and at the same time provide better memory storage and enable the possibility to perform bio-inspired computing. All these features find large employment in different fields of application, such as internet of things (IoT), big data, machine learning and realisation of artificial neural synapses. In this perspective, memristive devices can be used as random access memories (RAM) providing a faster signal transmission, because compared to traditional static or dynamic RAM they do not need hierarchical architectures in the integration and in the interconnections [4, 5]. Following the trend of the miniaturization for the high density integration on chip, memristive devices can be scaled to the nano-metric size, since the working principles at their basis allow that. For this reason, in the last years, the research in the framework of memristive devices focused on the development of strategies to increase the performances to make possible the practical use of memristors and at the same time in the study of new materials to be employed in their realisation. In this dissertation, the attention on memristive devices is focused on the materials involved in the realisation and how they impact on the device functionalities, nevertheless. In this framework, it is convenient to start with the description of basic memristive devices in form of monolithic sandwich structures, in which the material of interest for the switching is embedded between two metal electrodes.

1.2   Memristor: the 4$^{\text{th}}$ circuit element

A first testimony of the memristor goes back to 1971, in particular in the work of Leon Chua [6] in which he postulated the existence of 2-terminal circuit element with the peculiar capability of establishing a relationship between the charge q and the flux-linkage ϕ. The charge and the flux are related to the circuit variable i and v through the relationships:

$$q = \int_{-\infty}^{t} i(\tau)d\tau \tag{1.1}$$

$$\phi = \int_{-\infty}^{t} v(\tau)d\tau \tag{1.2}$$

In the circuit theory it is well-known that between each couple of the circuit variable q, ϕ, i and v there is a physical circuit element which physically realize the constitutive relationship. In particular, these elements are the *resistor*, the *capacitor* and the *inductor*.
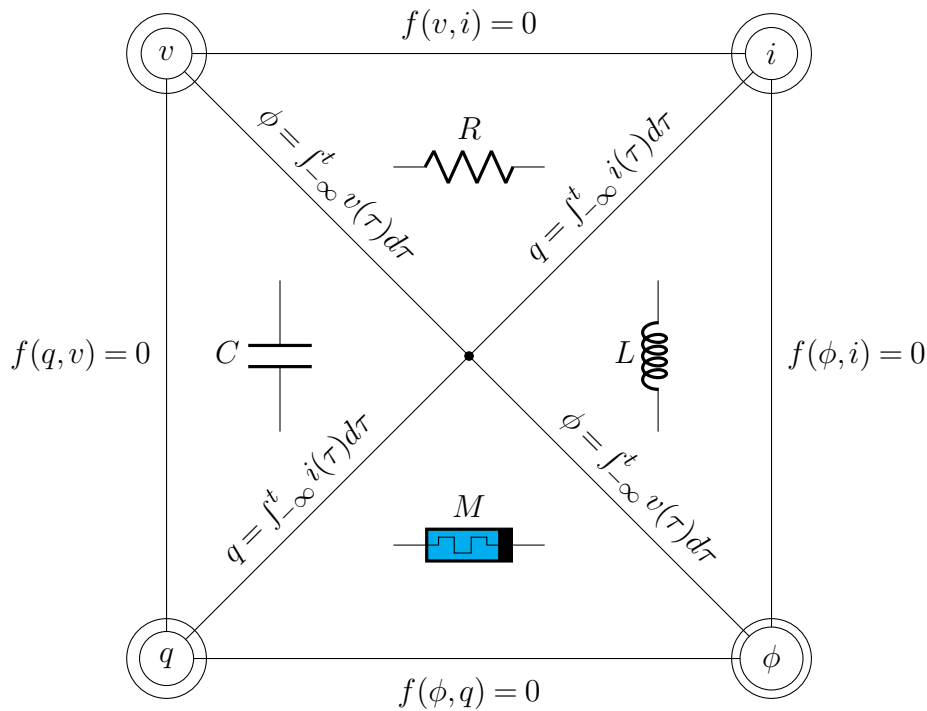
Fig. 1.1 The four quadrant elements scheme. Each couple of circuit variable is described by a constitutive relationship. Each quadrant shows the corresponding circuital element reproducing the constitutive relationship between the variables in the corners. The circuit element which establishes significance between charge and flux-linkage is the *memristor*, highlighted in cyan.

The scheme in Fig. 1.1 is the so-called 4-quadrants element scheme, and is a representation of the 4 fundamental circuit variables v, i, ϕ and q. In these representation the circuit variables are represented at the 4 corners of a square and all the possible relationships among there are represented. Of the 6 possible combination of these circuit variables, five were well-known, in particular, the two relationship describing the evolution on the charge and the flux-linkage in the expressions **1.1** and **1.2**, but also the relationships describing the circuit elements named *resistor*, *capacitor* and *inductor*, given by the following differential/close-form expressions:

$$R = \frac{dv}{di} \iff f(v,i) = 0 \qquad (1.3)$$

$$C = \frac{dq}{dv} \iff f(q,v) = 0 \qquad (1.4)$$

$$L = \frac{d\phi}{di} \iff f(\phi,i) = 0 \qquad (1.5)$$

At the beginning, before the Chua's theorization, a description of the link between the variables q and ϕ was missing and as a consequence of this, there was also a loose in the symmetry of the scheme, because there was no a circuit element able to establish significance between them. The idea of Chua was to intuitive but at the same time genial, he though in a fourth circuit element, what he named the *memristance M*, the missing link between the charge q and the flux-linkage ϕ, whose relationship close the symmetry of the scheme:

$$M = \frac{d\phi}{dq} \iff f(\phi,q) = 0 \qquad (1.6)$$

Until that moment a real physical circuit element which realised the memristance was still not known, even because the memristance should in principle exhibit properties really different and peculiar with respect to the one attributed to resistors, capacitors or inductors, which also means that no combination of this three passive elements or, alternatively speaking, no RLC two-terminal network, is able to realise the relationship in **1.6**. For the seek of completeness and for measurement reasons, the relationship in **1.6** can be rewritten in terms of the circuit variables v and i exploiting the expressions **1.1** and **1.2**:

$$v(t) = M(q,t)i(t) \qquad (1.7)$$

In which the memristance M is shown to be a function of the charge $q(t)$. This is important, in fact if someone looks at the expression in **1.1**, immediately will understand that the value of the memristance, even if is punctual because can be expressed through a differential relationship, is still dependent of the definition of the charge and so from the integral between $-\infty$

and the time t, and this means that the value of the memristance depends on the *history* of the system. Another important conclusion can be deduced from the expression **1.7** that figures out the memristance is dimensionally a resistance. So putting together the last two concepts, we have in principle an idea of what a memristance is, or a memristor represents from a circuit point of view: a resistance that keeps track of the past history of the system, but is still defined by the instantaneous value of the current and the voltage $i(t)$ and $v(t)$. At this point, the idea of a 4$^\text{th}$ element closing the circuit square is delineated, but, looking the expression **1.7** the memristor is represented as a black box whose transferring function is only a function of the input and output itself, and of the history of the circuit, but none information about what is inside is given. To understand this, someone can consider the concept of resistance expressed by **1.3**, it is known that for a linear cylindrical metal conductor, the expression of R is given by:

$$R = \rho \frac{l}{S} \tag{1.8}$$

In which it is highlighted the effect of the material and its geometry. This expression can be further complicated by introducing other effect related for example to the temperature:

$$R(T) = R_0(1 + \alpha \Delta T) \tag{1.9}$$

in the expressions eqs. (1.8) and (1.9) all the element appearing on the right side represent the so-called state variables. A state variable is representative of the element under test and can alters in a specific way its behaviour. These variables can be represented by the temperatures, the involved materials and geometry, the chemistry, the structure, the magnetization, etc... In the expression **1.8** the state variables are the geometrical factor of the conductor, while i n the **1.9**, that describes a thermristor, in addition there is the temperature. To take into account this concept, in the 1976 Chua introduced it in the description of memristor [7]:

$$v(t) = M(\bar{x}, q, t)i(t) \tag{1.10}$$

Where $\bar{x}$ is the vector containing the internal state variables.

Alongside this concept, it was introduced the one of kinetics expressed by [8]:

$$\dot{x} = \frac{d\bar{x}}{dt} = g(\bar{x}, i, t) \tag{1.11}$$

The **1.11** describe the temporal evolution of a system and in the specific case of a memristive system it can provide information about the dynamics.In particular, the effect of the history of the circuit is this time defined in the vector $\bar{x}$:

$$\bar{x} = \int_{-\infty}^{t} g(\bar{x}, i, \tau) d\tau \tag{1.12}$$
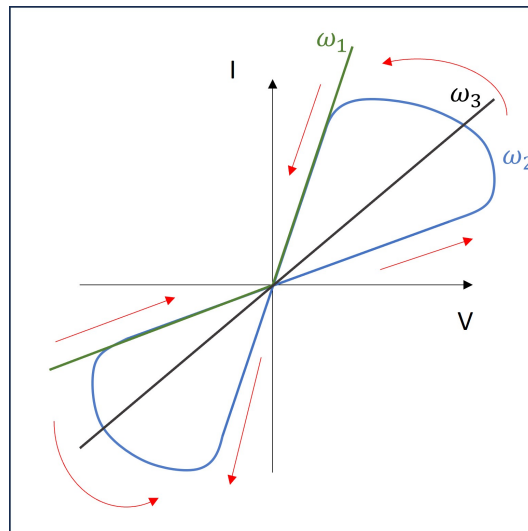
Fig. 1.2 *I-V* characteristics of a memristor. The behaviour of the current depends on de frequency of the external V signal.

At this point, it is clear that the previous thermristor described by the **1.9** can not be considered as a memristor because it lacks of the part taking into account the history of the circuit. Fig. 1.2 shows how the typical *I-V* characteristics of a memristor following the description of Chua looks like. In this sense, there is a non-linear behaviour in the resistance that, considering all the features introduced until now, is strictly dependent on the frequency of the external voltage input. As described in this qualitative plot, at low frequencies ω_1 ($\omega \to 0$), or in other words, in DC, the behaviour of the memristor act as a

non-linear resistor characterised by two different resistance values, dependently on the voltage polarity. At high frequencies ω_3 ($\omega \to \infty$), the memristor acts like a linear resistor. At intermediate frequencies ω_2, the behaviour is the one described by the blue pinched hysteretic loop.

In conclusion, a memristor is very similar to a non-linear resistance circuit element, but differently from the conventional resistors that can be characterised through the Ohm's law, this new circuit element take trace of the past history through the **1.11**.

1.3 Memristor and memristive devices

In the previous paragraph the concept of memristor was delineated, in particular, at the end what it resulted is the memristor can be assimilated to a circuit element able to vary in a non-linear way its resistance. Beside the axiomatic definition of memristor and the idea of memristance had in previous paragraph, the concept of a real working memristive device, comes later in the 2008 with the realisation of the first memristive device from Stanley Williams [9] at the Hewlett-Packard (HP) laboratories. The group of Stanley Williams included the concept of state variables and kinetics to the working principle of the RRAM, in this sense the first monolithic memristive device was realised by sandwiching a thin titanium oxide layer between two Pt electrodes.

Although, it is of great importance to say that the concept of resistive switching was already known in the scientific community, even before the discover of Stanley Williams. Many research groups, from different application fields, already studied this phenomenon adapting for example to the realisation of diodes[10], and others to study the switching mechanisms in different materials such as Rainer Waser [11]. However, despite the huge quantity of studies on the resistive switching in the literature and the discover of Stanley Williams, there is still no a real design concept for the realisation of a memristive device. Despite this, when talking about resistive switching and resistive switching devices the majority describes systems realised by sandwiching an insulator material between two metal electrodes. In fact, it is not uncommon referring to resistive switching memories as metal-insulator-metal (MIM) or metal-oxide-metal (MOM) structures [12–14]. It is clear that a huge combination of

RRAMs - Resistive Random Access Memories

MRAM	FeRAM	eRAM	ReRAM	PCM	ECRAM	NRAMs
• STT-RAM • Spintronic-RAM	• FeRAM • FTJ • FeFET	• Nanometal-lic RAM	• ECM • VCM • TCM	• PCM (compound or element)	• ECRAM	• Carbon NT (vdW)
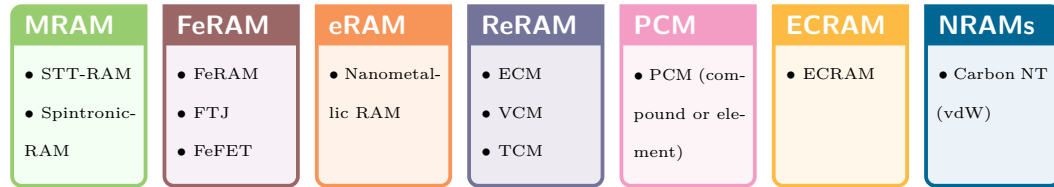
Fig. 1.3 Classification of different RRAM types according with their working principle.

insulating materials and metal electrode can be exploited in the realisation of resistance-based memory devices, all exhibiting resistive switching capability, but having at the basis of their working mechanism different physical principles. Given this premise, it is possible to classify the resistive switching devices with memory function, or in other words the RRAM, in different groups, upon their operational principle.

The different class of resistance-based memory devices reported in Fig. 1.3 highlights how complex and variegated could be the description of the resistive switching. In particular, dependently on this classification, different physical mechanisms are involved in the working principle of these devices, the main are:

- Magnetic

- Electrostatic

- Atomic Configuration

In the first group we find resistance-based devices characterised by magneto-resistive effects, such as MRAM. These class of RAMs exploit magnetic effect related to the spin transfer or to the internal magnetization in the insulating layer [15–17]. In the second group we can find resistive switching memory devices whose main mechanism is caused by the current leakage through flash gates or polarization effect in the insulating material, such as, typical real devices here are FeRAM. The last group is the most variegated and interesting from a phenomenological point of view including ReRAM, PCM, NRAM and others. Here we have both the devices in which the switching is caused by the

ion migration, in particular, very famous are the Electrochemical Metallization Cell (ECM) and the Valence Change Memory Cell (VCM), but also the Phase Change Memory (PCM) and the Thermochemical Memory Cell (TCM) [18–24].

1.3.1 Redox-Random Access Memories - ReRAMs

Among the possible classes of RRAMs, in this dissertation the attention will be focused on Redox-RAM. This particular ensemble of real devices includes all those MIM systems in which the memory effect is given by the passage between two resistance states and this is enabled by redox reaction involving the insulating layer and/or the electrodes. These redox reactions are generally activated through the application of an external voltage bias and produce ionized species that can be driven through the oxide layer. The resistance change is generally realised into two steps, the first is the Dissolution and the second is the Electromigration [25]. Dependently on the involved materials, different classes of Re-RAM can be distinguished, characterized by the type of the ionic species involved in the electromigration process. Here the two most popular classes of ECM and VCM cells will be analysed.

1.3.2 Electrochemical Metallization (ECM) effect

The device operating with this principle are the first for which there is a direct observation and clarification of the phenomenon. According to Valov et al. [22], who gave a comprehensive explanation of phenomenology at the basis of these devices, the working principle which can explain the resistance variation (e.g. the switching) in this type of cells, should be the formation of a conductive filament inside of the insulating layer of the typical MIM structure. For this reason, the memory working with this effect are usually named CBRAM or conductive bridge RAM.
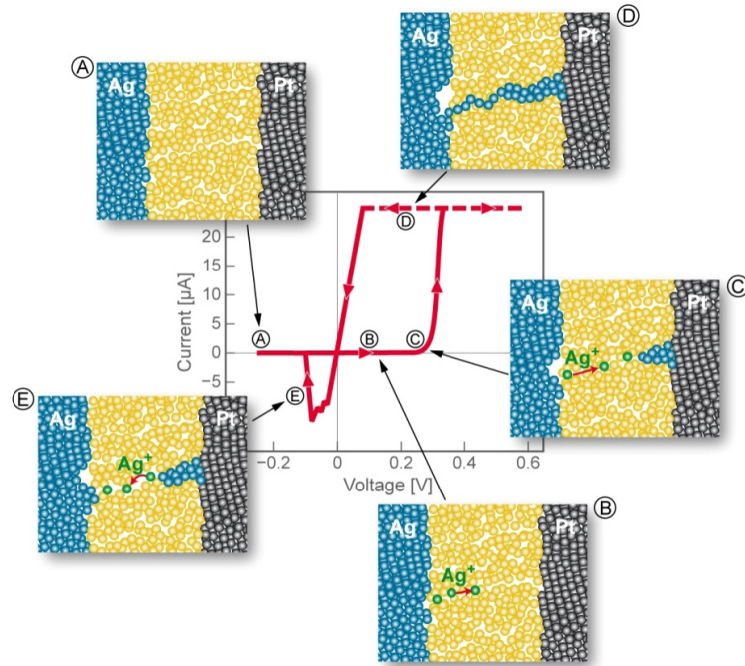
Fig. 1.4 Schematization of the working principle of a typical ECM cell device. Reprinted from [22]

As depicted in Fig. 1.4 we have a two terminal device which is composed by a solid electrolyte (yellow layer, e.g. the insulating layer) sandwiched by two metal electrode, in this example a Ag electrode, at which we will refer as the active electrode (AE) and a Pt electrode, exploited as counter electrode (CE). In this example, the choice of the Ag electrode is crucial, because the redox mechanism at the basis of the ECM cells should be investigated in the electrochemical activity of the AE and on its capability to dissolve in the solid electrolyte layer once a sufficiently high external voltage stimulus is applied between the two electrodes. At the beginning Ⓐ, the cell is in its pristine or virgin state (e.g. as fabricated) characterised by the insulating properties of the solid electrolyte that explain why the current is so small and the resistance is very high. Let us suppose a triangular voltage ramp is applied between the AE and the CE, with the voltage directly applied on the AE. As soon the voltage increases in the positive direction Ⓑ, the Ag atom which are at the interface of the solid electrolyte layer start to oxidise following the general equation path:

$$M \rightarrow M^{n+} + ne^- \tag{1.13}$$

In the chemical reaction **1.13** "M" represents a general metal able to oxidize, which in this case is Ag. As soon the Ag^+ ions are produced as reaction product of the **1.13**, they starts to be driven by the electric field as mobile charge and following the potential difference between the two metal electrodes, start to accumulate at the CE interface Ⓒ. The process of ion generation is often called *dissolution*, because the AE looks like it is dissolving in the solid electrolyte instead the ion movement through the insulating layer by the electric field is called *electromigration*. The increased positive voltage not only increases the dissolution of the AE, producing more Ag^+ species, but at the same time favour their accumulation at the CE and as soon the process goes on, a metal filament composed by Ag starts to grow from the CE to the AE. At a certain voltage, the growth of the filament is completed (between Ⓒ and Ⓓ). This process is called *Electroforming* and the resistive switching mechanism, for these type of memory devices, can be explained starting from this point. Once the Electroforming process is completed, the conduction, which in the beginning was only associated to the ionic conduction, assuming the solid electrolyte as a perfect insulating material, now can take place inside of the metal filament bridging the active and the CE, and is a pure electronic conduction, characterized by the conductance of the filament which is further higher rather than the solid electrolyte one. We have the so-called passage from what is ascribed to be the High Resistance State (HRS) to the Low Resistance State (LRS). And that is how the first part of the switching takes place. Now we should consider what happens when reversing the voltage polarity. Once the external applied voltage reaches its maximum positive value, the voltage ramp is reversed. Now the conduction is purely electronic through the metal filament Ⓓ and it is characterised by a linear behaviour, typical of the conduction through an ohmic conductor (note that in Fig. 1.4 the current saturates to a fixed compliance current, CC, value set to prevent damages to the device). Following the imposed external voltage ramp, the device experience the negative voltage ramp too, and the voltage starts to increase in the negative direction. Here the conduction is still ohmic through the filament, until something happens: the reversed voltage polarity induces the opposite chemical reaction, that starting from the Ag in its metallic state oxidises again to Ag^+. The new Ag^+ ions produced, driven by the electric field, move move in the opposite direction. As soon the process continues, the filament breaks and the electronic conduction

stops. The current is now subjected to a slight fall down which the device again in its HRS Ⓔ. This step explains how it is possible to recover the HRS explaining also how the reverse switching phenomenon happens. The process just described can be repeated several times, in order to have in a cyclic way, the alternation between the LRS and the HRS (and vice versa).

To summarize, the resistive switching mechanism in the case of ECM cell devices is related to the formation and the rupture of the metal filament composed by the same material of the AE. What it is crucial for this class of RAM is to have an AE which is characterised by high solubility and ion mobility at the operative condition. Common choices for the AE are generally AG, Cu, or their alloys, because the oxidation process of these metal electrodes can be triggered at relatively low voltages as shown from cyclic voltammetry measurements [26], make them perfect candidates in the realisation of ECM cells.

1.3.3 Valence Change Memory (VCM) effect

Differently from the memories working with the ECM effect, the ones operating with the VCM are characterised by redox reactions which involve only the chemical species of the insulating layer. Generally, the mobile species involved in this case are the anionic one because the cationic species inside the insulating layer are characterised by a lower ion mobility and consequently they can be considered immobile or not-participating to the ionic conduction during the switching process.
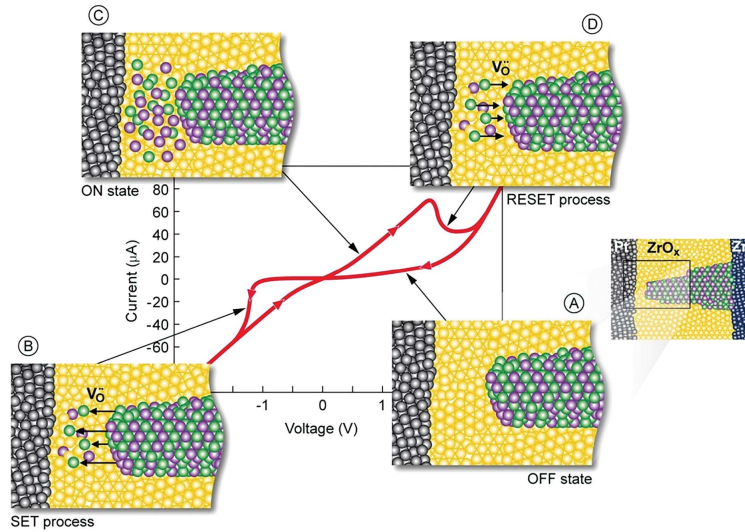
Fig. 1.5 Schematisation of the switching mechanism in a VCM cell device. Reprinted from [27].

The mechanism at the base of the resistive switching in the VCM cells is well described by Prof. Waser Rainer [27]. Here we find again, for analogy with the ECM cells, an active electrode interface, which in this case is characterised by an inert and/or immobile metal/compound, at which the switching process is expected to happen, an insulating layer which is characterised by an electrical point of view by a mixed ionic and electronic conduction (MIEC) and a counter electrode which establish an ohmic contact with the insulating inter layer. For VCM cells,a sketch of the switching mechanism can be found in Fig. 1.5 and refers to the formation of a conducting channel inside of the insulating layer. Referring to the conductive filament mechanism shown in Fig. 1.4, here a pre-formed $Pt/ZrO_x/Zr$ device experience a complete voltage sweep starting from the negative polarity to the positive one, and comeback. This is not a mandatory task for VCM cell, but in principle having a metal electrode as CE and its oxide as insulating layer, can be a good way to ensure an ohmic contact, that is why in this example we Zr and ZrO_x. We start from the HRS, characterised by very low current in the *I-V* curve Ⓐ. In this case, by applying a negative voltage on the active electrode (Pt), we are able to produce mobile oxygen species (e.g. oxygen vacancies) able to move in the insulating layer attracted by the negative potential of the electrode. In the meanwhile, the ZrO_x reduces to a lower valence state with respect to the initial one. These chemical species, differently from the oxygen vacancies are less mobile and

can be considered nearly immobile. So that, as soon the negative voltage increases, the oxygen vacancies accumulate at the active electrode interface. In a similar way as we discussed in the previous section, the application of a negative voltage is now able to trigger the movement of the lonely oxygen vacancies and varies the oxidation state of the Zr atoms to complete the channel toward the Pt electrode. Once the channel is completed the device switches to its LRS characterised by the low resistance of the channel and by the electronic conduction through the lower oxidation states atoms. Conversely, the application of an opposite polarity voltage is able to break the channel in correspondence of the Pt electrode by inducing the complete opposite process, which leads to the switching to the HRS of the device.

Once described the VCM effect, someone can now describe in a more complete way the switching behaviour the ECM-based devices. Usually, in the ECM-based MIM cells, the insulating layer is represented by a metal oxide, and through the external voltage not only the metallic species produced by the dissolution of the AE are involved in the electromigration, but the 'phenomenon is more complex. The oxygen species present in the oxide layer, following the mechanism describe for the VCM effect, can be driven by the electric field, in this sense, they help the formation of the conductive bridge by realizing a percolation path in which the metallic cationic species interested by the electromigration are preferentially channelled [25].

1.3.4 Bipolar and Unipolar switching

Although, not all Re-RAMs operate in the regimes described before. It is necessary to distinguish two type of operating mechanism:

- bipolar

- unipolar

The bipolar behaviour has been implicitly showed in the in the description of the ECM and VCM effect. The me memories operating in bipolar way are characterised by SET and RESET processes occurring in two opposite polarities. This means that it is possible to define a specific voltage polarity in which the SET process will triggered once a sufficiently high voltage is reached and the

same is valid for the RESET one, but triggered through the application of an opposite polarity voltage [28].

In counter-position, the unipolar behaviour is typical of all those memories in which the SET and the RESET processes happen in the same polarity and the type of the process, SET or RESET, depends on the amplitude of the applied voltage [29]. It can be said that, in order to give rise to a bipolar behaviour, it is necessary to have a certain degree of asymmetry in the design of the cell, which in other words means to have different metal species sandwiching the insulating layer, but this is not sufficient. Sometimes there are memories characterised by intermediate behaviour between bipolar and unipolar, which means that they can operate in bipolar regime, but, if the voltage sweep is too wide it is possible to give rise unipolar behaviour, and this is an unwanted features [30, 31].

To complete the description of the main effect involving the resistive switching in the Re-RAM, it should be said that for the real devices the electromigration is not caused by the application of triangular voltage bias as described in these sections, usually pulsed bias are exploited, in these sense, proper voltage pulses are used to program real memories. A typical train pulse is characterized by a V_{WR}, or a write pulse, that causes a fast passage between the OFF state to the ON state, a V_{rd}, typically smaller, used to read the resistance state, and a second couple of write and read pulse to perform the *erase* operation, which consist in to force the HRS of the memory by switching it from the ON state to the OFF state, with subsequent reading of the state [32].

In this dissertation, the studied resistive switching devices will be operated in bipolar way and by triggering the SET and the RESET operation through the application of triangular voltage ramps.

1.4 Resistive switching architectures
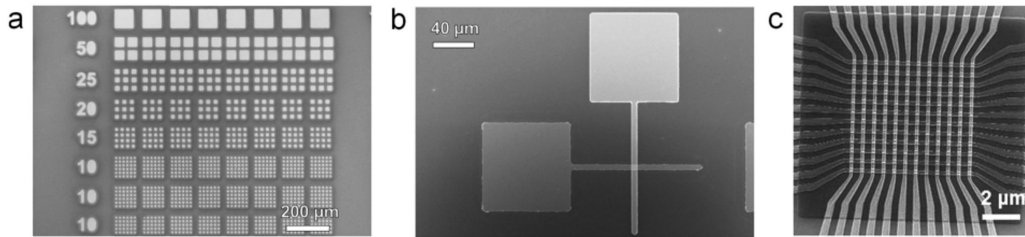
Fig. 1.6 Different resistive switching device structures. a) Common BE. b) Cross-point, c) Cross-bar arrays. Reprinted from [32]

According to Lanza et al. [32], the most common way to study the resistive switching behaviour in a material is to sandwich an insulating layer between two metal electrodes. Usually, three types of MIM structures can be realised:

- Common Bottom Electrode

- Cross-point

- Cross-bar

In the common BE structures, a thin metal layer is deposited all over the sample surface and it will act as a conductive substrate shared by all the device present on the sample. For this structure the insulating layer is deposited on the top of the common BE, paying attention to leave part of the BE accessible for the contacting part. Then the fabrication is finished by defining the TEs through a lithographic process (optical or e-beam). The TEs are all separated one to each other and can have different size depending on the mask used, usually device with small area are desired. For these type of structure the cell area can be assimilated to the TE area and the devices can be scaled as the lithographic process allow to do.

In the cross-point structure, both the BE and the TE are realised through a lithographic process. The design is the one in which two metal finger cross each other sandwiching the insulating layer. In this case, the insulating layer can be grown all over the sample surface, or, it can be possible to realise through proper designed processes, small vias connecting the two electrodes. depending

on the process used, it is possible to realise vias of small dimensions. The contact area in this case is determined by the section of the via. This structure is a valid alternative when it comes necessary to measure devices with very small contact area exploiting probe stations equipped with tips of some tens of micron. Considering the previous architectures, it is quite obvious that it is easy the contact of the BE, but for the TE there are limitations imposed by the dimensions of the tips and the size of the TE itself. the exploitation of a cross-point design architecture allow to scale the device area, but keeping the contacting area far from the one interested by the switching operations. In this way all the problems connected to the damaging of the device during the contacting part, are avoided.

The last structure, the cross-bar, also known as Cross-Bar array (CBA), is an evolution of the cross point one and is a 2D architecture. Differently from the common BE and the cross-point, in which just one device per time can be measured, in the cross-bar architecture, multiple devices can be triggered once a time exploiting multiple inputs. The CBAs are suitable for the integration in 3D architecture making them suitable for real memory application for high density non-volatile storage [33]. The different structure are reported in Fig. 1.6.

Moreover, it there exist a lot of systems whose architecture is not related to the previous ones, that act as resistive switching devices. An example are the the memristive devices based on nanostructures. In particular Nanowires and network of nanowires, in planar or vertical application attracted wide attention for neuromorphic applications [34]. These are just few examples of how it is possible to realize resistive switching devices. In this dissertation we occupy of the study of resistive switching devices based on the first proposed architecture, the common BE.

1.4.1 Common BE architecture

In the previous paragraphs we discussed about the different ways in which the MIM sandwich structure can be exploited in the realization of resistive switching devices. In this paragraph, the attention will be given on the common BE architecture, which is of great interest in the description of the devices studied in the next chapters.
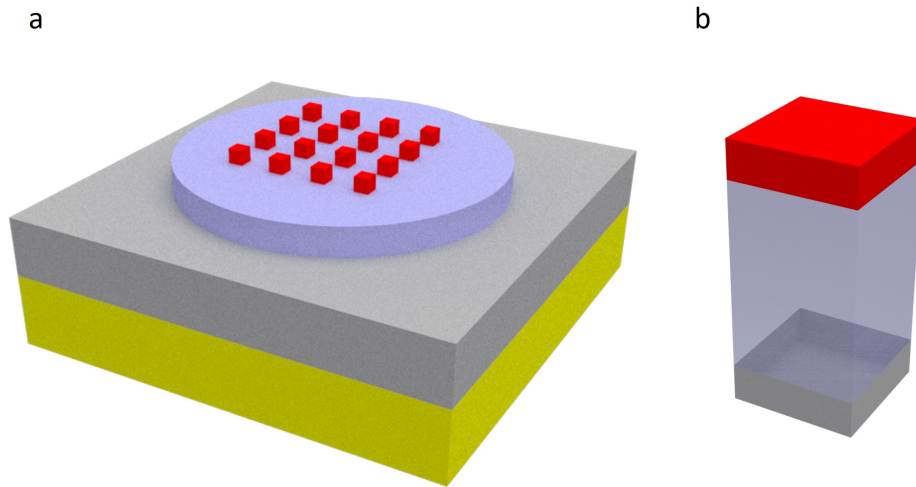
Fig. 1.7 Vertical device architecture. a) Scheme of the samples: the BE in grey is directly deposited on the top of an insulating substrate (yellow). the switching layer (purple) is grown on the top of the BE. In the end the TEs (red) are defined on the top through a proper lithographic process. b) Scheme of the isolated cell.

Usually, the design of these type of devices pass through three main steps:

- selection of the BE material

- growth of the RS medium

- definition of the TEs

Selection of the BE

The choice of the BE is crucial since the whole MIM structure will be fabricated on the top of it. Typically, the fabrication start by exploiting Si wafer covered by some hundred of nanometres of SiO_2 to prevent current leakage through the substrate during the electrical characterisation. The common BE will be directly deposited on the top of this insulating substrate. Typical choices for the BE are noble metals such as Pt or Au, but their adhesion is poor, for this reason often the deposition of these metals is preceded by the deposition of a thin-adhesion layer of Ti. For the BE metal are usually avoided materials such as Ti or Cu because they have great oxidation capability in atmosphere, this means that, after the deposition, a thin native oxide forms on their top and this can be a

problem if this oxide is unwanted in the material stack, making necessary its removal before the deposition of the RS medium. Typically, when depositing the BE, the recommended thickness is $>50\,$nm [32]. This is not mandatory, but it can help to prevent damages due to the high current densities when the devices are operating in the LRS.For the deposition of the BE metal, physical vapour-based method are the most common deposition methods exploited. Usually these methods includes a wide range of deposition techniques such as sputtering deposition, e-beam evaporation or thermal evaporation. The best technique is the e-beam evaporation since the film produced with this process are characterised by the smoothest surface with very small surface roughness.

Growth of the RS medium

The choice of the insulating layer is a fundamental task in this case: usually, transition metal oxides (TMOs) such as TiO_x, HfO_x, TaO_x, VO_x, ZrO_x, NbO_x are employed for this purpose, exploiting different technological techniques, but also solid electrolytes such as Ag_2S or Cu_2S can be employed with the same purpose. Generally, the most used techniques enable the control of the chemical composition of the deposited film such as ALD or RF sputtering (by controlling the fluxes of the gas involved in the process) other than the crystalline structure of the film, usually, sputtered film are polycrystalline if there is a crystalline target. Sometimes it can be necessary to have crystalline film and to reach the task a sequential annealing can be necessary after the deposition. The choice of ALD and RF sputtering allows to control the surface roughness keeping it lower than $1\,$nm making the grown film exploitable for RS applications. It is worth to mention that some materials show RS behaviour only when deposited with specific technique or are in a specific crystalline structure. The most notable example is the HfO_2 which does not show RS when deposited with ALD [35] or when deposited through sputtering shows stable switching only after an annealing process [36]. Recently, other techniques revealed good alternatives to the growth of the insulating layer, for example the anodic oxidation [37, 38], or other chemical methods such as the sol-gel method [39]. Other material can be exploited as resistive switching medium, for example, several studies have been conducted on polymers [40, 41]. Polymers can be easily synthesized through chemical method and directly spin-coated on the surface of the BE.

The only problem related to polymers is the high surface roughness derived if compared with the previous deposition/growth techniques. An important parameter to be considered is the thickness of the RS medium: usually tens of nanometres are sufficient to guarantee switching properties, even if, some TMOs do not show RS behaviour below specific thicknesses [42]. Finally, it is of interest, in the design of common BE device to observe that, independently on the selected method to grow the RS medium, it is necessary to keep part of the BE accessible for the measure operations. For this reason, before the grow of the RS medium it is recommended to screen a portion of the BE that will be dedicated for the contact part, with a sacrificial material, as a photoresist compound that will be removed at the end of the RS medium growth.

Definition of the TEs

The definition of the TEs is the final step to complete the device fabrication. Usually lithographic techniques are exploited for this task. In particular optical lithography with the employment of lithographic masks or direct writing methods are exploited for TEs with micro-metric size, whilst EBL technique is preferred when sub micrometer areas need to be realised. The task of the device area is strictly connect on the size of the TE and it has an impact on the device functionalities. It is widely demonstrated that devices with smaller size show more stable switching behaviour. In fact, for CBRAM, in which the switching is related to the formation and rupture of a conducting filament, the stability relies, among all the possible phenomena, even on the number of conducting channel that develop inside the RS medium. This means the stability is favoured when single channels are realized with fixed sizes. To ensure this, it is necessary that the maximum size of the TE in terms of area does not exceed $100\,\mu m^2$. This is due to the fact that the formation of the filament starts in correspondence of specific points of the TE area named hotspots and, the more the TE area, the highest the probability to find more than one hotspot. The presence of more hotspot can give rise to the formation of multiple channels or channel with different sizes that can modify the device characteristics, for example producing large variability in the SET and RESET voltages [32]. Moreover, this problem reflect when a device should be measured because to work in this regime, common probe station are no more suitable

being equipped with tips whose dimensions are comparable or bigger than the TE area, making difficult to contact the TE. For this reason, electrical measurement should be performed with the assistance of nano-manipulator in SEM or TEM systems. This problem can be solved when choosing different architectures such as the cross-point and the CBAs.

1.5 NbO$_x$ as switching material

Usually, in the realisation of memristors, especially the MIM devices, the most used materials are the transition metal oxides. In the last decades, it was shown the capability of NbO$_x$ as switching material. For this reason, it has been exploited in memristive-based devices to realize non-volatile Re-RAMs, but also for the realisation of devices mimicking the synapses behaviour artificial (synapses) and for neuromorphic computing application.[43–46]. The interest into using NbO$_x$ as switching material lead to development of a new class of non-linear circuit elements employed in the neuromorphic computing.[47] The NbO$_x$ is a very versatile material in the realisation of memristive devices, it has been largely exploited for the realisation of selector devices, exploiting what is called the "threshold switching", an important switching behaviour useful in the realisation of memory arrays.[48–59].

The NbO$_x$ is a very versatile material and can be grown exploiting a large variety of physical and chemical based processes. Most of these processes are CMOS compatible and include a series of techniques able to preserve the stoichiometry, such as the PVD through the RF sputtering, starting from a target of NbO$_x$ with specific composition, or depositing it starting from a Nb target in reactive oxygen atmosphere, often the latter is exploited in order to achieve two superimposed different stoichiometric composition, or other techniques useful to control the thickness, such as the atomic layer deposition (ALD), or to selective induce crystallization in the structure more than adjust locally the stoichiometry with the pulsed layer deposition (PLD), or exploiting other chemical method such as the sol-gel method. [60–65]

Alongside to the conventional fabrication techniques, anodic oxidation revealed useful into realize resistive switching devices, being an easy technique that does not require particular conditions such as low pressure, high purity target

material or gases. Anodic oxidation is largely exploited in the grow process of a variety of TMOs and in particular in the fabrication of TMO-bases memristive devices. Usually, the most popular materials grown using this technique are HfO_x, TaO_x, TiO_x, VO_x and NbO_x. However, the studies reporting anodic NbO_x in the realisation of memristive devices are very few.[37, 38, 66–69]

It should be mentioned that in this works there is no attention in the specific switching properties of niobium oxide and its link between the involved materials, but there is just a focus on the device performances. However, the switching properties of NbO_x are not only dependent on the oxide itself: even if the switching takes part in this layer, the resistive switching is a more complex phenomenon that involve the whole cell structure. This means that the switching properties of the NbO_x or its switching capability depend on the choice of the materials used to realize the memristive device. This means that some choice of electrode material can be useful to realize a capacitive structure that can no longer work as a memristive device and some other choices that can effectively do it. This will be better described in the chapter 3 in which the switching properties of the NbO_x will be investigated on the basis of the choice of the TE material.

1.6 Thesis outlook

This dissertation is organised in three main chapters. The first chapter 1 was thought to give a general background on the memristive devices, starting from the motivation into study them and how they were realised starting from the original idea of Chua. Different strategy were presented for the realisation of basic memristor devices and the typical material exploited as functional layer, in particular the NbO_x.

In the second chapter, a comprehensive study of the vertical anodic NbO_x devices terminated with Au is presented, with the main focus in the study of the material properties of this oxide material and trying to establish a connection between the chemical, the structural and the morphological properties of the oxide layer with the switching properties of the proposed and studied devices. In the third chapter, after discovered how The anodic niobium oxide works, the effect of different TE material such as Au, Pt, Ir, TiN and Nb were investigated

in order to find how the switching capability of the NbO_x are affected by varying the structure of the device from a material point of view and in the end comparing which material is the best candidate to realize NbO_x-based memristive devices keeping the TE area constant and reducing the oxide thickness.

The last chapter is devoted to the conclusions and the future perspectives that the anodic-NbO_x devices offers.

Chapter 2

Resistive Switching in NbO$_x$

2.1   Introduction

The fabrication of memristive devices includes a wide number of CMOS compatible techniques especially based on thin-film technology and other surface modification techniques, not conventionally adopted for the realisation of electronic devices in standardised processes.

In this chapter, we analyse in detail the realisation of vertical Au/NbO$_x$/Nb memristive devices in which the thin-film technology encounters the anodic oxidation process. The main aspect of the fabrication process will be analysed in detail, including the realisation of the anodic NbO$_x$ and the realisation of the metal contact. Great importance will be given to the characterisation on the material, which is the central core of these devices. In the end, the electrical characterisation will give explanation of the main switching mechanism of the proposed devices.

The whole fabrication and electrical characterisation of the devices presented in this chapter is carried out at INRIM laboratories (QR lab and Nanofacility

Piemonte), including the XRD structural analysis. The other characterisation
have been performed at PoliTo laboratories.

2.1.1   Device structure

The proposed $Au/NbO_x/Nb$ devices are realised as vertical structure obtained
through a bottom-up process. The devices are directly fabricated on the top
of an insulating substrate (SiO_2) covered by a thin layer of Nb exploited as
common bottom electrode. The switching layer is directly grown on the top of
the Nb film by mean of the anodic oxidation process, which occur dependently
on the geometry of the custom anodization cell, in the central region of our
sample. Finally the devices are terminated with their top electrodes realised
through Au sputtering deposition. This represents the typical MIM structure
where the solid electrolyte is represented by the oxide of the transition metal.

2.1.2   Physical Vapour Deposition (PVD)

The realisation of the switching layer starts with the anodic oxidation of a thin
Nb film which is exploited as common bottom electrode. The first step is the
realisation of this film. Different techniques can be exploited for the deposition
of Nb, but in in case we decided to adopt a typical physical vapour deposition
technique: the sputtering deposition. The sputtering deposition is part of a
series of techniques in which the mother phase of the material we want to
deposit on the substrate is a vapour or assessed to a vapour. The deposition
occurs in an evacuated chamber up to ultra high vacuum level conditions
to guarantee the purity of the material to be deposited and to prevent the
incorporation of external gaseous species in the film.

Experimental set-up
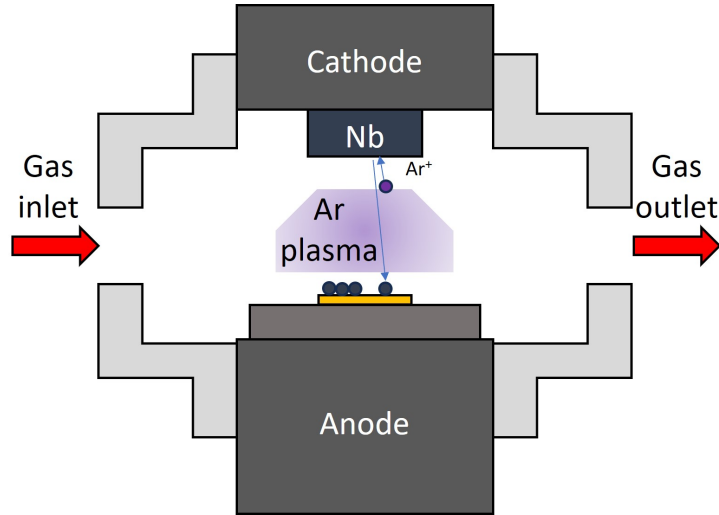
Fig. 2.1 Sputtering apparatus. The substrate (yellow) is positioned in correspondence of the anode. The cathode is represented by the material we want to deposit (Nb in this case). The Ar plasma is generated in between the two electrode triggered by high voltage and the Ar$^+$ species generated in the closest position to the cathode are attracted toward it. The impact between the Ar$^+$ species and the target is sufficiently powerful to erode it extracting clusters of metal which are deposited on the top of the substrate.

The sputtering apparatus used for the preparation of the sample is meanly composed of two chamber. The first one, the Load-Lock, is used to upload the sample and is dedicated to cleaning operation. Its main function is to keep the deposition chamber always in high vacuum condition preventing any target contamination. The deposition chamber, instead, is the core of the apparatus and here the deposition of the metal occurs.

Cleaning operation

For this operation, once the sample is loaded the Load-Lock and the chamber is evacuated from atmospheric pressure to high vacuum condition (10^{-8} mbar $\div 10^{-7}$ mbar). This operation is necessary to remove unwanted gaseous species from the atmosphere and to desorb contaminant from the surface. Once the base pressure is reached, Ar is introduced inside the chamber up to a final pressure of $5 \cdot 10^{-3}$ mbar and the Ar plasma is triggered through an RF generator. The

Ar^+ are accelerated toward the surface and through the ion impact the latter is cleaned by mean the remove of the first atomic layers: this operation is necessary to remove any contaminant from the surface, such as Carbon-based species which are luckily to be formed whenever a sample is exposed to the atmosphere and to increase the surface roughness of the sample, which turns useful to improve the film adhesion for the next deposition step. Usually, for the cleaning operations, $2\,\mathrm{min}$ of Ar plasma with $25\,\mathrm{W}$ and $700\,\mathrm{V}$ is exploited.

Metal Deposition

After the cleaning operation, the sample is transferred in the deposition chamber. Here the sample wait for the base vacuum level before the deposition, which is around $10^{-9}\,\mathrm{mbar} \div 10^{-8}\,\mathrm{mbar}$, then the Ar is introduced in the chamber until a pressure of $5 \cdot 10^{-3}$ mbar is reached. The Ar plasma this time is triggered through a DC voltage generator, assuming the target as cathode and the sample as anode. According to the scheme in Fig. 2.1, once the Ar plasma is generated, the Ar^+ species in proximity of the target are attracted toward it and the bombardment is sufficiently powerful to remove clusters of the material whose made of from it that will deposit on the top of the sample surface.

For the realisation of our samples, there is a common bottom electrode of Nb which is deposited through DC sputtering. For this purpose, $250\,\mathrm{nm}$ are deposited starting from a Nb target with 99.995% purity assisted by an Ar plasma feed with $357\,\mathrm{V}$ and $110\,\mathrm{W}$. Before the Nb deposition, to prevent the incorporation of the clusters derived from the first target layers, which may be rich in oxygen, usually, a pre-sputtering operation is performed: in this way, for a couple of minutes, the Nb is deposited on the top of a shutter which is hereafter removed and the purer Nb can be finally deposited on the sample surface.

2.1.3   Anodic Oxidation
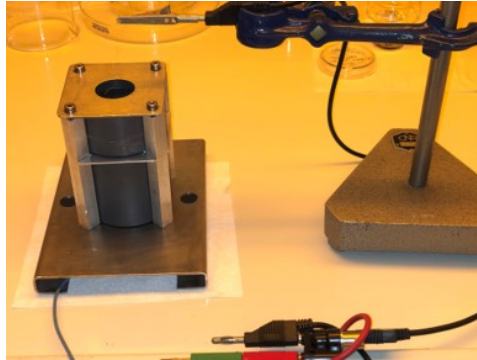
Fig. 2.2 Anodization set-up: the electrolytic cell is composed by two tubular pieces coupled together with an O-ring and clamped with a metal plate. The sample is placed inside with the surface short circuited with the bottom (anode, connected to the voltage and current generator) and the electrolytic solution is directly put on the open top part of the cell.a Pt wire connected to the current and voltage generator is immersed in the solution and close the circuit.

The insulating layer in the MIM structure is the core of the vertical memristive device. As discussed in the previous chapter, there are different materials that show resistive switching properties TiO_x, TaO_x, ZrO_x, VO_x, HfO_x, NbO_x and many fabrication techniques that can be exploited to growth them. Most of these processes require specific conditions in terms of pressure (requiring high vacuum) and of temperature (often required to grow specific crystalline phases). The anodic oxidation is an alternative process exploited for the realisation of insulating thin films starting from a metal (usually a transition metal). Despite of the previous techniques, this does not require specific laboratory conditions: it can be performed at room temperature and at atmospheric pressure, in addition, this is a fast and low cost process if compared with the standard deposition techniques.

The process
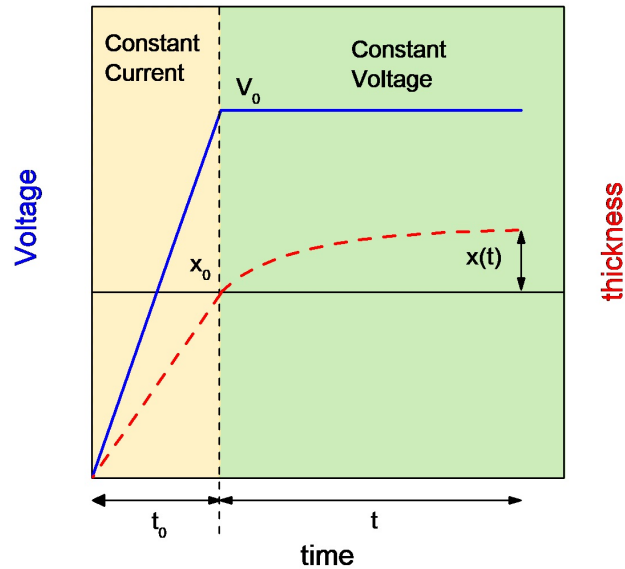
Fig. 2.3 Constant voltage anodization process.

The anodic oxidation is usually carried out at constant current density. The process takes place into two phase, as show in the graph in Fig. 2.3. In the first phase of the process, a constant current is externally applied and the voltage is monitored. After a time t_0, the voltage reaches the value of the anodizing voltage V_0 as a consequence of the growth of a thin oxide layer on the surface of the metal. At this point, the thickness of the oxide layer is x_0, approximately the final thickness of the anodic oxide. Now the second phase of the process starts: the current is adjusted through an external Labview interface connected to the electrical system in order to keep the voltage constant to the value of the anodizing voltage V_0, and the process is carried out for a time t. At the end, the final oxide thickness is $x = x_0 + x(t)$. The time t in the constant voltage phase is usually a long time, sometimes of the order of 20-30 min, and during this phase the sample can usually experience an additional oxide thickness $x(t) \approx 30\% x_0$ [71].

In the case of Nb films, the constant current step is crucial to reach the final oxide thickness, whilst, the constant voltage phase is determinant to adjust the oxide density, increasing the oxygen amount in NbO$_\text{x}$.

Anodization set-up

In Fig. 2.2 there is picture of the electrolytic cell exploited for the anodization process.
The cell is custom-made and composed of two main parts: a conducting support, on which the sample to be processed is inserted and the top part, which seals the cell, that is shaped as an upside down truncated cone, terminated with an o-ring, and that can be filled with the electrolytic solution. The cell is then connected to a current generator (Keithley 220 current source meter) which provide the current during the whole process and to a voltage generator (HP 34410a). Current is kept constant until the maximum voltage (e.g. the anodizing voltage) is reached. Once the anodizing voltage is reached, the anodization process continues at constant voltage automatically adjusting the current through a Labview$^{©}$ interface.
To ensure the electrical contact between the top of the sample and the bottom of the cell which is connected to the voltage and current generator, a Cu tape is used. Whilst, to close the electrical circuit, the top of the cell is filled with the electrolytic solution and a Pt wire is used as cathode.

Electrolytic solution preparation

The electrolytic solution exploited for the realisation of the anodic NbO$_\text{x}$ is a supersaturated solution based on ammonium pentaborate. The preparation of the solution takes place in the cleanroom. For the preparation, 13 g of $(NH_4)B_5O_8 \cdot 8H_2O$ (Sigma-Aldrich$_®$) are mixed with 76 mL of ethylene glycol (Sigma-Aldrich$_®$), then 100 mL of deionized water are added to dilute the solution. The solution is kept under continuos stirring overnight and then is filtered two times to remove the unreacted reagents.

The anodization of Nb thin film
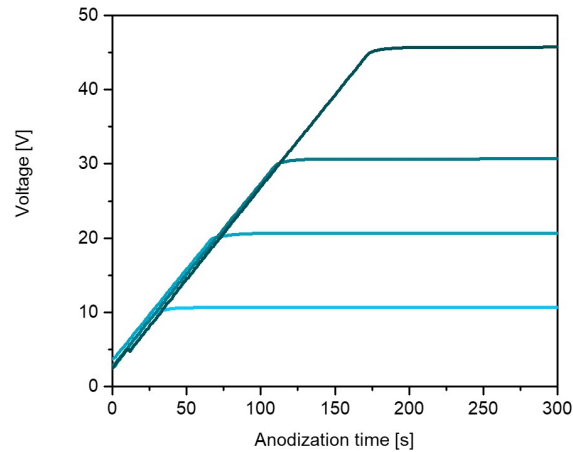
Fig. 2.4 Anodization curves. An example of the typical anodization curves acquired during the anodic oxidation of the Nb thin films. the two region at constant current and at constant voltage are clearly distinguishable.

At this point, the Nb thin films can be anodized. First of all, a contact with the back side of the sample is established through the Cu tape. The anodization cell is closed and filled with $6\,\mathrm{mL}$ of solution. The back of the cell is connected to the current generator and the circuit is closed with the Pt wire directly immersed in the solution. For each anodization, the current is set to $1\,\mathrm{mA}$, which corresponds to a current density of $1.6\,\mathrm{mA\,cm^{-2}}$, whilst the anodizing voltage is adjusted basing on the final oxide thickness we want to reach. For the whole anodization process, a total time of $300\,\mathrm{s}$ was assumed for each anodizing voltage as shown in Fig. 2.4.
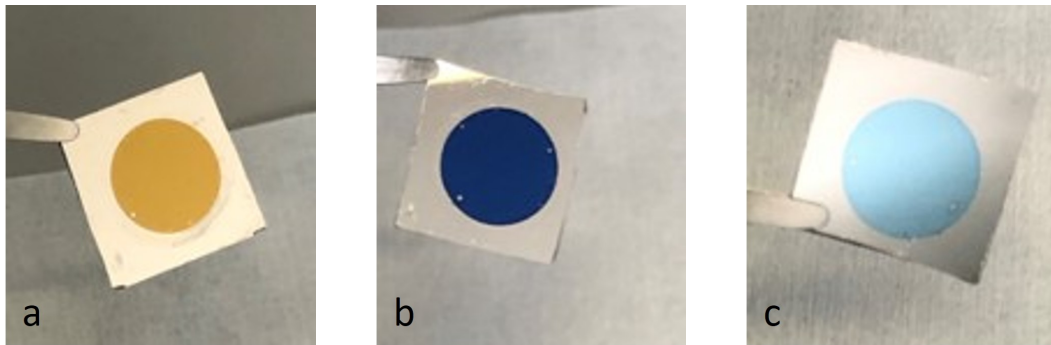
Fig. 2.5 Samples after the anodic oxidation process. The Nb thin-film on the top of the substrate was anodically oxidized at different voltages: a) 10 V, b) 20 V and c) 30 V.

In Fig. 2.5 there is an example of three Nb samples anodized at different anodizing voltages: the different colour in the central area is due to the thickness of the NbO_x layer grown.

2.1.4   Device Fabrication
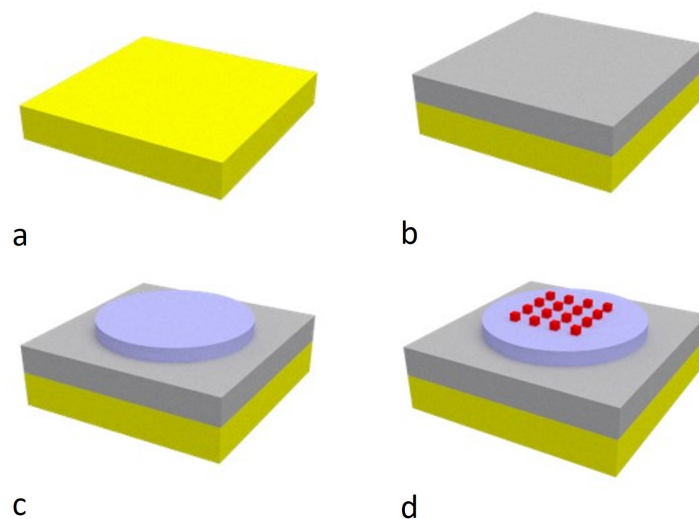
Fig. 2.6 Scheme of the fabrication process of the vertical NbO_x: a) cleaned Si/SiO_2 substrate, b) deposition of thin Nb film, c) anodic oxidation and, c) definition of the top electrodes.

The fabrication of the vertical device is resumed in the four panels of Fig. 2.6. It starts with Si/SiO$_2$ (SiMat) substrates cut in $17 \times 17 \, \text{cm}^2$. After the cut, the sample are washed sequentially first in ethanol and after in acetone for 4 min with the assistance of an ultrasonic bath (CEIA CP102, ultrasonic cleaner) at 40 °C (Fig. 2.6a). Then, a 250 nm Nb thin film is deposited through DC sputtering as described at the beginning of this section (Fig. 2.6b). The next step is the anodization process: as described in the previous subsection, depending on the geometry of the electrolytic cell, the anodization process takes place only in the central region, in a circle of radius 0.45 cm(Fig. 2.6c). Finally, the definition of the top electrodes is done using an optical lithographic process.

2.2 NbO$_x$ Characterisation

When the anodic oxidation process of Nb occurs in a water-based electrolyte such the Nb oxidizes at its maximum oxidation state compound, the Nb$_2$O$_5$. In principle, the aqueous electrolyte contains dissociated OH$^-$ and H$^+$ species, as well as other dissociated compound species derived from the salts dissolved in it. If we consider the process occurring at the anode during the anodization of the Nb films, and we consider only the oxidant species derived from water, during the second step of the anodization, the one occurring at constant voltage, the evolution of Nb follows the reaction path:

$$2\text{Nb} + 5\text{H}_2\text{O} \longrightarrow \text{Nb}_2\text{O}_5 + 10\text{e}^- + 10\text{H}^+ \tag{2.1}$$
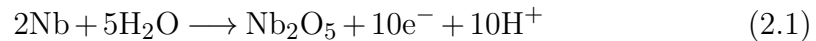
It is worth noticing that other chemical reaction could happen basing on the type of the electrolytic solution used and that, other Nb-based compound can be produced as result and incorporated in the anodic oxide film. An example of this can be using acid-based solution containing HF or H$_2$SO$_4$ because this acid compound are able, in solution, to dissolve the Nb and if added in small percentage in the electrolytic solution they give rise to the formation of porous anodic oxides. In the case of our ammonium pentaborate solution in ethylene glycol (C$_2$H$_6$O$_2$) a small incorporation of Boron can occur at the surface of the anodized film, but no reaction is expected with Nb, at the same time, some

Anodizing Voltage [V]	Thickness [nm]
10	27
20	51
30	75
45	121

Table 2.1 Anodizing Voltage vs Thickness of the NbO$_x$ thin films.

compound of Nitrogen can forms as a result of the interaction between the dissociation of ammonium an Nb leading to some nitrogenated compounds of Nb.

The material properties of the anodized samples have been investigated through different characterisation techniques in order to determine the thickness, the morphology, the structure and the chemical composition of the so-grown oxide.

2.2.1 Optical analysis

The optical analysis is performed immediately after the anodization of the Nb films and is meant to determine the thickness of the anodic oxide grown in the central region of the sample. This analysis is performed by mean of optical ellipsometry. The optical ellipsometry is a typical characterisation technique for the analysis of optically transparent thin films in the visible range, such as the NbO$_x$. The analysis is performed in reflection mode condition, which means the incident light and the collected signal from the detector are inclined by the same angle with respect to the surface of the sample. The incident light is refracted through the thin oxide layer until it reaches the interface with the Nb at which is reflected back, then it exits from the surface and reaches the detector. By analysing the polarization of the reflected signal it is possible to obtain important information regarding the optical constants of the thin layer under test and as a consequence, it is possible to determine its thickness. The optical ellipsometry was performed by means of alpha-SE Ellipsometer J.A. Woollam on several samples, acquiring the signal of the reflected light in three different spot of the surface at three different incidence angles (60°, 65° and 70°) and averaging the result.
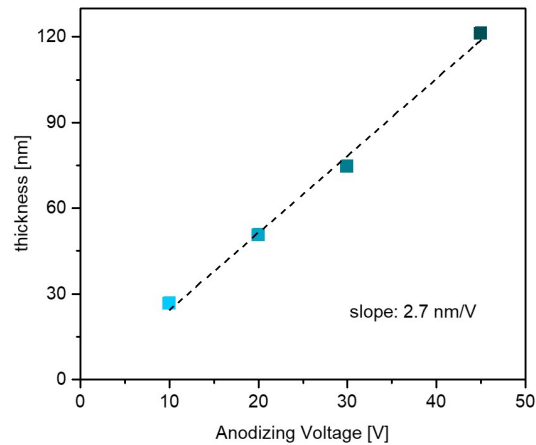
Fig. 2.7 Dependence of the anodic NbO$_x$ thin films' thicknesses from the anodizing voltage used to grow them. For the voltages under test, it seems to be a linear dependence with the thickness.

In order to determine the thickness of the NbO$_x$ thin films, the acquired spectra were fitted imposing the presence of a transparent Cauchy layer on the top of the Nb film. In this step it was no necessary to impose the exact thickness of the Nb metal film because due to its reflecting nature, after a specific thickness the ellipsometer is not able to determine it. The Cauchy layer was parametrized as usual using the variable A, B and , C all fitted at the same time. A resume of the averaged thicknesses for each anodizing voltage can be found in Table table 2.1. These results show a linear dependence of the thickness with respect of the anodizing voltage used to grow it. This is more evident in the Fig. 2.7 in which the evaluated thicknesses have been interpolated with a linear fit, achieving a growth rate of 2.7 nm V^{-1}.

2.2.2   Morphological characterisation
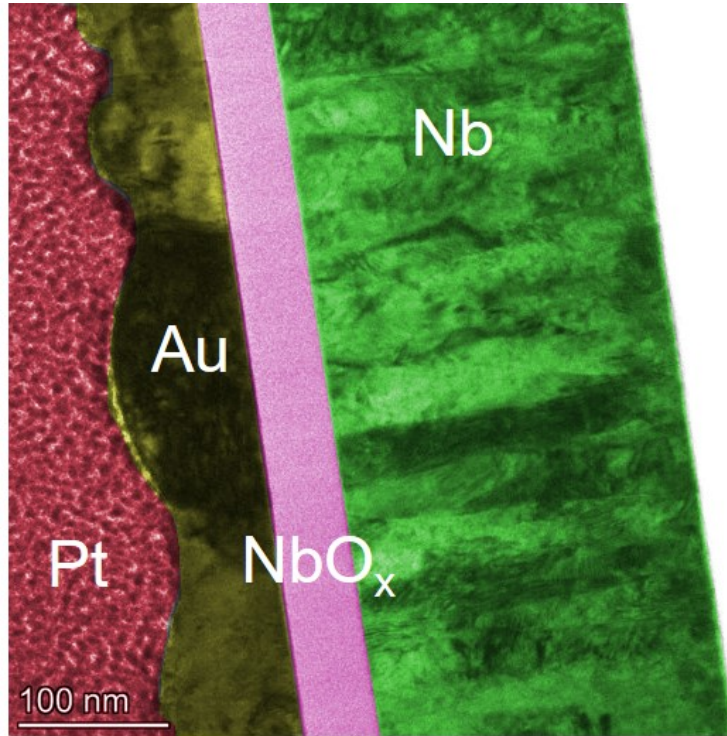
Fig. 2.8 Cross sectional analysis through TEM lamella in false colours. The stacks of the different materials is clearly distinguishable. Starting from the left side, the Pt top protective layer, the Au top electrode, the NbO$_x$ switching layer and the Nb bottom electrode.

The morphological characterization was performed on a 60 nm NbO$_x$ device terminated with Au, with the study of a TEM lamella. The lamella was extracted by mean of a standard *lift-out* technique in a Transmission Electron Microscope (TEM, TALOS F200X G2 microscope) equipped with a Focused Ion Beam (FIB) and a Gas Injector System (GIS) and observed in STEM mode in the same apparatus. Before the extraction, the region of interest was covered by a thin Pt layer to prevent the implantation of Ga$^+$ ions. The deposition was carried out exploiting $(CH_3)_3Pt(C_pCH_3)$ as a metallorganic precursor of Pt and the e$^-$-deposition method available in the TEM system. The extraction of the lamella was carried out with the assistance of a Ga$^+$ ion source operating 30 kV and a final cleaning operation was performed at 2 kV. A picture of the extracted lamella can be found in Fig. 2.8. The lamella was observed at 200 kV with a high angle anular dark (HAADF) detector. As can be observed, the

three layer of the Au/NbO$_x$/Nb structure are well-distinguishable, in particular, the most relevant information derived from this preliminary analysis are the high compactness of the anodic NbO$_x$ layer and its smooth interface with the Nb. A further information is concerning the growth method of the Nb bottom layer: in the picture it is evident the columnar growth typical of the sputtering deposition of Nb as demonstrated by the vertical stripes in the right side of Fig. 2.8.

2.2.3 Structural characterisation

The structural characterisation was performed joining together the information achieved through the observation of the TEM lamella, exploiting the STEM detector and the X-ray diffraction analysis.
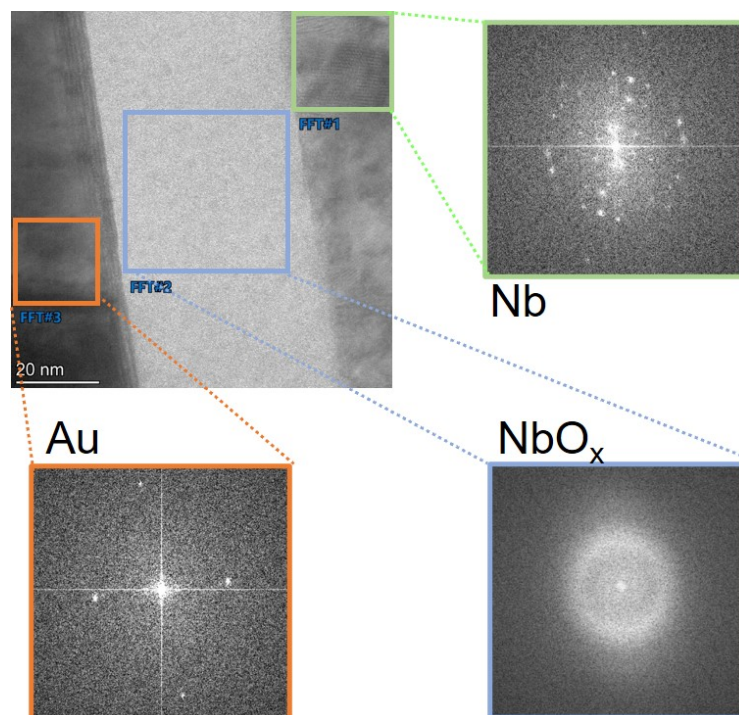
Fig. 2.9 Structural characterisation performed in TEM. From the analysis of the diffracted electron signal it is possible to have a picture of the reciprocal lattice of the observed areas in the lamella.

The first analysis was performed during the observation of the TEM lamella, in particular, the Fast Fourier Transform (FFT) of the collected electron signal

derived from the diffraction of the incident electron beam, is able to give us an image of the reciprocal lattice of the investigated areas. As shown in Fig. 2.9, the structure of the three layer is clearly evident. Au top (on the left side in the picture) and Nb bottom (on the right side) layers show the typical spots derived from a polycrystalline structure, whilst, on the contrary, the NbO_x layer is characterised by a confused circular alone typical of the amorphous materials.
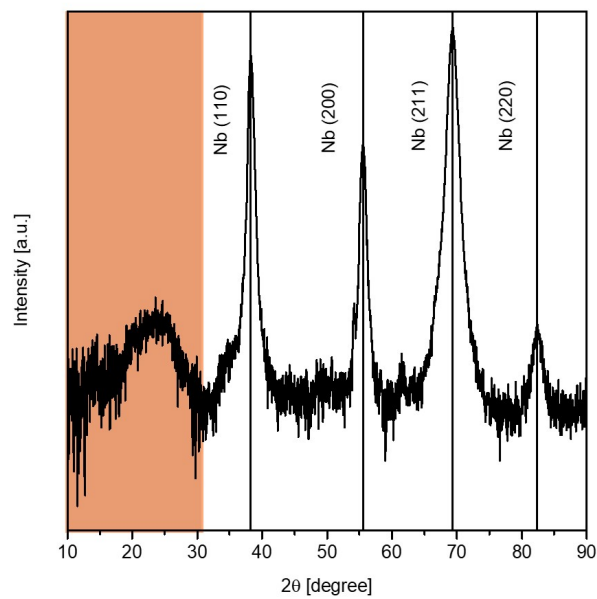
Fig. 2.10 XRD diffractogram of NbO_x layer. The diffractogram shows the typical peaks due to the Nb bottom electrodes at high angle, whilst, the highlighted red region, the presence of the amorphous NbO_x phase is clearly evident due to the pronounced bounce instead of the peaks due to the crystalline phases of this oxide.

The structural analysis was completed with the X-ray diffraction characterisation performed on the top of a 20 V anodized sample. The acquisition of the diffractiogram was carried out with the assistance of the Panalytical X-PERT-PRO diffractometer equipped with a Cu anode (K-alpha with $\lambda = 1.5419\,\text{Å}$). For this analysis, a pseudo-parallel beam configuration was adopted with a glance incidence angle of 0.8°, in order to maximize the signal coming from the anodized surface. In the diffractogram of Fig. 2.10 it is possible to observe the typical Nb peaks to to the polycrystalline nature of the sputtered Nb, but no peaks related to any kind of specific crystalline phase of NbO_x can

be distinguished. At their place, in the red highlighted region, a pronounced bounce is present: this is typical of the amorphous materials in which the presence of multiple crystalline phases is replaced by their convolution resulting in a unique hill. This should not surprise, in fact when the anodic oxidation of Nb is carried out at room temperature, and to temperature treatments such as annealing processes are sequentially performed, the resulting oxide is amorphous.[72, 73] In the XRD analysis the peaks related to the SiO$_2$ substrate have been manually removed.

2.2.4 Chemical analysis

The chemical analysis was performed on both the TEM lamella previously prepared for the morphological analysis with the the study of the transmitted electron signal, exploiting the Energy Electron Loss Spectroscopy (EELS) and on the Au/NbO$_x$/Nb device stack with the X-ray Photoelectron spectroscopy (XPS).

Electron Energy Loss Spectroscopy

The EELS analysis was performed in the same TEM apparatus described before, this time with the assistance of an energy electron loss spectroscopy detector (Continuum S/1077 spectrometer). For this purpose, a dispersion energy for the core-loss EELS of 0.15 eV was assumed to acquire both the Nb M-edge spectra and the O K-edge spectra.
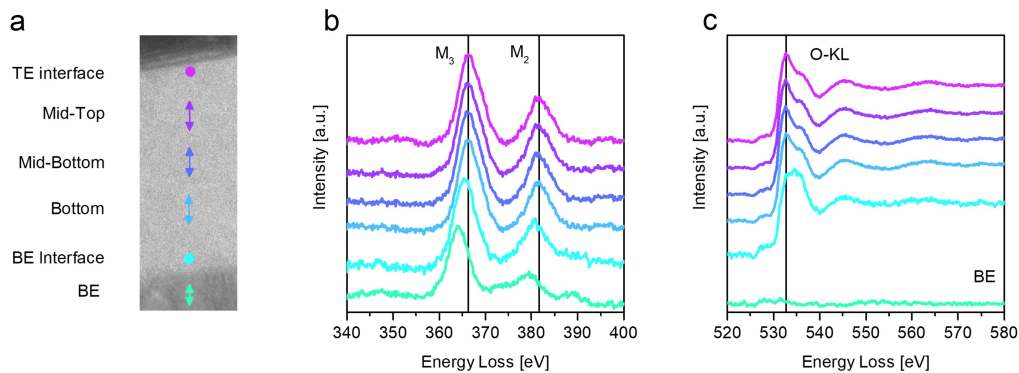
Fig. 2.11 EELS characterisation on the TEM specimen lamella. a) particular of the TEM lamella with indication on the spot in which the EELS analysis has been performed. b) M_2 and M_3 edge lines related to the Nb and c) O-KL line related to the oxygen regions.

In the EELS analysis, the incident electron beam with known kinetic energy, experiences energy loss due to inelastic scatterings event due to the interaction with the inner shell electrons of the specimen material. In this sense, the energy loss can be considered as the energy required to extract an electron from a inner shell of the investigated material and this means that this energy is specific for each material and each type of bond. In this case, the EELS analysis has been performed in different region of the specimen lamella, as shown in Fig. 2.11a. In order to identify the chemical nature of the NbO_x present in the sample, two different spectral region have been analysed, the Nb region, in which the M-edges are presents at approximately 370 eV and the K-edge at about 530 eV. The first region, in Fig. 2.11b with the M-edges, shows the peaks related to the Nb, in particular, depending on its oxidation state, this peaks undergo to a chemical shift.

In Table table 2.2 there is a resume of the EELS analysis in the region of Nb. Experimentally, the separation between the M_3 and M_2 lines is about 15.3 eV for each investigated spot of the specimen lamella . This is in agreement with the literature [74], in addition, this separation is independent on the oxidation state of Nb, meaning that both the peaks should be affected by a rigid shift toward low energy-loss once the oxidation state of Nb reduces. The main results of this analysis is that, going from the TE interface toward the BE, the NbO_x

Position	M$_3$ [eV]	M$_2$ [eV]	Composition
TE Interface	366	381.3	Nb$_2$O$_5$
Mid-Top	366	381.3	Nb$_2$O$_5$
Mid-Bottom	366	381.3	Nb$_2$O$_5$
Bottom	366	381.3	Nb$_2$O$_5$
BE Interface	365.5	380.8	NbO
BE	364	379.3	Nb

Table 2.2 EELS analysis of the M$_2$ and M$_3$ edge lines of the Nb region.

is mainly composed by Nb$_2$O$_5$, as demonstrated by the position of the M$_3$ peak at 366 eV, then, there is a very small layer at the interface with the BE, in which the M$_3$ peak is at 365.5 eV, indicating the presence of NbO. In the end, the observation in the BE, close to the interface, has been performed to show the presence of the metallic Nb, with the M$_3$ at 364 eV.

To complete the EELS analysis, the O-KL edge has been observed too. In this case we have the presence of two peaks at 532.7 eV and at 536 eV broadened together in a single pronounced peak at 532.7 eV, for all the investigated spots between the TE interface and the Bottom. This high energy loss peak now evolves toward lower loss energies at the BE interface, in which is centred at 534.6 eV, leaving the other in the same position of 532.7 eV, as described in the literature [74]. In the spot corresponding to the Nb BE, instead, no presence of oxygen is detected.

To conclude, the EELS analysis shows a massive presence of Nb$_2$O$_5$ in the whole volume of the specimen lamella, except for the BE interface in which due to the position of the edge lines in the Nb region, it seems to be only NbO.

X-ray Photoelectron Spectroscopy

A complementary, finer, chemical analysis can be performed exploiting X-ray Photoelectron Spectroscopy (XPS). Differently from EELS, in the XPS the incident electron beam is able to excite the atoms from the first atomic layers and extract electron with characteristic energy dependent on the oxidation state of the involved atomic species in the sample.

For this analysis, a-20 V anodized sample (nominal oxide thickness 60 nm) covered by 20 nm of Au for half of its surface, was used.

The sample was prepared following the standard anodization process described in the previous section, them, before the Au deposition, half of the sample was protected with a photoresist mask to shadow the surface. The region with the metal was exploited for the depth profile analysis, whilst, the uncovered, to obtain the first survey spectrum at the surface immediately after the anodization process.
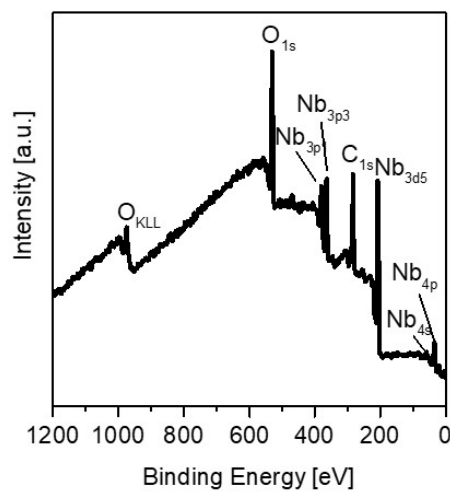
Fig. 2.12 XPS survey spectrum at the surface of the anodized sample.

The sample was uploaded in the PHI 5000 Versaprobe Scanning X-ray Photoelectron spectrometer equipped with a monochromatic Al-Kalpha X-ray source working at 1486.6 eV. Prior the analysis, the chamber was evacuated in high vacuum condition to desorb gaseous species adsorbed onto the surface. The apparatus was calibrated using the C1s peak (284.8 eV) since the adventous carbon is the most source of contamination and this causes a natural shift in the acquired spectra. A spot of 100 µm and a collection angle for the XPS signal was used. A first survey analysis was performed on the bare NbO$_x$ surface to detect all the chemical species presents in the first atomic layers. As shown in Fig. 2.12, at a first sight, the only detected chemical species on the surface are Oxygen, Niobium and Carbon. Carbon is a very common source of contamination whenever a sample is directly exposed to the atmosphere, due to

the chemisorbed CO_2. Instead, Oxygen and niobium are the only two chemical species present on the sample surface and we can focus the attention on the study of their oxidation states to establish the chemical composition of the anodized sample terminated with Au, which mimics the structure of our devices.
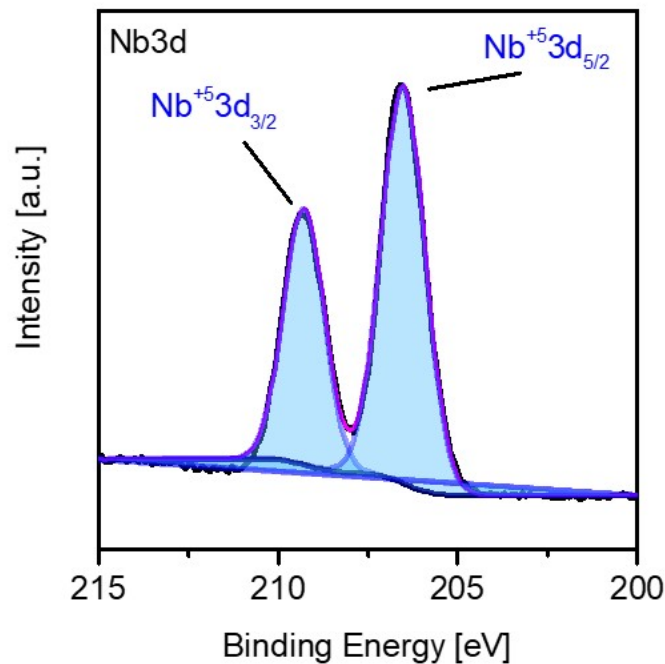
Fig. 2.13 XPS HR spectrum of NbO$_x$ at the surface in the Nb region.

Fig. 2.13 show the high resolution (HR) spectrum acquired in the region of the Nb3d peaks, which characterize the valence electrons in the Nb compound and give us information about the oxidation state of Nb.

Dependently on the oxidation state of Nb, its HR comes with a doublet with a separation of about 2.5 eV. At the surface, we have the presence of two mean peaks at the characteristics energies of 209.7 eV and 207.9 eV corresponding to the Nb3d$_{3/2}$ and Nb3d$_{5/2}$ respectively, which identify the Nb(+5) oxidation state, meaning on the surface of the bare oxide, the composition of our sample is Nb$_2$O$_5$.

For the second analysis, the depth profiling, The XPS was used in combination of a Ar$^+$ beam to sputter the surface and at the same time to collect the signal

through it during the scalp.
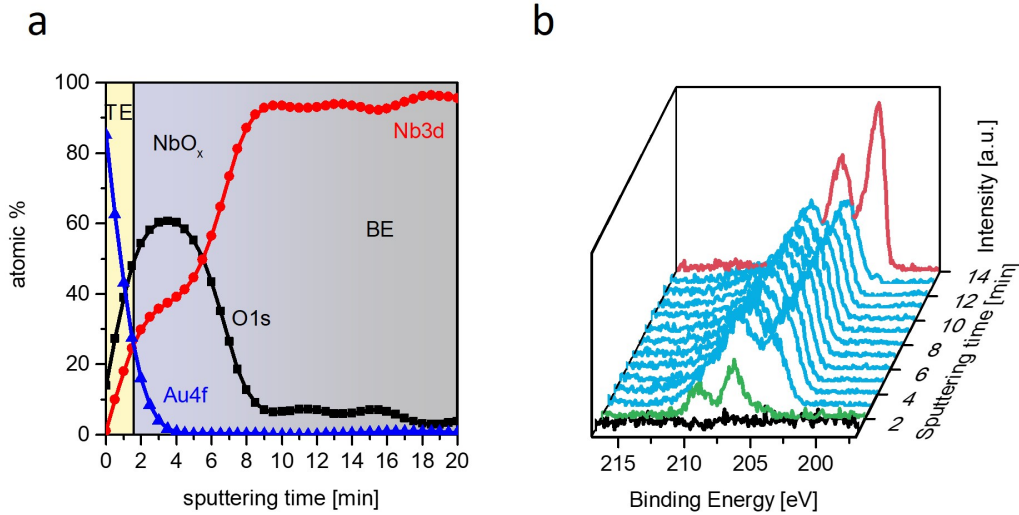
Fig. 2.14 XPS analysis. a) Atomic percentage during depth profile and b) HR spectra of Nb region vs sputtering time.

The depth profile analysis was performed of the half sample covered by Au in order to mimic the device structure. The HR spectra now are acquired at specific sputtering time, in particular each 2 min. The Ar$^+$ performs a first dig, then the XPS HR spectrum is acquired for all the element detected in the survey plus Au. Fig. 2.14a highlights the the chemical composition in atomic percentage at each sputtering time. The most important information derived from it is that the Nb signal increases going in deep into the sample, whilst the oxygen content reduces. the oxygen results in a more pronounced amount very close to the gold surface, which only appears for the first sputtering two minutes, then it progressively reduces and disappears after 14 minutes sputtering time at which the bottom Nb electrode is reached. The compositional analysis was carried out by integrating the peaks area after suitable background subtraction using Shearly baseline.

Fig. 2.14b shows how the collected HR spectra related to Nb evolve in the 3d-peaks region during the sputtering of the sample. What it is clear is that the Nb oxidation state is practically the same in the whole volume of the investigated region, except for the regions at the interfaces with the two electrodes. A more detailed analysis of this can be done giving a look on the HR spectra at

specific sputtering time which are indicative of the Au-TE interface, a central oxide region and the Nb-BE interface, at 2 min, 8 min and 14 min sputtering time respectively.
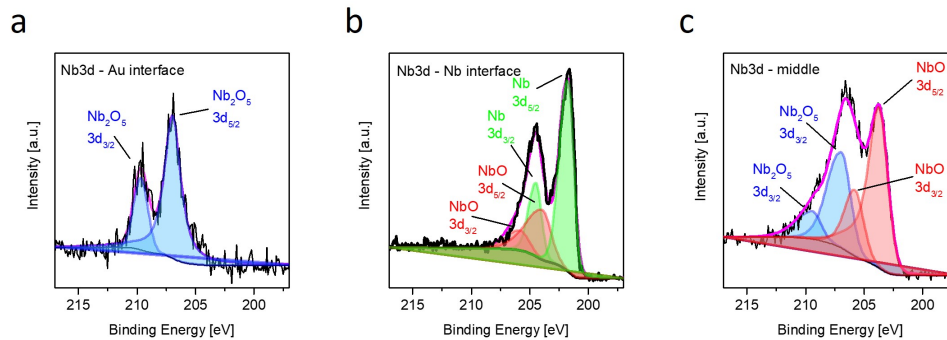
Fig. 2.15 Depth profile analysis through HR XPS spectra at different sputtering time. a) 2 min, TE interface, b) 8 min middle, and c) 14 min BE interface.

To determine the oxidation state of Nb in the whole oxide, we can analyse the spectra in Fig. 2.15. Fig. 2.15a represents the HR spectrum in the 3d region of Nb. After a first baseline subtraction through Shirley's baseline, the HR spectra was deconvolved using a combination of Gaussian and Lorentzian (G-L) distribution functions in a measure of 10% (where 0% represents a completely Gaussian distribution and 100% a Lorentzian one). To perfectly fit the spectrum under test, a 0.7 peak asymmetry was assumed and finally, a peak separation of 2.5 eV was setted in order to consider the doublet separation of the typical Nb3d peaks. The same combination of distribution function was used to fit the HR spectrum in Fig. 2.15b, at 8 min sputtering time. This time, jointly to the peaks related to Nb(+5) oxidation state, even the ones of Nb(+2) can be encountered too. Finally, in Fig. 2.15c, the HR spectrum at the Nb bottom interface deconvolved using the same function for the oxide part and with a combination of G-L function at 10% but with peak asymmetry of 0.3 was assumed for the metallic part (Nb(0)).

As a final consideration, comparing the HR spectrum at the surface (Fig. 2.13) and at the interface of the Au TE (Fig. 2.15a) it is possible to find no variation

position	$t_{sputt.}$	Nb(+5)		Nb(+2)		Nb(0)		composition
		Nb3d$_{3/2}$	Nb3d$_{5/2}$	Nb3d$_{3/2}$	Nb3d$_{5/2}$	Nb3d$_{3/2}$	Nb3d$_{5/2}$	
TE interface	2 min	209.4 eV	206.9 eV	-	-	-	-	Nb$_2$O$_5$
middle	8 min	209.4 eV	206.9 eV	205.8 eV	203.7 eV	-	-	Nb$_2$O$_5$ + NbO
BE interface	14 min	-	-	205.8 eV	203.7 eV	204.5 eV	201.8 eV	NbO + Nb

Table 2.3 Summary of the XPS analysis.

in the oxidation state of the Nb, which is definitively Nb(+5), meaning that the deposition of Au does not affect chemically the oxide and this is a confirmation that Au is unreactable with NbO$_x$. Details on the peak position for the sputtering time under test can be found in table Table table 2.3.
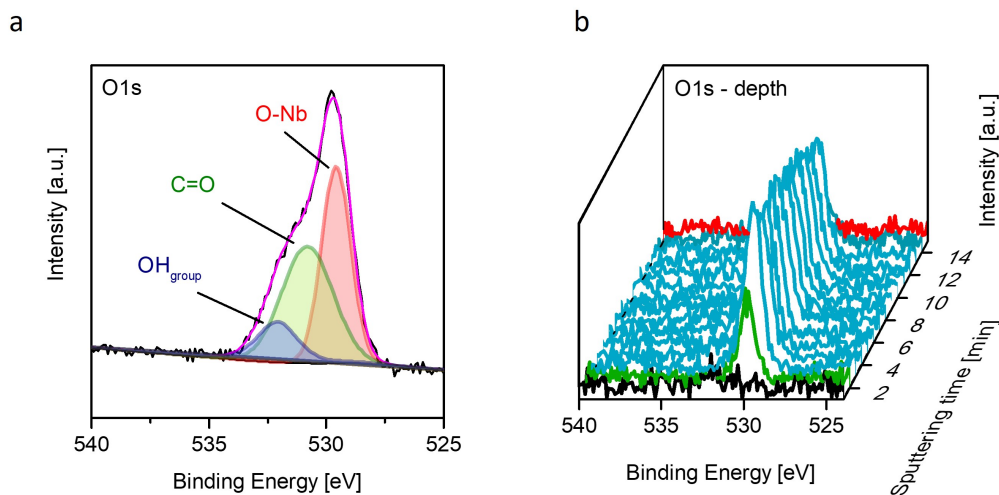
Fig. 2.16 XPS analysis of oxygen. a) HR spectrum at the surface of the bare NbO$_x$ and b) evolution of the O1s spectra during the depth profile analysis.

To conclude the XPS analysis, Fig. 2.16 shows the results for the O1s HR spectra of the oxygen in the NbO$_x$ layer. In particular, Fig. 2.16a shows the HR spectrum acquired focusing in the oxygen region (between 540 eV and 525 eV binding energies) at the surface of the anodized area. The most evident result is the presence of three main peaks: at the lowest binding energy (529.6 eV) there is the peak related to the Nb bond that now is definitively attributed to the bond of Nb$_2$O$_5$. The second peak, at intermediate binding energy (530.8 eV) is attributed to the $C = O$ bond and it is an indication of the chemisorbed CO$_2$ at the surface due to the exposition of the surface sample to the atmosphere. Last, at high binding energy (532.1 eV) there is the presence of the peak due to the OH groups.

From the chemical characterisation carried out with EELS and XPS some important conclusions can be deduced. First of all, the EELS characterisation detected the presence of the lonely Nb$_2$O$_5$ compound on the whole volume of the TEM lamella, except for the very thin layer at the interface with the

Nb BE, whilst on the contrary, the XPS analysis detected the presence of NbO and it cannot be excluded the presence of intermediate oxidation state oxides NbO_x ($2 < x < 5$). An explanation to these discordance can be searched in the characterisation process: while the TEM lamella was extracted in HV conditions through the FIB apparatus, the observation in the TEM apparatus required the exposition of the TEM lamella to the atmosphere, so that, the high presence of oxygen in the atmosphere favoured the oxidation of the thin lamella in its volume increasing the oxidation state of Nb to $+5$. Instead, at the interface with Nb, the Nb_2O_5 cannot be present because of the spontaneous reaction paths:

$$Nb + 2Nb_2O_5 \rightarrow 5NbO_2 \tag{2.2}$$

$$NbO_2 + Nb \rightarrow 2NbO \tag{2.3}$$
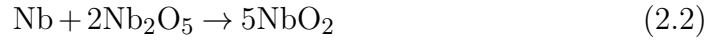
The expressions **2.2** and **2.3** describe the chemical reaction occurring at the Nb BE interface when the Nb_2O_5 is interfaced with it. Since the Gibbs free energy is negative in the directions in which the chemical reactions are written, they result in a spontaneous evolution of the Nb_2O_5 in NbO. This aspect as been well described in the literature [62], in addition, this behaviour is common to any kind of Nb_2O_5 grown on the top of a Nb film that, independently on the deposition/growth technique, give rise to the presence of a very thin layer of NbO whose thickness is around 1-2 nm [75].

In conclusion, te morphological, structural and chemical characterisations highlight different aspect of the anodized sample and the device structure. the first important information is related to the compactness of the NbO_x layer and its very smooth interface with Nb. Secondly, the anodized thin film are definitively amorphous. Last, the anodized films result in a mixture of the Nb_2O_5 and the NbO species in the whole volume, exception done at the TE interface in which the film is definitively Nb_2O_5 and at the BE interface in which it is NbO.

2.3   Electrical Characterisation

The electrical characterisations are necessary to program the devices and describe their functionalities. For these devices, being a preliminary characterization focused more into the discovery on the functionalities more than the performances, DC measurements only will be considered. For each type of experiment presented, the adopted electrical scheme is always the same: the Nb BE grounded and voltage/current directly applied on the Au TE. All the measurements have been acquired using Keithely 4200A scs parameter analyzer and subsequently processed in Matlab for the data analysis.

2.3.1   Pristine state analysis

Immediately after the fabrication process, the devices are in what is named *pristine* or *virgin state*. This represents a fingerprint or an instantaneous picture of the devices before any programming steps.
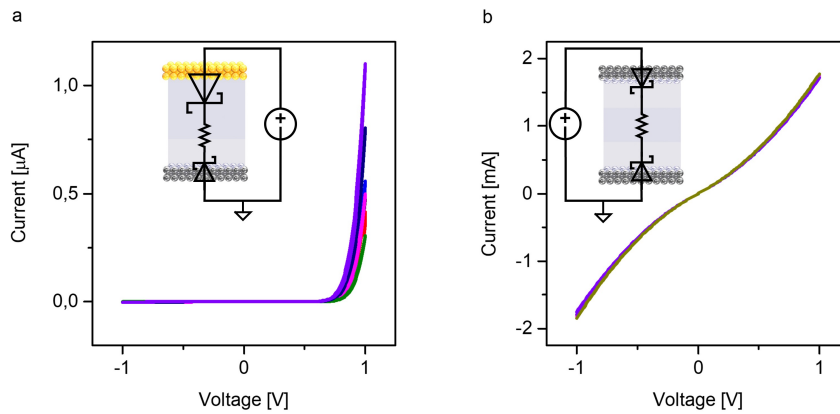
Fig. 2.17 Pristine state curves of a) Au/NbO$_x$/Nb and b) Nb/NbO$_x$/Nb devices.

An example of pristine state curves related on Au/NbO$_x$/Nb devices can be found in Fig. 2.17a. The signal, as usual for this kind of measurement, was acquired investigating a very small range of voltages, between $[-1\,\text{V}; 1\,\text{V}]$, in order to do not give rise any kind of switching process. In the picture, the asymmetric nature of these *I-V* curves is evident: the explanation to this should

be searched in the barriers at the interfaces with the two electrodes. As it is shown, there is the presence of two different types of barriers at the interfaces with the TE and the BE that arise in principle from the difference between the work function of the metal electrode (Top or Bottom respectively) and the electron affinity of the oxide, in this case NbO$_x$. The different blocking power derived from the different barrier energies is modelled using the two Schottky diodes in the back-to-back configuration. Since the Au/NbO$_x$ interface results in a lower current in our analysis, the Schottky diode related to this inter-facial barrier is represented with a greater dimension Schottky diode. This should not surprise in principle, because at the interface of the TE, as derived from the chemical analysis, the oxidation state of Nb is +5 and the oxide is characterised by its most insulating compound. Whilst, following the results derived from the XPS spectrum in Fig. 2.15c, the BE interface, being composed by NbO/Nb is characterised by a lower barrier difference between the Nb work function and the electron affinity of NbO, which is nearly a metallic compound. [76]

As a comparison, the effect of Nb TE has been studied in the symmetric structure device Nb/NbO$_x$/Nb. In Fig. 2.17b it is possible to find a collection of *I-V* curves showing the effect of the reduced barrier on both the interfaces, here modelled as two symmetric back-to-back diodes separated by the resistor representing the resistance of the oxide layer [76].

In the literature, many group proposed different models for the diode-like behaviour in memristive ECM systems, such as ZnO nanowires coupled with Pt and Ag electrodes [77]. At a first sight, having a symmetric barrier due to the symmetric material structure of the cell, causes an increase of the conductivity of the cell, in particular there are at least three order of magnitude difference in the current looking the Au terminated devices with respect to the Nb ones. As a final consideration, the barrier arising at the interface between a metal and an insulator is strongly dependent on the inter-facial chemistry, this is particularly important going toward nano-metric scaled-devices, in which the surface properties become predominant with respect to the bulk one[78, 79]. A more detailed analysis on the barrier height will be provided in the next chapter, where the effect of different TE materials is investigated in regard of the resistive switching properties of the cells under test. The conduction mechanism in Au-terminated cells can be described in more detailed way if we look at the electrical scheme in Fig. 2.17a: here, when a negative voltage

is applied on the top of the Au electrode, it acts like a reversely polarized diode blocking the electronic current injected through it into the oxide layer. Conversely, in the case of applied positive voltage, the junction NbO/Nb on the BE results in a reverse polarization, but the Au/Nb_2O_5 is in direct polarization and the result is a more conductive behaviour through the Au interface and this explains the high current in the positive polarity branch of the pristine state curve.

As a first conclusion, the presence of Au at the TE favours the increase of the resistance of the whole cell in the pristine state: this means the resistivity of the cell does not only depends on the oxide layer only, but great importance should be given to the choice of the TE material and particular attention should be kept in regard of the chemistry of interface and the possible presence of defects due to the poor adhesion of the metal film with respect to the oxide layer and/or to the mechanism of reconstruction actuated to adapt to the interface [80].

2.3.2 The Electroforming process in $Au/NbO_x/Nb$ devices

Usually, high insulating materials or metal oxides are used to realise the resistive switching medium in memristive devices, this means that the related pristine state is characterised by high resistance too. For the memristive devices based on this type of material, the process of *Electroforming* can be considered the first programming step that transform the MIM structure into a reversible switching device. The Electroforming in insulating oxide based memristive devices can be assimilated to a soft dielectric breakdown. "Soft" means that the electrical stimulus externally applied can in some ways partially reverse the breakdown. When the electrons are injected through the application of an external bias, the production of defects in the lattice of the resistive switching medium occurs. Defects can be produced in a random way elsewhere in the volume of the insulating layer, but they are preferentially generated close to the anode. The production of defects is the first step to realise the channel that will shortcut the two electrodes: the soft breakdown takes part along the percolation path created by the defects. [81] In transition metal oxides, alongside the electron injection, ionic processes are involved too. Among the

ionic processes there are the ionic motions, the redox reactions and the anodic oxidation. The ionic motion is caused by the presence of the external electric field that permeate the region between the two electrodes and on the ionic conductivity. The external field can easily drive ionic species, in a direction which depend on the their charge, along the insulating layer. Ionic motion is expected to take part along the percolation paths, consequence of the defects generation. Moreover, ions are not always a constant presence in the insulating layer, often they are generated by redox processes induced by the presence of the external field, when a sufficiently high energy is provided through the applied voltage. Ion generation through redox reactions usually takes place at the interface between the electrodes and the insulating layer as described in the previous section. [19, 27] The majority of the MIM memristive devices required an Electroforming process, unless the system can be considered forming-free, but there is no an unique strategy to trigger it. For memristive devices in which the insulating layer is sufficiently thick, typically the application of a sufficiently high DC voltage is required. This voltage can be applied as a constant bias in time or as a voltage ramp, but it depends on the considered structure. [82] For the VCM devices this is necessary in the first cycle of their life and this cycle strongly differ from the after ones. Other Electroforming methods are based on the application of voltage pulses, this usually is done by applying rectangular voltage signals characterised by different amplitude and length, many research groups exploit this procedure to study the dynamics of the process. [83, 84] Other groups have studied even the possibility to trigger the Electroforming process through the application of controlled current signals, but usually the more popular strategies require the applications of voltage bias. [85] On the basis of the previous considerations, the Electroforming process in the case of NbO$_x$ devices will be actuated by applying a DC voltage sweep.

Considering the possibility to apply both negative and positive voltage on the TE, it is possible to trigger the REDOX reaction leading to the formation of anionic moving species O⁻ and drive them both toward the top and the bottom electrode. Usually, a good balance between the forming voltage and the compliance current is necessary to make the good choice in terms of what polarity is better to initialize the Electroforming. In this case, if we choose the positive polarity, the low barrier at the Nb interface will require very small voltage, but the required current for the formation of the channel would be

very high. Conversely, in the negative polarity, we can exploit, despite of the high barrier and voltage required to complete the process, a very low current compliance, which in this case translate in a channel of small size. It is worth noticing that, in the case of conducting bridge cells as in this case, the choice of the current is crucial, the higher the current chosen, and the more stable the channel is, make it difficult to break it by applying the reverse polarity. This means, if we want to realise a channel that would be easy to break and re-form again, it is better acting with the lowest current compliance, that is why it was decided to give rise the Electroforming in the negative polarity.
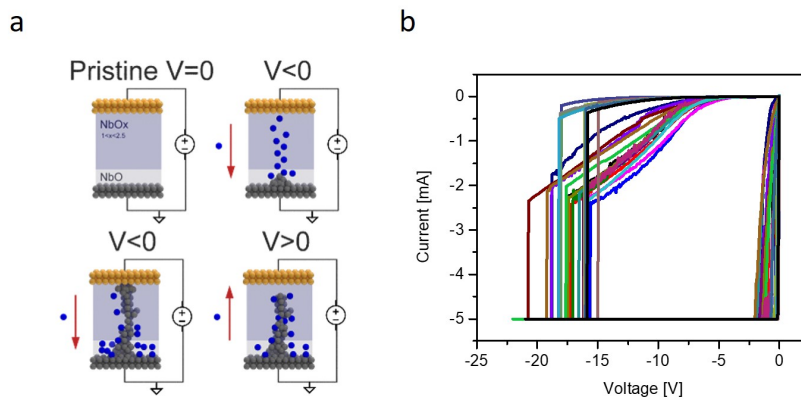
Fig. 2.18 Electroforming scheme in $Au/NbO_x/Nb$ cells. At the beginning the cell is in its high resistance pristine state. By applying a negative bias voltage on the Au top electrode, a sub-stoichiometric NbO_x channel starts to grow in the oxide layer, from the Nb bottom electrode. by increasing the negative voltage, the migration of the oxygen ions continues toward the bottom electrode, in which, the lower concentration in oxygen favours their accumulation, in the meanwhile the channel open toward the top electrode bridging it with the bottom one. By reversing the polarity, the process can be reversed breaking the channel in correspondence of the top electrode. b) Typical Electroforming curves in the $Au/NbO_x/Nb$ devices.

Fig. 2.18a is a representation of how the Electroforming process should look like in $Au/NbO_x/Nb$ devices. At the beginning, the cell is in its pristine state characterised by the high resistance of the cell favoured by the combination of the high barrier at the Au/NbO_x interface and the high resistance of the oxide layer in the top part of the device. The application of the negative voltage on the Au TE triggers the generation of both O^{2-} and Nb^{5+} in the oxide layer. The latter, considering the voltage range investigated, can be

considered immobile, whilst, the oxygen ions, the blue spheres, are highly mobility ions and easily to be driven by the electric field, even at low operative voltage. The oxygen ions are so attracted toward the more positive potential of the Nb bottom electrode and, following the different oxide stoichiometry, as investigated in the previous paragraph, they are easily to be accumulated in the layer alongside of this interface. This oxygen-deficient layer is what is called scavenger layer and its main function is to facilitate the formation of the channel acting as a reservoir of oxygen each time the switching process is triggered by applying the negative voltage polarity [38]. The grow of the channel, can be in such a way attributed only to the movement of the oxygen ion which leave their sites in the lattice along the channel structure, so that wee can imagine the channel as a depleted region in which there is absence of oxygen. This is not completely true, because the formation of oxygen ionic species implies the formation of niobium ionic species too, but they are hardly drivable through the electric field due to their lower ion mobility, or conversely, their high transport number (0.24-0.27), so that once they are formed, they can be considered immobile and only able to recombine by reduction in the channel [37, 86–88]. The metallic-like sub-stoichiometric Nb channel continues is growth until it bridges the two electrodes. at this point the cell reaches a new state and lose permanently the capability to come back in its initial pristine state. Now the channel structure is irremediably present in the cell and even triggering the opposite process, by applying the positive polarity on the Au top electrode, it is impossible to destroy it, but only to interrupt it in the very proximity on the top electrode (bottom-right in Fig. 2.18a).

From an electrical point of view, the Electroforming process can be represented by the *I-V* curves in Fig. 2.18b. For this purpose, a current compliance of 5 mA was set and a continuous voltage sweep by applying a triangular voltage ramp in the negative polarity was performed. As it can be observed by the curves, for small voltages, the behaviour follows the one of the Schottky barrier, but, as soon the oxygen ions starts to migrate and the inner structure of the oxide begins its variation, there is an increase in the conductance. At a certain point the current abruptly reaches the compliance value: this is the sign the Electroforming process has happened and the channel is finally bridging the two electrodes. At this point, the voltage reaches its maximum negative value, as imposed by the ramp and in the comeback phase, the current is now fixed

at its maximum allowed value, $5\,\text{mA}$, because now the conduction is no more through the insulating layer and attributed to ionic motion and recombination, but is completely due to the electrons inside the channel. The conductivity of the channel now it is so high the only at very small voltages, so approaching zero, the linear nature of the current can be correctly visualise. Now, the devices are finally in the low resistance state (LRS).

It is important to mention that, relatively high voltages are necessary to trigger the Electroforming process, in this case, high variability is present since it could happen between $-15\,\text{V}$ and $-21\,\text{V}$. Moreover, the Electroforming curves show the Electroforming process can start by applying lower compliance currents, such as $1\,\text{mA}$, but, at these currents, the Electroforming process is not completed or ensured for all the devices: the majority of them require current compliance well-above $3\,\text{mA}$.

2.3.3 The switching mechanism in $Au/NbO_x/Nb$
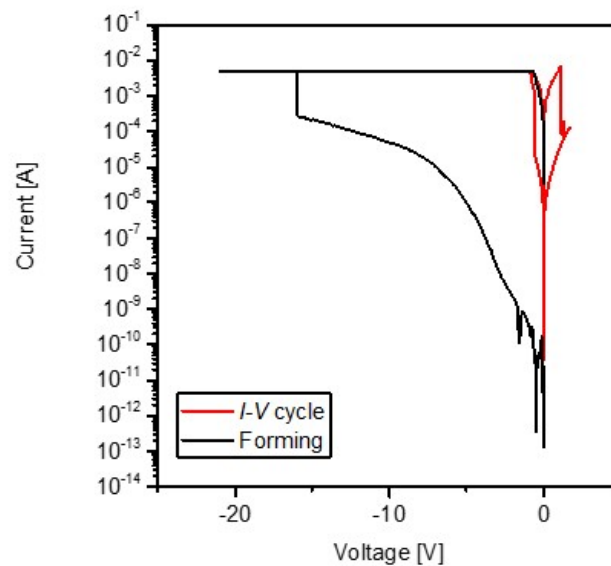
Fig. 2.19 Typical *I-V* curves related to the Electroforming (black) and resistive switching cycle (red). Once the Electroforming has occurred, the HRS is different from the initial pristine state.

In Fig. 2.19 a representation of the effect of the Electroforming process with respect to the subsequent *I-V* cycles can be observed from an electrical point of view. In this plot, there is the typical Electroforming curve (black) of one of the devices under test superimposed with the typical shape of the typical SET and RESET (red) of a complete cycle. At a first sight, it is evident that the effect of the Electroforming process produces is into change the resistance state of the cell. Before the Electroforming, the black curve describes current values very small if compared to the current values associated to the device in what is called the high resistance state (HRS). This is a proof that the Electroforming process produces an irreversible and permanent change in the structure of the oxide layer or in other words, that a channel is realised along it.
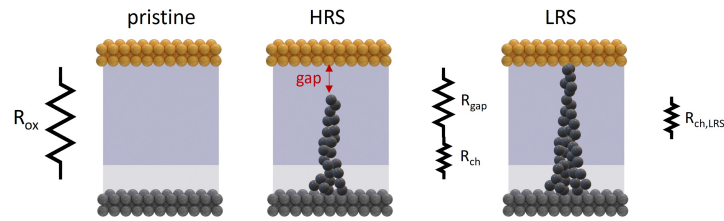
Fig. 2.20 Schematics of Pristine state vs HRS. On the left side, the device in its pristine state characterised by the high resistance of the oxide layer. In the centre, the same device when the Electroforming occurred and the HRS is recovered: now the resistance of the device is given by the series of the channel and the gap, which for obvious reason is lower of the initial pristine state oxide resistance. On the right, the LRS characterised by the low resistance of the channel. (In the electrical scheme the contact resistances related to the electrodes and the barriers at the oxide interface have been neglected.)

This is better shown in Fig. 2.20, where the device resistance has been differentiate from the situation before the Electroforming (pristine state) and after, once the HRS has been recovered. At the beginning the oxide resistance is very high and is characterised by R_{ox}, after the HRS recover, the channel is permanently inside of the oxide and a gap separate it from the Au TE. Both the channel and the gap posses their own resistances, R_{ch} and R_{gap} and in this situation, the device resistance is given by the series of them. In conclusion, by the qualitative comparison of the two it derives:

$$R_{ox} > R_{ch} + R_{gap} \tag{2.4}$$

The dis-equality in **2.4** explains the difference in the current magnitudes between the pristine state and the HRS shown in Fig. 2.19.

The describe model is very simplified and it describes only qualitatively the behaviour of the LRS and HRS. More in general, someone can realize a model taking into account the whole cell and considering the Resistance of the cell before and after the Electroforming process, but this time involving all the resistances we introduced before. When the cell is in its pristine state, the resistance associated with it is:

$$R_{cell} = R_{ox} \tag{2.5}$$

After the Electroforming process, the channel is still immersed in the oxide matrix, which still maintain its higher pristine resistance, so that it is possible to consider the channel resistance in series with the gap resistance, and this series results in parallel with the pristine resistance, so that, the cell resistance in the OFF state becomes:

$$R_{cell} = R_{ox} \oplus (R_{ch} + R_{gap}) \tag{2.6}$$

Where the symbol $\oplus$ denotes the harmonic sum, or the mathematical operation correspondent to the parallel between two resistances. IN this way it results:

$$R_{cell} = \frac{R_{ox}(R_{ch} + R_{gap})}{R_{ox} + R_{ch} + R_{gap}} \tag{2.7}$$

Now, it is not so difficult to observe that the quantity multiplying R_{ox} is lower than 1 and in this way it is demonstrated that the resistance in the OFF state after the Electroforming is lower than the initial pristine state one. the study of the resistive switching capability and behaviour of the $Au/NbO_x/Nb$ devices has been carried out through different electrical tests which include the well known endurance and retention, which are the major figures of merit in the study of the typical resistive switching devices [32]. In addition the possibility of multilevel programming has been tested.

Endurance

The endurance test is one of the most common and exploited test to study the switching performances of a memristive devices. Once the device is formed and suitable operative conditions for the switching have been found, it is possible to study the evolution of the *I-V* curves through the cycles. The meaning of this test is first of all to observe if it is possible to trigger consequently a SET and a RESET for a very high number of cycle, without any missing state, and, second, study the electrical properties of the cell in each cycle.

In this case, being this a preliminary study on this particular anodic oxide based cells, a continuous voltage sweep has been used to describe the voltage ramp in each cycle. Being the application of a continuous voltage ramp a time consuming process, an endurance test like this can be considered good if the number of cycles reaches at least one thousand units, on the contrary, in the literature are reported endurance test of million of cycles, but achieved exploiting a different electrical measurement, based on train of pulses. [89] The exploitation of train pulses, as described in the Electroforming section, is a different method to study memristive devices, especially if someone is interested into study the dynamics of the process, which is not the case of the devices under test.
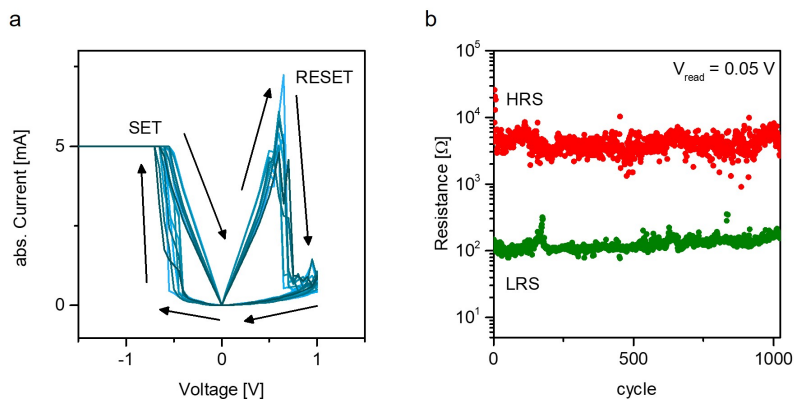
Fig. 2.21 Endurance test on Au/NbO$_x$/Nb devices. a) *I-V* curves at sample cycles: 1st (lightest), 128th, 256th, 384th, 512th, 640th, 768th, 896th, and 1024 (darkest). b) HRS and LRS read for each cycle at the voltage V$_{read}$= $-50\,$mV.

An example performed on an Au/NbO$_x$/Nb device is reported in Fig. 2.21a, where samples *I-V* curves are reported after a 1024 cycle endurance. Here, from the lightest to the darkest the cycles 1, 128, 256, 384, 512, 640, 768, 896, and 1024 are represented with surprising low variability in terms of shape and slope of the *I-V*. The arrows in the plot indicate the direction of the voltage sweep, which starts in the negative polarity, where the SET is achieved approximately around -0.6 V with a current compliance of -5 mA and the RESET is reached in the positive polarity around 0.5 V. The linear behaviour close to the origin (in both polarities) is a confirmation the conduction in the LRS (after the SET and before the RESET) occurs through a metallic channel and due to the electrons flow across it, whilst, after the RESET is reached and the device is in its HRS, the current decreases and the shape of the *I-V* indicates the conduction is meanly described as tunnelling through the gap between the channel and the TE.

In order to study the possible memory effect related to this device, jointly to the *I-V* curves, the resistances can be studied. The study of the resistances associated to the LRS (the ON state) and the HRS (the OFF state) can be carried out in different ways. Usually, this resistances are directly extracted by reading the current at a specific voltage value, for each cycle, has occurred in this case, in which the current has been read at the voltage -50 mV, choosing preferentially the negative voltage being the SET process occurring in the negative polarity. The LRS is, by definition, the resistance associated to the device after the SET event, instead the HRS is assumed as the resistance of the device, at the same voltage, after the RESET event. From the analysis of the *I-V* curves of the 1024 cycle endurance test, once the currents at the voltage -50 mV have been recorded, the HRS and the LRS have been evaluated through the Ohm's law, after suitable linearization of the characteristics under test around the reading voltage. From this analysis, the resistances related to the LRS and the HRS are 126 Ω and 4.2 kΩ respectively, with an average OFF/ON ratio of 33.
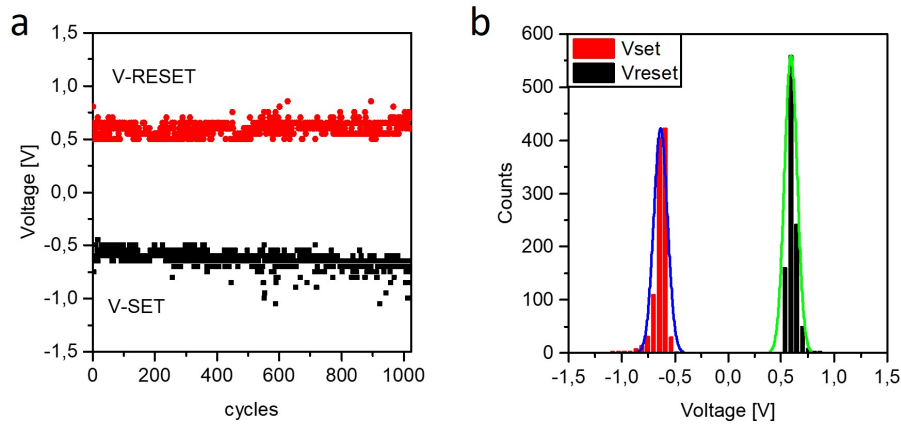
Fig. 2.22 SET and RESET voltages in Au/60 nm NbO$_x$/Nb devices. a) cycle by cycle and b) cumulative distribution.

Another important information derived from the analysis of the endurance curves are the SET and the RESET voltages. These quantities represent the threshold voltages for the switching from OFF to ON and ON to OFF states respectively.

The definition of the SET and the RESET voltage it is possible for CF-based devices, for which the transition OFF to ON (or vice versa) is not analogic, so there is a net variation between the characteristics in the two states. Several model have been proposed for ECM, VCM and TCM devices for the description of the SET and the RESET processes and as a consequence for deriving the expressions of the SET and the RESET voltages, but despite these models there are mainly statistical-based, we should define a proper method for the acquisition of these two important quantities. [90]

The operation of extraction of the SET and the RESET voltages is for obvious reasons, strongly related with the typology of the measured devices and on the characteristic *I-V* curves collected, so that, each experiment requires its proper method for the definition of the SET and the RESET voltages. Giving a look to the devices measured in this experiment and in particular on the collected *I-V* curves, it is possible to observe that the transition from the OFF state (HRS) to the ON state (LRS), or in other words, the SET process, is nearly abrupt and, once the current reaches the value of the compliance for the first time, the device persists in this state, meaning the process is successfully

happened. This means, in this case, it is possible to assume the SET voltage as the first voltage at which the current reaches the value of the compliance current.

For the RESET process, something similar happens: in this case the transitions are nearly triangular-shaped and the RESET voltage can be assumed as the voltage at which the RESET starts. Looking at the curves in Fig. 2.21a, this translates into collect all the voltages at which the current assumes its maximum value in the positive polarity.

Given this premise, it is finally possible to determine the SET and the RESET voltages related to the device under test.

Fig. 2.22a show the collection of the SET and the RESET voltages with associated statistical distributions. In particular, the average SET and RESET voltages are found to be $-0.6\,\mathrm{V}$ and $0.6\,\mathrm{V}$ respectively. These are relatively low values. Not only, the Gaussian distributions superimposed to the statistical histograms in Fig. 2.22b show the low variability of these programming voltage conditions over the whole endurance experiment.

Retention

The retention is another figure of merit in the study of RS devices. This type of measurement are usually designed to show the capability of a programmed device of staying in the ON or in the OFF state when a small external bias voltage is applied. In principle the meaning of the small bias voltage is to have a quantity to read the current and extract the resistance, and having a small voltage means the energy introduced by the external field is not enough to give rise any kind of phenomenon related to the ion conduction. The experiment which is carried out in this case is very simple: once a device survived the endurance test, it can be switched into the ON state by performing only the SET process, at this point, the small constant voltage bias is applied and the current is measured over time. Usually the experiment lasts when the device switches in the opposite state, so from LRS to HRS, or more in general, when the resistance varies over a certain imposed limit. The same is done for the opposite OFF state. First the device is subjected to a forced RESET, then if the device is still able to switch, a further SET and a subsequent RESET are performed. Now the device is in the HRS. The same procedure is applied

to evaluate the current, and so the resistance in this OFF state: the same constant bias voltage is applied and the current is measured over time for the same time interval as the previous measurement. The values of HRS and LRS are extracted from the currents collected over time by using the Ohm's law.
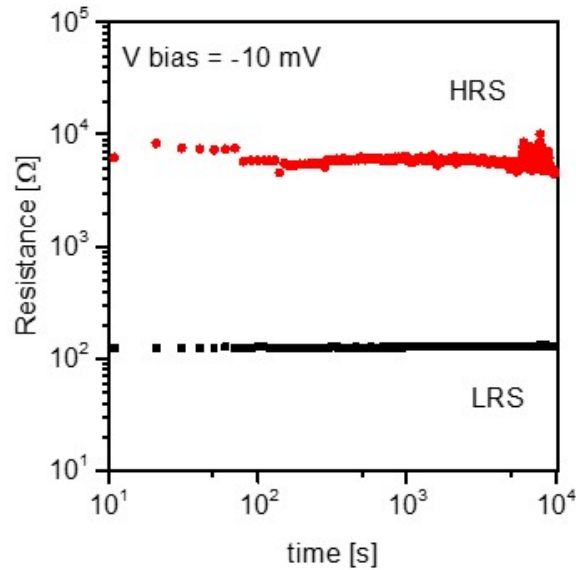
Fig. 2.23 Retention test for the Au terminated devices.

In Fig. 2.23 a typical retention experiment is shown. The two resistance states, HRS and LRS are determined by reading the current in the OFF and ON state respectively, using a constat bias voltage of $-10\,\text{mV}$. The experiment was carried out for $10\,000\,\text{s}$. In this case, the measurement of the LRS is very stable in time. For the HRS, however, some fluctuations starts to appear in the final part of the experiment, going toward $10\,000\,\text{s}$, but the values of these resistances are in the range of the whole experiment.

Multilevel Analysis

The possibility to switch between the HRS and the LRS (and vice versa) is strongly related to the operational condition used to program the devices, or in other words, on the voltage range and the compliance currents. From an experimental point of view, when the switching is related on the formation

and rupture of a conducting bridge, as in the case of $Au/NbO_x/Nb$ devices analysed in this chapter, the values of the HRS result independent on the compliance current chosen to SET the devices, this has been already observed in the literature .[91] This is easily demonstrated by observing the eq.**2.7**, where being $R_{gap} \gg R_{ch}$, it results :

$$R_{HRS} \approx R_{gap} \tag{2.8}$$

So in principle, it is possible to consider HRS almost independent on the choice of the compliance.

Instead, the LRS is strongly influenced by the compliance current chosen for the SET process, in fact, the bigger the compliance current and the bigger should be the section of the filament, and as a consequence, the resistance in the LRS should progressively decrease by reducing the compliance current. This can be experimentally demonstrated by observing what it happens to a one of the devices under test when different compliance currents are chosen to perform the SET process during the endurance test.[92]
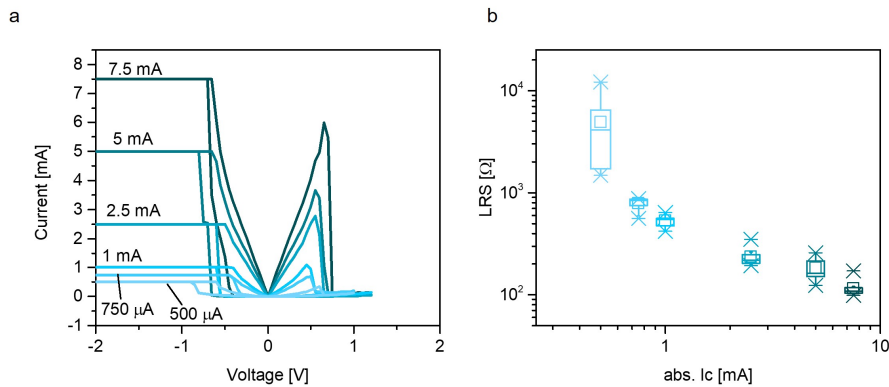
Fig. 2.24 Multilevel analysis in Au terminated devices. a) Series of *I-V* curves (medians over 10 cycles endurance test) obtained at different CC. b) Box-plots collecting the LRS of the endurance test.

Figure 2.24a shows a collection of *I-V* curves related to the median of consecutive 10 cycles of a $Au/NbO_x/Nb$ device performed exploiting different compliance current for the SET processes. In the specific, six different com-

pliance currents where chosen: 500 µA, 750 µA, 1 A, 2.5 A, 5 A and, 7.5 mA. Jointly to the *I-V* characteristics, the LRS have been extracted to show the direct effect the current has on the electric properties of the cell. The LRS in Fig. 2.24b show the main effect of the compliance current, the reduction of the LRS with this almost exponential behaviour in log scale. Interestingly, the LRS show low variability at higher compliance current, meaning the filament in the ON state in more stable, instead at very low compliance current, high variability is present, this is not so weird and an explanation can be found looking at the *I-V* curves in Fig. 2.24a, where at I$_c$ = 500 µA the behaviour of the current in the come back phase of the SET is strongly non-linear. The evolution of the LRS with the compliance current opens to the possibility to exploit different level of resistance by changing the current. The evolution can be in such a way important, because, excluding the smallest compliance current which produce a very non-linear SET, the LRS evaluated at 750 µA and at 7.5 A differ of one order of magnitude each other. The choice to use a current not higher than 7.5 A is to ensure the RESET operation. The multilevel capability has a drawback: if the compliance current used to program the device in the SET process is too high, the filament can result very hard to break in the RESET process, so that no more than 7.5 mA are eligible in this case. The contrary can be concluded for the lower limit too: apart from the strongly non-linear behaviour in the SET process, the main problem is related to the difficulty to achieve a stable SET when the compliance current is reduced to much, in this case 500 µA seems to represent a lower limit for this process. Differently from the devices tested for the endurance test in the previous section, in this case the device has been initially programmed using the lowest compliance current, 500 µA. Once the compliance current is set for the "level", the device is initially subjected to 10 cycles, then, after the stabilisation, 10 cycles are recorded for the test. The voltage sweep conditions are the same as the previous endurance tests, meaning only the compliance current is varied in this case.

Device-to-Device variability

The device-to-device variability is usually performed to test the capability to program devices fabricated on the same substrate and verify both the program-

ming condition are correct for their proper functioning and at the same time, to verify that the variation in the collected properties can be considered small. In order to test the device variability, 10 test device have been chosen from different region of the sample. These devices have then been electro-formed and programmed following the programming condition described in the previous sections. In the end the end, it has been decided to collect the values of HRS and LRS related to a 10 consecutive cycles test.
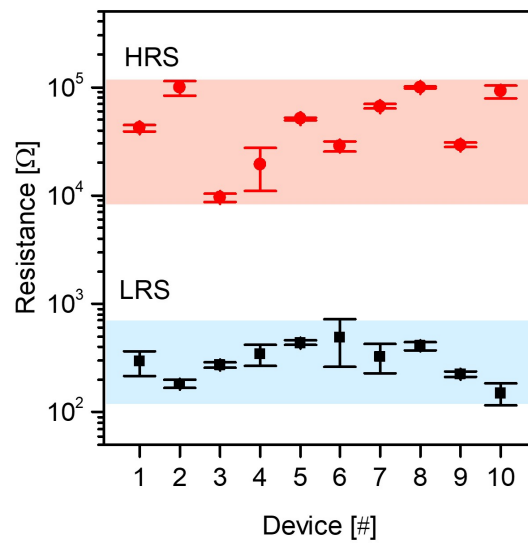
Fig. 2.25 Device-to-device variability in Au/(60 nm)NbO$_x$/Nb devices.

Figure 2.25 shows the average values related to the HRS and LRS of the devices under test, read at a voltage of -50 mV. It is interesting to observe that, despite the different investigated region, the electrical properties are not affected from a high variation, in fact, the LRS, seems to be very stable, less than a order of magnitude is present between the maximum and the minimum collected values. The same cannot be concluded for the HRS, which is affected by a little bit higher variability. In addition, this test shows the possibility to visualize the memory window of the Au/NbO$_x$/Nb devices from a collective point of view. The two highlighted regions are not superimposed and show a gap in between them, demonstrating that it exists a separation between the high and the low resistance states. The memory window is not so large, because, usually, a good separation between the on and the off states is represented by at

least two order of magnitude in current, and conversely in the resistances.[32] Moreover, it is possible to enhance the memory window capability by finding suitable operation conditions: for example, by the previous multilevel test, it was possible to observe the possibility to reduce the LRS, so by increasing the compliance current it is possible to enlarge the memory window acting on its lower limit. The same cannot unfortunately done for the upper limit: working with a fixed size devices it is not possible increase the HRS by acting on the compliance, because intrinsically this resistance is associated to the resistance of the cell and the gap, and not on the one of the channel, so it is not possible to increase it operating on the current. A possible method can be instead to operate on the size of the cell: if we reduce the size of the electrode, the resistance in the OFF state should increase, but in this case it is necessary to find new operative condition for the programming operation of the cells. [93]

2.3.4 Quantized effect in Au/NbO$_x$/Nb devices

The last experiment presented in this chapter is related to the observation of the quantum conductance properties observation of the Au/NbO$_x$/Nb devices. In principle, the observation of quantum properties is possible when the dimensions of the channel formed in the device are small enough to give rise quantization phenomena when a specific properties is observed. In the case of a memristive device, the observation of quantum phenomena is meanly related on some quantization effect which can be observed during the measurement of the conductance of a device. Before starting with the description of these part it is important to specify that the observation of quantized effect in conductance is possible in micro-metric devices when the working principle at the basis of the switching is the formation and rupture of a conducting bridge inside of the cell. So that, the electrons are able to move in a sufficiently small structure, that we are able to describe their conduction at a mesoscopic regime. At this point it is clear that, even if the devices studied have a micro-metric size ($50\text{x}50\,\mu\text{m}^2$), any effect of quantization in the conductance can only be associated to the electron conduction through a nano-metric filament/channel, otherwise impossible to be observed at such dimensions.[94]
In the case of Au/NbO$_x$/Nb devices, the observation of quantized properties of the conductance is possible under specific measurement conditions. The

idea in this experiment is to trigger the SET process under relatively slow voltage (or current) sweeps, differently from what happen during the normal operation condition of a device, in which the SET and the RESET processes are usually very fast. The reason must be searched in the mechanism itself: if the SET process is carried out very slowly, at the same time the completion of the channel should happen at the same velocity and this should mean the evolution of the conductance in time should reflect the slow changes in the channel morphology. In other words, the device starts from its HRS and the channel is progressively reconstructed by triggering a slow voltage (current) sweep, but this process is so slow that even the evolution in the conductance is slow and effect in the quantization becomes visible because progressively in the filament more channels become available to the electron conduction.
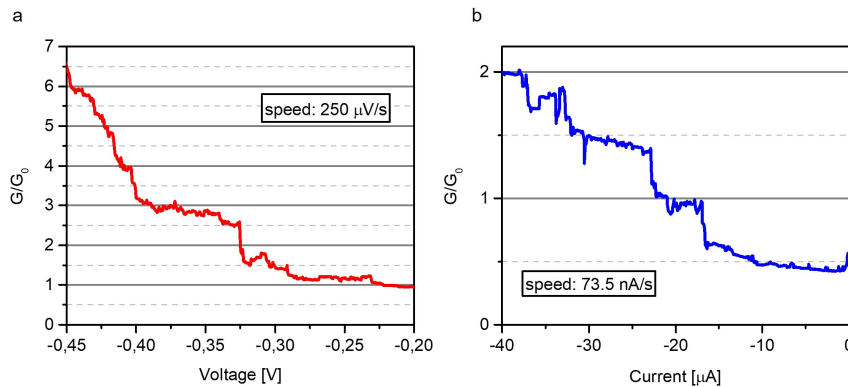
Fig. 2.26 QPC analysis in Au terminated devices. Through a) slow voltage and b)slow current sweeps the observation of quantized effect in conductance is possible.

The plots in Figg. 2.26a-b show that through the slow voltage and current sweeps it is possible to give rise to steps in the conductance (here reported as normalised with respect to $G_0 = 2e^2/h$, the conductance quanta). At a first sight, it seems that by triggering this process exploiting slow current sweeps leads to a better observation of the possible quantum states. There is no a specific reason on why this happen, but, in principle, of the two processes the one taking place thanks to the current produce a major number of steps. This means in other words, the process should carried out slower than the voltage initiated one. The origin of this difference can be searched in the different

mechanism giving rise to the electromigration. Differently from the canonic electromigration triggered by the voltage sweep, in which the electric field is moving ions through the solid electrolyte, when the current is exploited, the electrons are injected and slowly transfer energy to the atoms in the solid electrolyte causing their displacement and movement. For this reason it should be not so difficult imagine why of the two processes, the current can lead the slowest movement atoms and formation of the channel.

Another important aspect to be discussed is why steps are observed in conductance during this experiment whilst in the previous ones the *I-V* characteristics look continuous and no discretised. In this case the reason is simple: discretisation arises from the size of the channel. In the case of macroscopic channels, or in other words, channels where no effects of electron confinement occur, the electrons are free to move in the three directions and this give rise to a continuous *I-V* characteristics. When the dimensions of the channel are reduced, as in the case of small currents used for the SET process or in the case of slow voltage/current sweeps in which the formation of the channel is triggered atom by atom leading to a physical constriction in its morphology, then the lateral dimensions become sufficiently small to be under the Fermi wavelength of the material and the density of states of the electron of the channel changes description because now there is electron confinement along the lateral dimension. In addition, the length of the channel, which is physically determined by the thickness of the oxide layer, results to be greater than the electron main free path along it. This two morphological properties of the channel make it what is called a mesoscopic conductor, a particular electronic structure in which electrons move through a ballistic motion. In this particular ballistic regime condition, the electron current flowing through the channel is well described by the Landauer-Büttiker formula [95]:

$$I = \frac{2e^2}{h} \int_{\varepsilon_F}^{\varepsilon_F + eV} T(E)(f_L(E) - f_R(E))dE \qquad (2.9)$$

In this expression, the quantity *T(E)* represents the transmission coefficient and describe the probability to transfer an electron along the channel. This probability depends on the energy, *E* and on the temperature *T*, even if in the equation this dependency is not reported. This probability is multiplied by the difference of the Fermi function of the two electrodes: when an energy

difference between them exists, or in other words an external voltage is applied, one of the two, the Left one or the Right one, is at a greater energy and a net flux of electron starts to flow from that electrode to the other one. The factor $2e^2/h$ is the afore mentioned G_0, the conductance quanta, an universal constant given by the ratio of the square of the electronic charge and the Plank constant. The factor 2 represents the spin degeneracy of the electrons able to flow in the channel. It is important to notice that this formula is only valid for a single channel transmission and it can be simplified in the case the temperature approaches to the zero limit to:

$$I = \frac{2e^2}{h} \int_{\varepsilon_F}^{\varepsilon_F + eV} T(E)dE \tag{2.10}$$

when the electron energy is sufficiently close to the Fermi energy, that is true in the case of the electrons flowing across the channel, the transmission probability becomes almost independent from the energy and the formula further simplify to:

$$I = \frac{2e^2}{h} T(\varepsilon_F)V \tag{2.11}$$

Where, $V = \dfrac{\mu_L - \mu_R}{e}$ is the external applied voltage from which the difference between the chemical potential of the two electrode arises.
If at this point multiple parallel channel are considered, the transmission probability becomes a discrete quantity and the final current becomes:

$$I = \frac{2e^2}{h} \sum_n T_n(\varepsilon_F)V \tag{2.12}$$

The quantity:

$$G = \frac{2e^2}{h} \sum_n T_n(\varepsilon_F) = G_0 \sum_n T_n(\varepsilon_F) \tag{2.13}$$

represents the quantized conductance. The effect of the discretization is in the summation over $T_n(\varepsilon_F)$ which is represented by a staircase function that gives rise to the typical steps observed in Figg. 2.26a-b (see Appendix A for

more exemplary curves).

The previous **2.12** expression and with reference to the Figg. 2.26a-b, it can be concluded that slow current or voltage sweeps originate nano-metric sized channels and that the electrons flowing through them are moving in a confined structure.

Chapter 3

Effects of the electrode material on the RS properties of NbO$_x$-based devices

Reference paper:

[96]*LEONETTI, Giuseppe, et al. Effect of electrode materials on resistive switching behaviour of NbOx-based memristive devices. Scientific Reports, 2023, 13.1: 17003.*

3.1 Introduction

In the previous chapter, the material properties of anodic NbO$_x$ have been investigated through morphological, structural and chemical characterisations and, through suitable electrical measurements, the functionalities of Au/NbO$_x$/Nb devices based on the anodic oxide have been investigated. In this chapter, the attention will be focused on how the switching capabilities and properties of the memristive devices based on anodic NbO$_x$ are influenced by the choice of the top electrode material and on the thickness of the oxide layer. For this aim a selection of five different materials (including Au) will be proposed for the realisation of VCM memristive devices. The purpose of this study is trying to find a possible selection rule for the realisation of memristive devices based on anodic NbO$_x$.

3.2   Methods

For the realisation of a VCM cell, there is the necessity to choose a TE material that is inert or characterised by nearly immobile ion species in the operative range of the device. In other words, there is the intrinsic need of select a material that is characterised either by a very low or absent chemical reactivity with the NbO$_x$ layer. This means that, the dissolution processes that can take place at the interface with the TE, can be characterised by either not relevant degree of dissolution or the ionic species generated by it are characterised by a very low ion mobility. Under this premise, ions can be considered immobile in the range of applied voltage exploited to program and use the cell, and the electric field is not able to drive them across the oxide layer. For example, Pt and Au can be considered to chemical inert materials with respect to NbO$_x$, which means that at the interface with them, no REDOX reactions take place, so no dissolution process happens.[97, 98] Instead, Nb or Ir, that are two transition metals, are expected to chemically react with other transition metal oxides to produce their own oxide. This has already been discussed in the previous chapter in the chemical analysis section reporting the chemical composition at the interface of the BE showing the Nb reacts with Nb$_2$O$_5$ to produce NbO. But, even if a chemical reaction takes place at the interface, Nb ions are characterised by a very low ion mobility to be driven by the electric field, so they can be practically considered immobile. For the realisation of the NbO$_x$-based VCM cell described in this chapter, the choice of the TE materials fell on Au, Pt, Ir, TiN and Nb. In principle, Au, Pt and Ir are three of the highest work function material: the high work function at the interface of the oxide layer should increase the resistance of the cell because it is expected a high Schottky barrier that should limit the transfer of electrons. TiN has a different nature: in principle it is not a pure metal, but it is a ceramic material largely exploited in electronic to be a good contact material, but it is a low oxygen affinity material, which means it is a perfect candidate to be interfaced to NbO$_x$as TE. Last, but not least important, Nb: this metal is the same as the BE, the necessity of this material is to have a comparison with totally symmetric structure. For these experiments, only the effect of the TE material on the switching condition will be considered, but in addition, it will investigated how the switching properties vary by reducing the oxide thickness but keeping constant the TE area.

Thickness	Au	Pt	Ir	TiN	Nb
60 nm	✘	✘	✘	✘	✘
30 nm	✘	✘	✘		

Table 3.1 Summary of the NbO$_x$-based sample realised, highlighting the combinations of oxide thicknesses and the TE materials.

3.3   Sample Fabrication and Characterisation
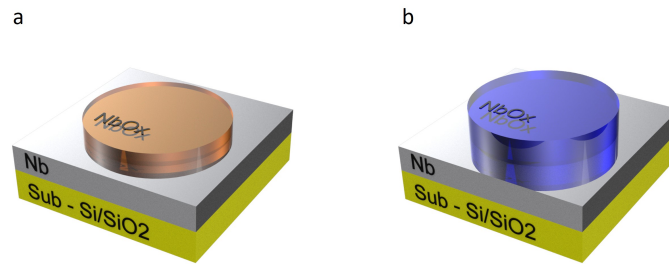
Fig. 3.1 Sample after the anodic oxidation process. a) 30 nm and b) a) 60 nm NbO$_x$: different anodizing voltages translate into different oxide thicknesses and appearance from an optical point of view.

For this experiment VCM cell based NbO$_x$ devices have been realised varying the oxide thickness and the TE material, according with the scheme reported in Table table 3.1.

8 17×17 mm^2 samples were realised following the procedure described in the previous chapter. Each sample was first subjected to a Nb deposition (250 nm) exploiting the apparatus described in the section 2.1.2. Immediately after the deposition, the samples were subjected to the anodic oxidation process to grow the oxide layer in the central region according with the set-up and the modalities described in 2.1.3, in particular, two different oxide thickness were realised, nominally 60 nm and 30 nm, exploiting the anodizing voltages 20 V and 10 V respectively. Fig. 3.1 shows how the different samples appear after the anodic oxidation processes depending on the voltage used to growth the oxide.

Neither chemical nor structural analysis was performed on the samples, but a check of the thicknesses was done to verify the effectiveness of the anodic oxidation process. The thickness check was performed through the optical

Sample	TE	V_{anod} [V]	t_1 [nm]	t_2 [nm]	t_3 [nm]	t_{avg} [nm]
#1	Au	20	56	56	61	58
#2	Pt	20	60	60	60	60
#3	Ir	20	59	59	59	60
#4	TiN	20	58	59	58	58
#5	Nb	20	57	64	58	60
#6	Au	10	30	30	30	30
#7	Pt	10	29	29	29	29
#8	Ir	10	29	29	29	29

Table 3.2 Summary of the NbO$_x$-based sample realised, highlighting the combinations of oxide thicknesses and the TE materials. The thicknesses were evaluated through the integrated software of the optical ellipsometer by fitting the acquired spectra.

Sample	TE	*target*	P_{dep} [mbar]	*Power* [W]	Ar_{flux} [sccm]	N_{2flux} [sccm]	t [nm]
#1	Au	Au	$5 \cdot 10^{-3}$	100	53	-	150
#2	Pt	Pt	$5 \cdot 10^{-3}$	200	30	-	50
#3	Ir	Ir	$2 \cdot 10^{-3}$	30	20	-	50
#4	TiN	Ti	$1 \cdot 10^{-3}$	200	27	3	50
#5	Nb	Nb	$3 \cdot 10^{-3}$	110	50	-	150
#6	Au	Au	$5 \cdot 10^{-3}$	100	53	-	150
#7	Pt	Pt	$5 \cdot 10^{-3}$	200	30	-	50
#8	Ir	Ir	$2 \cdot 10^{-3}$	30	20	-	50

Table 3.3 Parameters used for the deposition of the TE materials of the 8 samples described. The samples #1, #5 and #6 were realised at INRiM laboratories, the other ones at RWTH university of Aachen.

ellipsometry (alpha-SE Ellipsometer J.A. Woollam). The thicknesses derived from the fit of the optical measurements are reported in Table table 3.2).

3.3.1   TE definition

Each one of the previous sample went toward an optical lithography process for the definition of the TE. The samples #1, #5 and #6, for which the fabrication process was completely carried out at the INRiM laboratories (QR lab), the direct laser writing process was chosen, different TE sizes were realised ($1000{\times}1000\,\mu\text{m}^2$, $500{\times}500\,\mu\text{m}^2$, $100{\times}100\,\mu\text{m}^2$ and $50{\times}50\,\mu\text{m}^2$). Whilst, for the

other samples, the conventional UV lithographic process was carried out at the RWTH university, to define TEs with the same sizes, including a further set of smaller electrodes with dimensions $25{\times}25\,\mu m^2$.

The deposition of the TE materials were performed exploiting the sputtering deposition according with the data in Table table 3.3.

3.4   Pristine state analysis
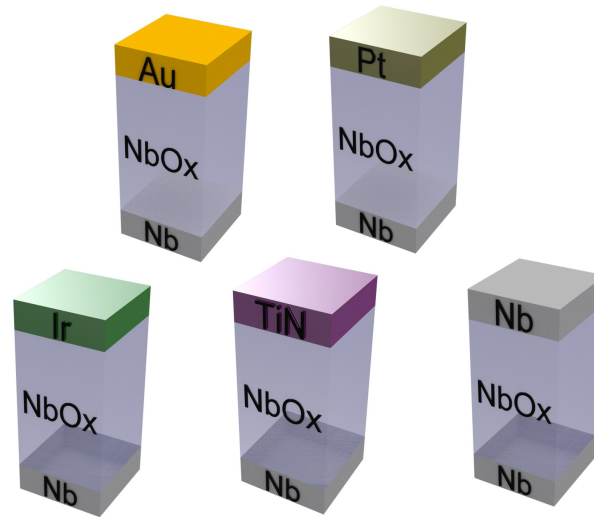
Fig. 3.2 Cell structure of the first test. Vertical device structure was defined by the stack of the three material: Nb (BE), NbO$_x$ (central layer, 60 nm), TE. The size of the TE is $50{\times}50\,\mu m^2$.

This analysis was carried out to show how the different TE materials influence the electronic transport of the cell fabricated in the previous section and whose related scheme is visible in Fig. 3.2. This preliminary test was performed on the first 5 samples (#1, #2, #3, #4 and #5), with the nominal oxide thickness of 60 nm. For the other three samples the shape of the *I-V* characteristics is expected to be the same, but with a different order of magnitude of the current, due to the fact that by reducing the oxide layer thickness, the associated resistance of the cell is expected to reduce.
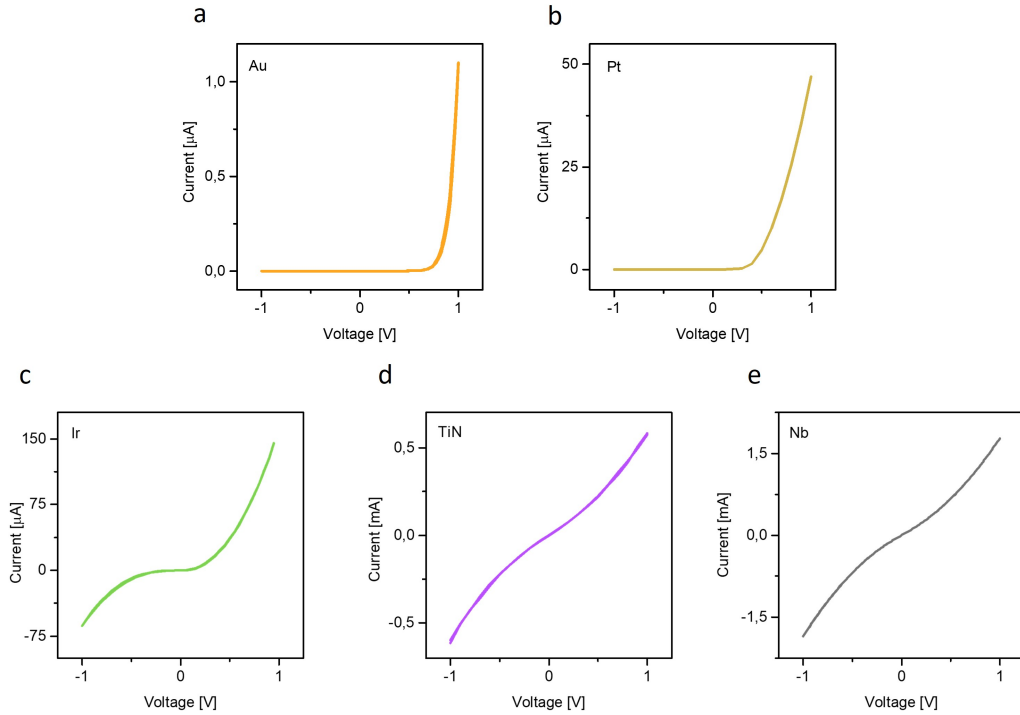
Fig. 3.3 Pristine state characteristics for the different TEs. a) Au, b) Pt, c) Ir, d) TiN and e) Nb.

Fig. 3.3 show how the different TE materials affect the electronic transport in the pristine state. The curves were acquired considering exemplary *I-V* characteristics from one device for each TE material, for the TE size of $50 \times 50 \, \mu m^2$. The electrical characteristic was acquired in the range $[-1 \, V; 1 \, V]$ with a voltage step of $0.01 \, V$. During each measurements, the Nb BE was kept to ground and the continuous voltage sweep was directly applied on the TE material. The reason of this choice in the acquisition of the *I-V* characteristics is to not give rise any kind of switching process.

As the pristine state curves show, the electronic transport at the interface of the TE is strongly regulated by the material used to terminate the devices, that in this case is the only discriminant differentiating each cell. In other words, the difference between each pristine state relies in the different nature of the barriers arising at the interface TE/NbO$_x$. A preliminary discussion

for the Au and Nb TE has been done in the section 2.3.1: it was previously described the behaviour of the Nb BE which act as an Ohmic contact, whilst, on the contrary, the TE material gives rise to a Schottky barrier contact. It was previously said that the Schottky barrier can be modelled from an electrical point of view with a diode. Now, the situation is very similar: alongside Au and Nb there are Pt, Ir and TiN that have mixed behaviour. At a first sight, Au and Pt qualitatively act in the same way, being characterised by a pronounced blocking character in the negative polarity and very high conductivity in the positive one (Fig. 3.3 a-b). This is the well-known rectifying behaviour and is typical of the diodes. Nb and TiN (Fig. 3.3 d-Fig. 3.3 e), on the contrary, seem to exhibit a very conducting and linear behaviour, that is typical of the metals: for the Nb, at the interface with NbO_x the contact is ohmic-like, the presence of a very small Schottky is still present due to the very attenuate curvature in the *I-V* characteristics, but in principle no blocking character is exercised from the two interface and the electronic conduction seems to be unaffected from them. The pristine state of the TiN terminated devices is from a qualitative point of view the same of the Nb terminated devices. The only appreciable difference in this case is in the measured current, which seems a little bit lower in the case of TiN. For this material similar consideration of Nb can be done and assume we have an Ohmic contact at the interface with NbO_x too. The last material, Ir (Fig. 3.3 c) shows intermediate behaviour with respect to the first two noble metal and the last two good ohmic contacts. Ir seem to give rise to some kind of Schottky barrier at the interface of the top interface with NbO_x, the negative branch of the *I-V* characteristics exhibits the typical curvature with exponential-like behaviour, whilst in the positive branch it is evident the linear ohmic behaviour due to the Nb contact on the bottom. But, the problem is related to the order of magnitude of the current flowing in these two branches: they are practically the same, the only discriminant is in the shape of the current. In principle, it can be concluded that Ir acts as a Schottky contact on the top side, but its blocking character is not so high and to give rise to any kind of rectifying behaviour.

metal	Φ_M [eV]	$\Phi_B=\Phi_M$-χ [eV]	Cont. type	Ref.
Au	$5.1 \div 5.4$	1.45	Schottky	[99, 100]
Pt	$5.7 \div 6.35$	2.23	Schottky	[99, 100]
Ir	5.25	1.45	Schottky	[99]
TiN	$4.2 \div 4.5$	0.55	Ohmic	[101]
Nb	4.3	0.5	Ohmic	[100]

Table 3.4 Metal work function Φ_M and barriers Φ_B for each type of TE material exploited in the realisation of NbO$_x$ memristive devices.

3.4.1   The effect of the metal Work function

From a physical point of view, having treated of the Schottky barriers at the interfaces of the TEs and the Nb/NbO$_x$ BE interface, it is clear that it is necessary to investigate what causes the rise of these barriers. Usually, a barrier arises at the interface between two materials because of a difference between the work function/electron affinities of the two materials (without explicit the nature of them, because they can be two metals, two insulators or an insulator and a metal). The higher this difference and the higher the resulting barrier should be, with consequent lower current values in the pristine state. Among the possible materials that can be implemented in the fabrication of the TEs, it was decided to choose the ones characterised by the highest work function, in order to achieve the most insulating pristine state.

Data in table 3.4 show the different metal work function Φ_M related to the metal exploited as TEs in the devices described in this chapter. The metal work function is a physical quantity whose meaning is related to the extraction work of an electron, in other words, it represents how much energy is required to bring an electron from the Fermi level of a metal and transport it up to the vacuum level (outside the material). For the insulating materials, instead, a different quantity is generally associated, but with a very similar meaning, the electron affinity χ. This quantity should not be confused with the one defined for the atoms. For insulators (and semiconductors) χ is the amount of energy required to bring an electron from the bottom of the conduction band toward the vacuum level. When an insulator and a metal are interfaced together, as it happens looking at the interface of the TE of these devices, a barrier arises due to the difference of these energy contributes and because we are in

presence of two different material reaching the thermodynamic equilibrium. The highest this barrier is, the more difficult is for the electron to be extracted from the metal and across the interface when an external bias voltage is applied. Following this reasoning, to the highest work function materials it should be associated the highest blocking power. In Table table 3.4, Pt, Au and Ir are the most high work function material with associated highest barrier Φ_B. If on the one side, someone expects a similar trend between the barrier and the pristine state, it should be surprised of the different behaviour and scenarios that open looking on the experimental data. In principle the pristine state should reflect the effect of the barrier and it should be expected the lowest pristine state current for Pt, followed by Ir and Au with the same order of magnitude. Surprisingly, it seems to be a small discrepancy between the theoretical aspect of the barrier and the measured current. In this case it seems that from a pure physical point of view it is not possible to find an explanation. Another possible contribution that can be considered is for example in the chemistry at the TE/NbO_x interface: with high probability, the three materials interface the NbO_x in different ways and this translates in very dissimilar behaviour when looking to the electron transport phenomena. Let's start with Au and Pt. Apparently, Pt should give rise to a higher barrier than Au, but from an experimental point of view, the pristine state of Au is more insulating. In the literature this is not uncommon, for example there is the case of Ag that, even if is a material characterised with a lower work function of Au, in the devices $TE/CuO_x/Cu$ gives rise to a more insulating pristine state.[102] This means the chemistry and the quality of the interface between two materials alter the canonical behaviour due to the Schottky barrier arising from the barrier height generated by the difference between the two extraction works. In other words, the generation of electronic states arising from the surface states interacting together, or the presence of trap states due to point and/or structural defects, the charge transfer effect due to the different molecular species at the interface, the non-spatial uniformity in the deposition of the metal layer, can all singularly or jointly contribute to this apparently anomalous behaviour.[103]

The Ir is probably the most noticeable material among the three high work function TE: it has the same work function of Au, but the barrier arising at the interface with NbO_x seems to be much lower rather than it. Same assumption about the quality of the interface can be done for this material, but differently

fro Au and Pt, Ir is able to oxidize. In the nature oxides of iridium exist in different oxidation states, as any other material able to oxidize, but the most stable one is IrO_2. Given this premise, it is not so strange to think Ir coupled with NbO_x or any other oxides (especially a TMO) is able to form its own oxide. There is no experimental proof from this side to ensure the presence of IrO_x at the interface with the TE, but it is reasonable to assume its presence or the presence of intermediate compounds generated by the chemical activity of this material with the NbO_x. Ir was at the beginning chosen because it is an immobile atomic species when it comes to describe the switching behaviour, but we do not exclude the possibility of it to react at the interface. In the literature, it is described that Ir is able to react with Nb to form metallic intermediate compound such as Ir_3Nb as result of the reduction mechanism at whose Nb^{+5} is subjected when Nb_2O_5 is interfaced with Ir [104]. This can in some ways explain why the theoretical Schottky barrier reduces for this TE.

For TiN and Nb, the type of contact at the interface with Nb_2O_5 can be assumed as Ohmic, the pristine state plots and the and barrier heights are a proof of this, in particular, for Nb this has been exhaustively discussed in the previous chapter, describing the formation of NbO at the interface between the two materials, for TiN, experimentally, the behaviour is similar to Nb, so we can conclude it acts as an Ohmic contact.
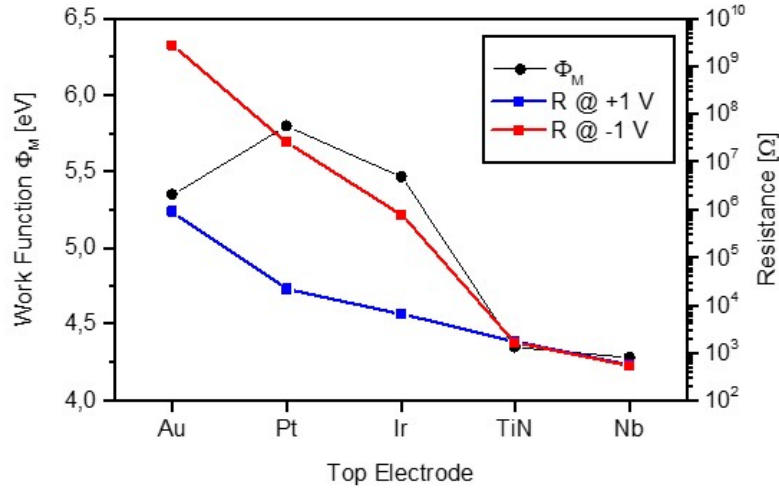
Fig. 3.4 Resistances and work functions comparison for the different TE materials.

To conclude this description, the resulting resistance of the cell was evaluated for the different TE material at the values $+1\,\mathrm{V}$ and $-1\,\mathrm{V}$, directly applying the Ohm's law at the reading voltage. Fig. 3.4 show how the different resistances of the cells are distributed dependently on the TEs. This is a complementary analysis with respect to the *I-V* characteristics, and its main purpose is to highlight that the resistance of the cell, in both polarities is regulated by the barriers arising at the interfaces with the oxide. Moreover, these differences in the resistances can arise from the point defects due to the structure at the interface that regulate the ionic and the electronic transport. What is evident is that there is a trend between the resistances evaluated at the two reading voltages, in particular, for the high work function materials, at least two order of magnitude there exist in the passage from negative to positive polarity, where the diode like character of the cell is expected to favour the conduction. Whilst, for the Ohmic contact, symmetric behaviour in the pristine states gives rise to symmetrical resistances of the same order of magnitude.

3.5   Electroforming process

The initialization of the cells starts with the Electroforming process. In the previous chapter 2 this has been described for the Au TE, now the analysis is repeated in order to compare the effect of the different electrode in this process. A first guideline to this process can be given from the considerations on the chemical analysis and the Electroforming process of the Au/NbO$_x$/Nb cells described in section 2.3.2, where it was underlined the scavenger effect promoted by the presence of the Nb BE interfaced with NbO$_x$ layer. In particular, the BE interface is able to act as a reservoir of oxygen ions and during the Electroforming process, they are most favourable to travel and accumulate at that interface, where the chemical analysis showed an impoverishment in the oxide composition. For this reason, even if the Electroforming process can be promoted in both polarities, it is better to study it by reverse polarizing the different cells under test, by applying a negative voltage ramp directly on the TE while the Nb BE is kept a constant ground voltage (the ground of the instrument).
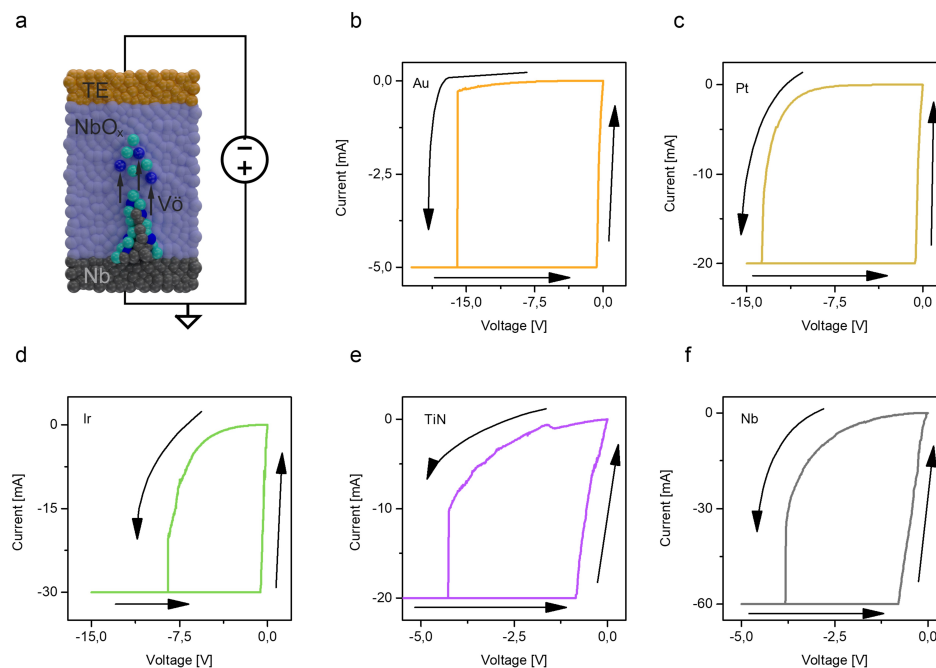
Fig. 3.5 Electroforming process for the $60\,\text{nm}$ NbO_x devices. a) Schematisation of the channel formation during the application of the negative voltage bias sweep. Electroforming *I-V* curves for the different TE material: b) Au, c) Pt, d) Ir, e) TiN and, f) Nb.

Figure 3.5 show how the different TE materials affect the Electroforming process of the cells under test. Apparently this process should involve the oxide layer only because the ion movement that is at the basis of the process itself take place in this layer. Like in the pristine state analysis, even in this case the TE plays an important role into regulating the goodness and the possibility to have the channel formation. First of all, we can describe the process of the channel formation in a more general way, even if this has already done for the Au-terminated cells. Figure 3.5a how the channel is formed starting from the BE toward the TE. The description proposed in the previous chapter can now be generalised to the different TE materials, but where is the difference between the chosen materials? It is worth mentioning that to allow the Electroforming process, a specific voltage ramp with a proper amplitude (in the negative

polarity in this case) is necessary, jointly to a CC which limit the amount of maximum current flowing across the device. The CC has two main purposes:

- prevent damages on the devices

- set the maximum section of the channel

Looking at the plots in Figures 3.5b-f it can be seen that dependently on the material used for the TE, each cell requires different CC to activate the process. In the graphs they are reported Electroforming processes exploiting CCs that are enough to give rise the process and the behaviour of these currents in some ways reflect the previous pristine state trend. As it can be observed, the CC required to form the channel is expected to increase the more conducting the cell is, this means that for materials such as Au and Pt, that characterize the most insulating cell in the pristine state, the CC required are smaller.
The process can be described looking the I-V characteristics: in the initial phase, the current follows the behaviour of the Schottky barrier at the interface TE/NbO$_x$, until a sufficiently high voltage, the Electroforming voltage, is reached. In correspondence of this voltage value, the current experiences a jump and reaches the value of the imposed CC. When this happens, the channel is formed and is bridging the two metal electrodes. At this point, the voltage is further increased toward the maximum negative value and the sweep is completed by reversing the polarity reporting it to zero. In doing this, the current is due to the electron conduction through the channel and, dependently on its conductivity it can be high enough to exceed the value of the compliance, that why during the comeback phase it saturates. When the voltage approaches to zero, the current that should follows the Ohm's law, becomes smaller than the compliance and the I-V characteristics starts to variate again, showing a linear-like behaviour. The different orders of magnitude in the current can be in principle related to the pristine states of the different materials, but in this alongside the transfer process across the interfaces it must be considered the ion movements across the oxide layer, and what it is evident in this experiment is that different TE materials alter the rapidity at which the Electroforming process happens. For example, Au and Pt requires very high voltages to form the channel, meaning these two materials make more difficult this process, or in other words slower. Whilst, TiN or Nb, that are more conducting, favour the

electronic transfer making this process more efficient and happening at lower voltages.

As previously discussed, Ir, but this can be also applied to other materials such as TiN, regulate their transport at the interface with the TE/NbO_x interface by chemical reactions, especially REDOX reactions that involve electrons exchange. For example it was previously mentioned the possibility of Ir to form Ir_3Nb, but the same can happen for TiN, that in a similar way of the TiN/HfO junctions can form TiO_x and TiON, at the same time can produce different compounds with NbO_x, that in this case act to favour the Electroforming process.
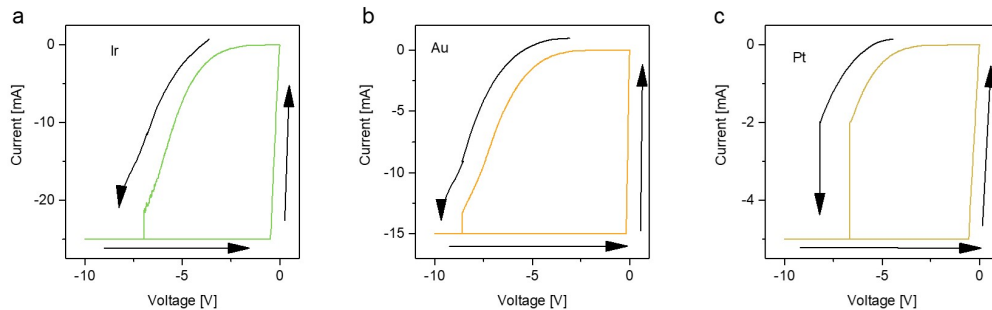
Fig. 3.6 Electroforming *I-V* curves for the 30 nm NbO_x devices terminated with a) Ir, b) Au, and c) Pt.

For the sake of completeness, alongside the Electroforming curves of the 60 nm NbO_x devices, the ones related to the high work function materials but for the 30 nm NbO_x devices are shown. In figure 3.6 three exemplary plots are shown. As it can be seen, no variation in the behaviour of the current can be observed, the only difference are in the Electroforming voltages, this time lower, and in the CC regulating the process itself.

3.5.1   Electroforming voltages comparison

The Electroforming process can be considered as a properties of the aforementioned cells, because it is regulated both by the physics and the chemistry of the interfaces, apart to oxide layer. So it is interesting to analyse how the forming voltage varies with the five considered materials. Apparently it seems the CC regulate the process, but it does it without altering the Electroforming process.

This means that the Electroforming process can happen at specific voltages just dependently on the involved materials and dimensions of the device.

A more detailed analysis of the forming voltages have been done by collecting the data of the different devices in this process. For this purpose, the Electroforming voltage was assumed as the first voltage at which the compliance current was reached.
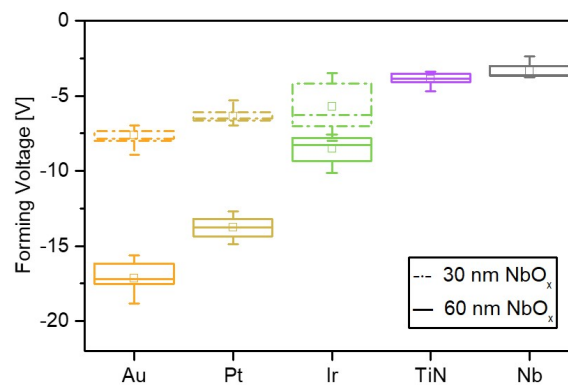
Fig. 3.7 Box-plot distributions of the Electroforming voltages for the different TE materials for the two investigated oxide thicknesses.

Fig. 3.7 show the forming voltages collected as box plots. The plot is divided in two parts: the solid line box-plots refer to the previously 60 nm devices, divided by colour dependently on the TE, whilst, the dashed line ones refer to the 30 nm devices. For the 30 nm NbO$_x$ devices only Au, Pt and Ir have been considered as TEs, this is due to the fact that only for these three materials it make sense to have switching, but this will be clear in the next section.

What is important from this analysis is that there is a trend between the forming voltages and the pristine state resistances, in fact the most insulating cells in the pristine states are also the ones characterised by the highest forming voltage. It is interesting to observe that when the thickness of the oxide layer is reduced by half of its initial size (30 nm), the forming voltages reduce, but the trend is still maintained. Although, this should not surprise, and it is

$metal$	t_{ox} [nm]	# dev.	$V_{F,avg}$ [V]	CC [mA]
Au	60	12	-17.17	5
Pt	60	10	-12.54	20
Ir	60	15	-8.51	30
Au	30	10	-7.63	15
Pt	30	15	-6.35	5
Ir	30	10	-6.05	25
TiN	60	12	-3.89	20
Nb	60	12	-3.35	60

Table 3.5 Specifics of the devices considered for the Electroforming process.

an experimental evidence on the fact that the theoretical forming voltage is expected to reduce when the thickness of the oxide layer is reduced, or when the size of the TEs is increased (Note that both the two design choice contribute to alter the initial pristine state resistance by reducing it).[105]

For the Electroforming experiments described in this section and in the previous section 3.5, different cells have been considered. The specifics are collected in table 3.5.

3.6   Effect of the electrode metal on the Resistive switching behaviour
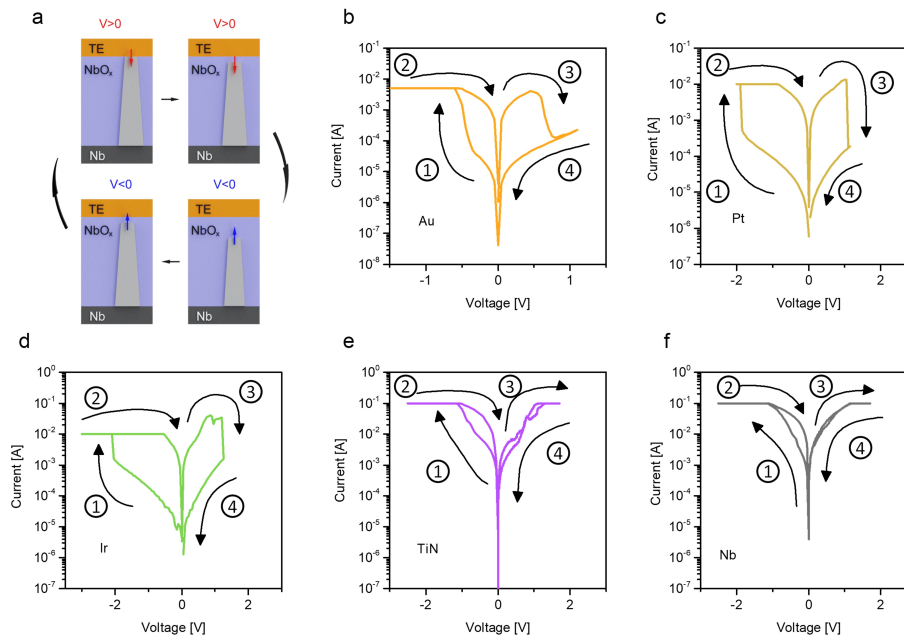
Fig. 3.8 RS mechanism in NbO$_x$-based VCM cells. a) Schematisation of the switching process dependently on the applied voltage: the Switching involves the rupture/formation of the channel close to the TE interface. Exemplary *I-V* curves (log-scale) for the typical RS behaviour of the TE materials under test: b) Au, c) Pt, d) Ir, e) TiN and, f) Nb. The numbers and the arrows in the plots indicate the sweep evolution.

In the section 2.3.3 the mechanism of RS has been described for the Au-terminated device. For the other VCM cell characterised by a different TE material, the process is exactly the same. What is worth mentioning is that, differently from the Electroforming process, characterised by localised REDOX but along the whole oxide with the main purpose of realise the channel, here, the process involves once again localised REDOX reaction, but close to the TE interface. A schematisation of this process can be found in Figure 3.8a. Here it can be seen how the channel withdraws (blue arrow) or grow (red arrow) toward the TE interface, dependently on the applied voltage, which governs the activation of the REDOX reactions and the oxygen ion movement (here

not represented).

The RS mechanism can be directly observed through the electrical measurements since it involves the global variation of the cell resistance between the HRS (channel interrupted) and the LRS (channel completed) and *vice versa.* The switching behaviour has been shown for the $60\,\text{nm}$ NbO_x devices to first analyse if it is possible to have any kind of switching phenomenon inside the oxide layer. For the Au, Pt and Ir TEs in Figures 3.8b-d it is clear the possibility to have resistive switching and with bipolar behaviour, characterised by a SET process in the negative polarity and a RESET in the positive one. For the other two TE materials, TiN and Nb, instead, no switching process is possible. The plots in Figure 3.8e-f show how in the positive polarity no RESET is achieved, meaning that, after the forming process, usually these cells go toward a permanent SET. This is an experimental evidence on the fact that to have resistive switching behaviour in a memristive device, the MIM structure should be designed in a way that one of the two electrodes should establish a Schottky contact and the counter one an Ohmic contact. That is the case of Au, Pt and Ir. But, for TiN and Nb, having Ohmic contacts on both sides disables the switching capability.[106, 107] In the next subsections the behaviours of the single cells, depending on the TE will be analysed showing the main switching properties.

3.6.1   Switching behaviour of the $Au/(60\ nm)NbO_x/Nb$ cells

Fig. 3.9 RS behaviour in $Au/60\,nm$-NbO_x/Nb devices.a) Endurance test with exemplary. b) HRS and LRS collected for each cycle at the reading voltage $V_{read}=-0.2\,V$. SET and RESET voltages cycle by cycle c) and distributed in histograms d).

The RS behaviour of the $Au/(60\ nm)NbO_x/Nb$ devices was analysed in the previous chapter, here a second test was carried out showing the capability of switching, but for a lower number of cycles (200). The measurements have been stopped with purpose at the 200th cycle, because in this case the main interest was into study the stability of the device and its switching capability more than the possibility to have high endurances. In the Fig. 3.9a exemplary

curves at specific cycles (the first one, the 50th, the 100th, the 150th, the last 200th) are reported with superimposed median. At a first sight, these devices seem to be characterised by high reproducibility in terms of *I-V* curves, that even after a high number of cycles seem to superimpose one to each other and with the median, here assumed as more statistical correct description to group all the collected curves. Fig. 3.9b shows a collection of HRS and LRS related to each cycle and extracted directly by reading the resistance value from the curves using the Ohm's law. The LRS looks stable and with values of the order of 10^2 Ω instead for the HRS values of the orders of tens of $k\Omega$ are registered. The HRS seems to stabilize after the first half of the experiment. For what concern the SET and the RESET voltages, the plot in Figg. 3.9c-d show the distribution cycle-by-cycle and the statistical distribution with histograms. The Au-terminated cells seem to be characterised by low and symmetrical SET and RESET voltages with very low variability.

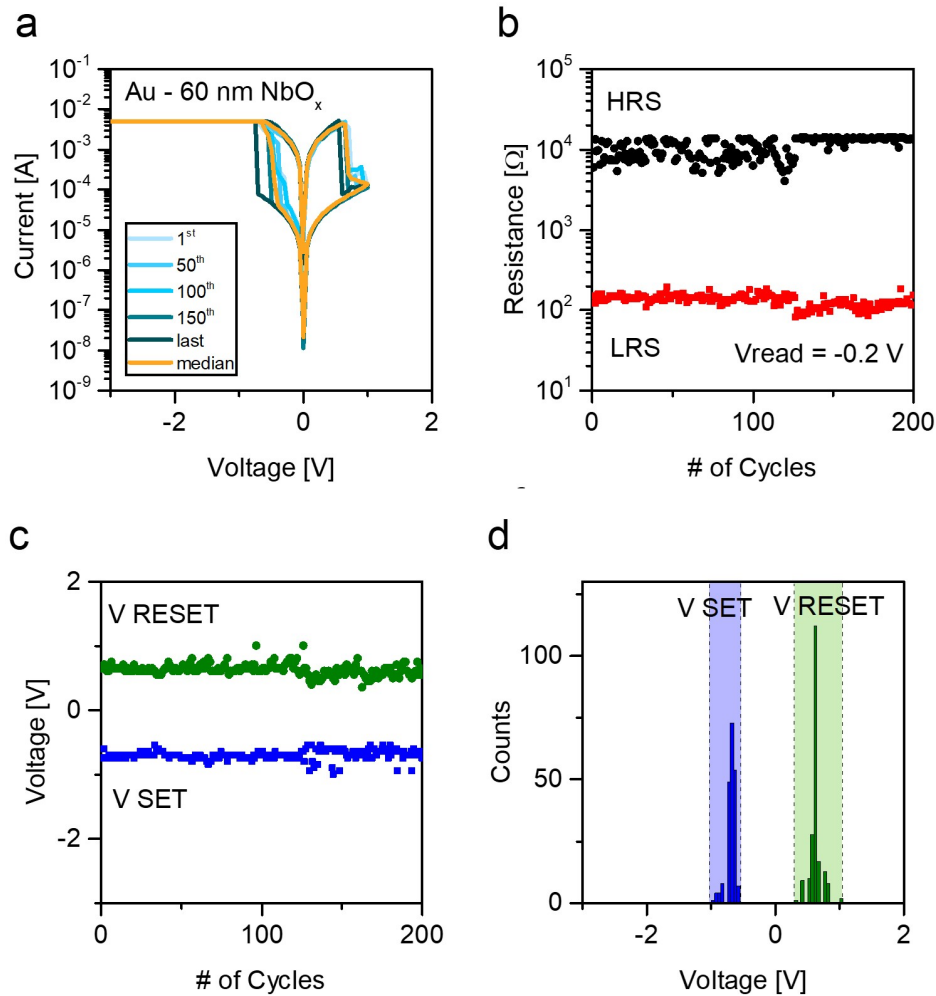## 3.6.2 Switching behaviour of the Pt/(60 nm)NbO_x/Nb cells
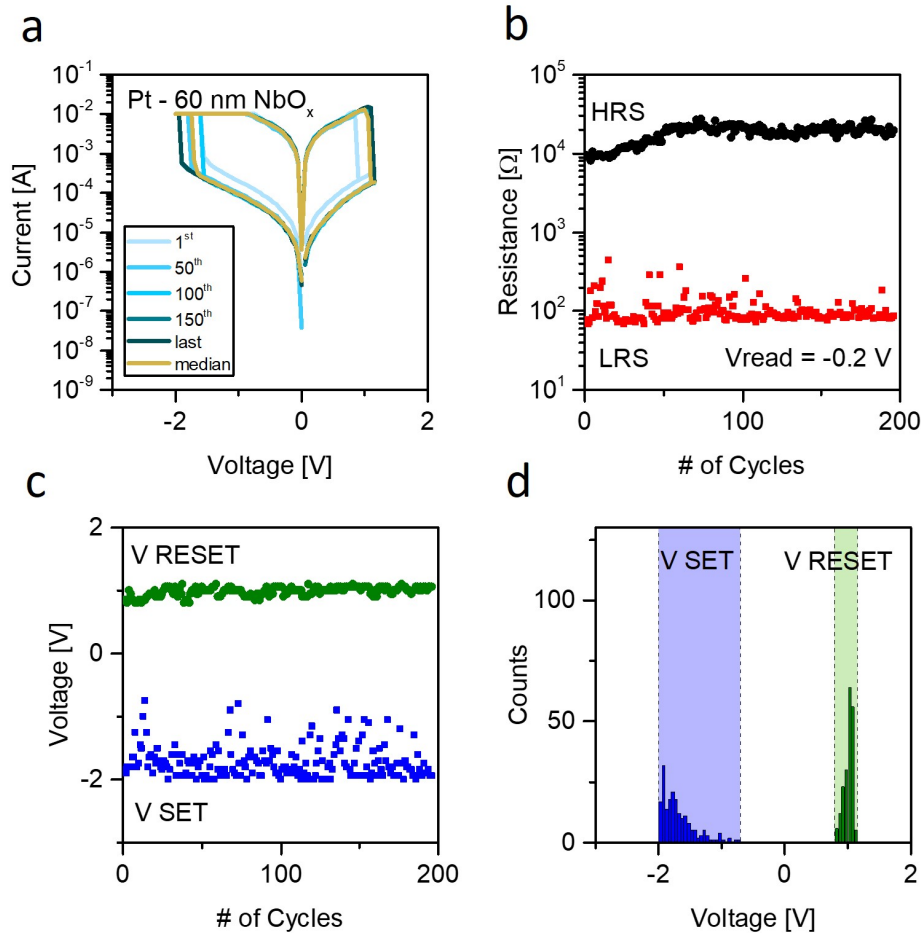
Fig. 3.10 RS behaviour in Pt/60 nm-NbO_x/Nb devices.a) Endurance test with exemplary. b) HRS and LRS collected for each cycle at the reading voltage $V_{read}=-0.2\,V$. SET and RESET voltages cycle by cycle c) and distributed in histograms d).

The same test was repeated for the Pt-terminated cells and 60 nm NbO_x. A similar consideration can be deduced for these devices when talking about the cycle by cycle stability: for the *I-V* curves, Fig. 3.10a show good reproducibility and superimposition with the median curve. Even in terms of LRS and HRS there is good stability, the values are compatibles with the one of the previous analysed Au-cell, but with a LRS which results less stable in the initial switching events. Nevertheless, good separation between the two states exists with at

least two order of magnitude, as shown in Fig. Fig. 3.10b. Alongside the good stability in terms of resistances, the Pt terminated devices are characterised by a low variability RESET voltage, a little bit larger than the Au one, on the contrary a large SET voltage characterised by very high variability. The plots in Figg. 3.10c-d demonstrate the presence on SET/RESET events in terms of voltages with the distributions of the SET voltages that is broadened in a large range between -2 and -1 V, making these cells able to switch, but with a SET which is not predictable.

3.6.3 Switching behaviour of the Ir/(60 nm)NbO$_x$/Nb cells
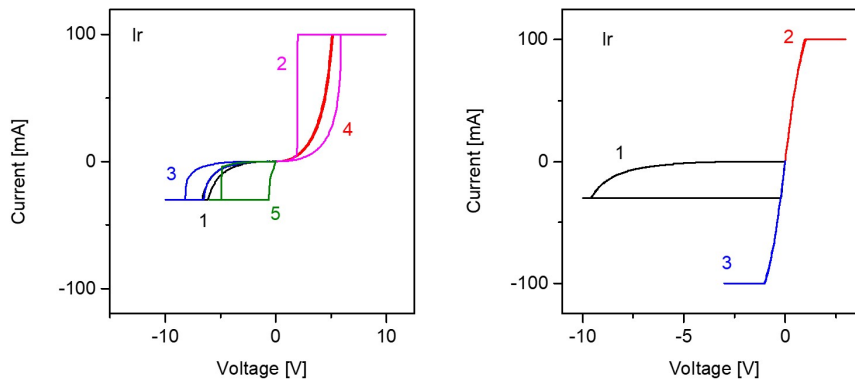
Fig. 3.11 Two different behaviours in the RS of Ir-terminated devices. a) Instability given by the difficulty into reach The SET in a specific polarity, even changing the CC. b) Permanent SET leading to the impossibility to RESET the device after the Electroforming process. The numbers indicate the order in which the voltage sweeps are temporally performed.

Differently from the Au and the Pt devices, the Ir-terminated one show the possibility to switch, but not in a stable and in a predictable way. Figure 3.11a shows how the switching in a Ir terminated device looks like when the device is able to give rise to any specific switching phenomenon. What it is clear is that no specific SET or RESET in a given polarity is highlighted, meaning that there is no bipolar switching behaviour. At the same time, neither unipolar behaviour

is detected. These devices can SET and RESET in both polarities. Another trend for these devices is shown in Fig. 3.11b where, after the Electroforming process, the device goes toward a permanent SET which is impossible to be recovered in the opposite polarity, where the CC (the maximum allowed one by instrument, 100 mA) is reached. For this reason, it is not interesting to study the behaviour of the Ir-terminated devices at lower oxide thicknesses. Although, Ir is a largely employed material in the catalysis and, it cannot be excluded a good switching behaviour of these devices if studied in a different environment, for example in a controlled environment setup in which it is possible to set both the temperature and the moisture level. In this study, all the cells have been studied in the laboratory environment that can be subjected to interesting variation of both the temperature and the moisture, but it is interesting to observe that, differently from the other materials that seem to be unaffected by these variations, Ir does. [108]

3.6.4   Switching behaviour of the TiN and Nb terminated devices in 60 nm NbO$_x$ cells
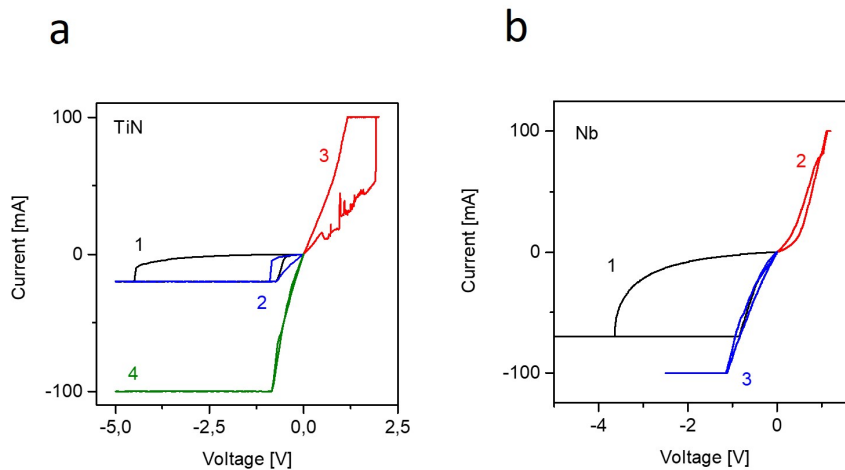
Fig. 3.12 RS behaviour in a) TiN and b) Nb terminated cells. In both cases the type of contact established at the TE interface does not allow the possibility to have switching in the cell, leading to a permanent SET after the electroforming process, that is impossible to be recovered in the opposite polarity (or in the same). The proof is the reaching of the CC. The numbers indicate the order in which the voltage sweeps are performed.

For TiN and Nb terminated devices, the type of switching has been discussed in terms of the type of contacts at the interface. To have bipolar switching it is necessary to generate an asymmetry in the cell, not only due to materials involved, but also in the type of the established contacts. TiN in such a way is able to produce asymmetry in the materials, but is not able to establish a sufficiently high barrier at the TE interface, and the result is that it acts as an Ohmic contact on the TE, like Nb on the bottom one. For sure the asymmetry in the type of materials can be distinguished when comparing its RS behaviour with Nb, in fact, differently from what happens in the case of Nb, that after the Electroforming process goes toward a permanent SET (Fig. 3.12b), in the TiN terminated devices there is a tentative to recover the HRS, but in unstable way as shown in Fig. 3.12a, where after a difficult Electroforming process in which the SET was not completely achieved, a second cycle has been necessary to SET the device. Immediately after that, the RESET process tempted to be completed, but the device SET once again of a higher level, reaching the compliance in the positive polarity, in the end, a further cycle in the positive polarity showed the impossibility to RESET the device being the current reaching the maximum allowed level in the negative polarity. To conclude, TiN and Nb, are definitively not good TE material in the realisation of VCM cell devices based on NbO_x and for this reason is not interesting to observe the effect of RS properties or capabilities when the oxide thickness is reduced.

3.6.5   Switching behaviour of the $Au/(30\ nm)NbO_x/Nb$ cells

Once studied the effect of the different TE materials in the 60 nm NbO_x cells, now RS behaviour will be analysed at reduce oxide thickness. In particular, the nominal 30 nm NbO_x cells will be considered and for the Au and the Pt terminated devices. Ir devices will be not considered due to their instability as previously seen and because, when the dimensions are reduced, the cells become more conductive and keeping the TE area constant, this means is more difficult to achieve the switching. For this reason, it is interesting to study the RS at reduced dimensions only for Au and Pt.

Fig. 3.13 RS behaviour in Au/30 nm-NbO$_x$/Nb devices.a) Endurance test with exemplary. b) HRS and LRS collected for each cycle at the reading voltage V$_{read}$=−0.2 V. SET and RESET voltages cycle by cycle c) and distributed in histograms d).

Surprisingly, the Au-terminated devices have a bad switching behaviour when the NbO$_x$ thickness is reduced. A proof of this in the plots of Fig. 3.13a-d. In the Fig. 3.13a an exemplary curve showing the typical RS cycle of these devices is shown. There is still bipolar switching, with the SET in the negative polarity and the RESET in the opposite one. But, the endurance tests last after few cycle and are not able to reach hundred of consecutive SET/RESET, in addition there is no good separation between the HRS and the LRS. Fig. 3.13b show how these devices act when an endurance test is performed with the same modalities of the thicker devices. In the initial half of the experiment, the SET is always reached, and with stable values, but the

RESET is distributed randomly, meaning that at each cycle the RESET is not completely reached, after a certain number of cycles, the device stops working: The SET is permanently reached with no possibility to recover the HRS, the test shows that, even if further cycles are performed, there is no possibility this device switches again. The device-to-device variability was here studied to show that this was not just a behaviour due to a bad cell, but that these devices are really difficult to be used and even if they work, their endurances last after few cycles. For this endurance experiment, the same electroformed cells of the forming were studied. Of the previously formed devices the maximum numbers of cycles achieved to have a comparison between them was 20, after that it was really difficult to make them switch. Of the studied cells, only 4 devices survived and the results of the SET7RESET voltages and the HRS/LRS have been collected in the box-plot shown in Figg. 3.13c-d. At a first sight, these devices have good RESET voltages, characterised by low variability, on the contrary, the SET varies in a large range of $1\,\mathrm{V}$ or more, but with an average value that make them symmetric. For the HRS and the LRS, the bias window is not so large, but a separation between the two resistance states exists. The LRS seems to be more stable and characterised by low variability differently from the HRS. To conclude, the $30\,\mathrm{nm}$ NbO_x devices terminated with Au are not so good as the same devices but with thicker oxide, that is why is not so interesting to use them at reduced dimensions if only the oxide thickness is reduced. This means it will be interesting to study what does it happen in the case of both the thickness and the TEs area are reduced.

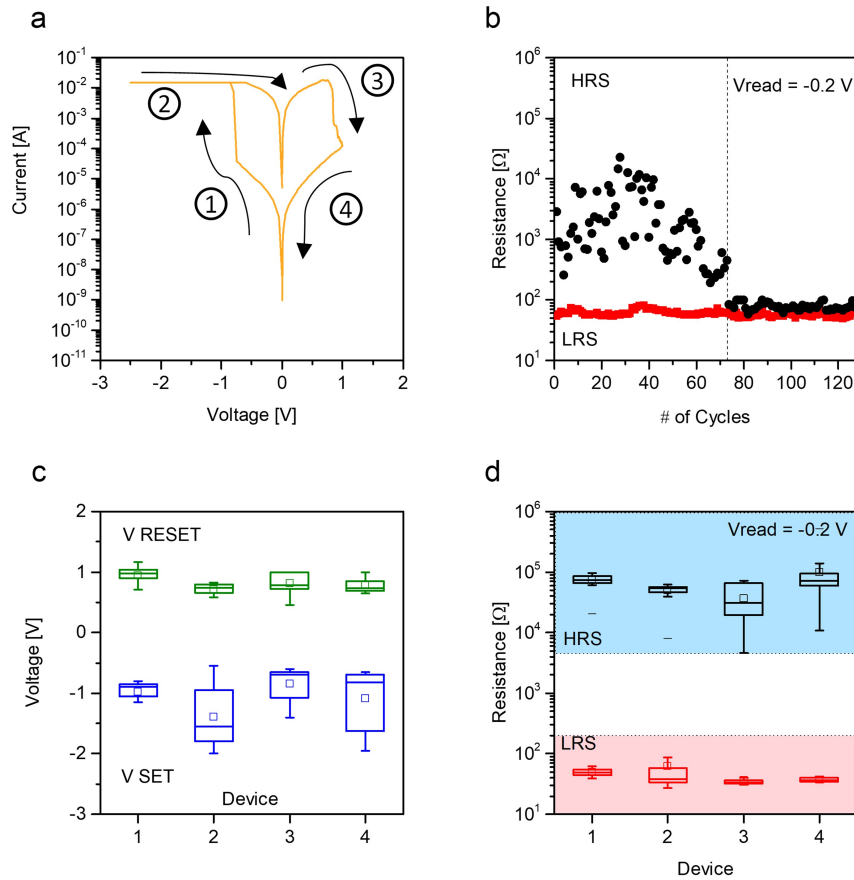### 3.6.6   Switching behaviour of the Pt/(30 nm)NbO$_x$/Nb cells
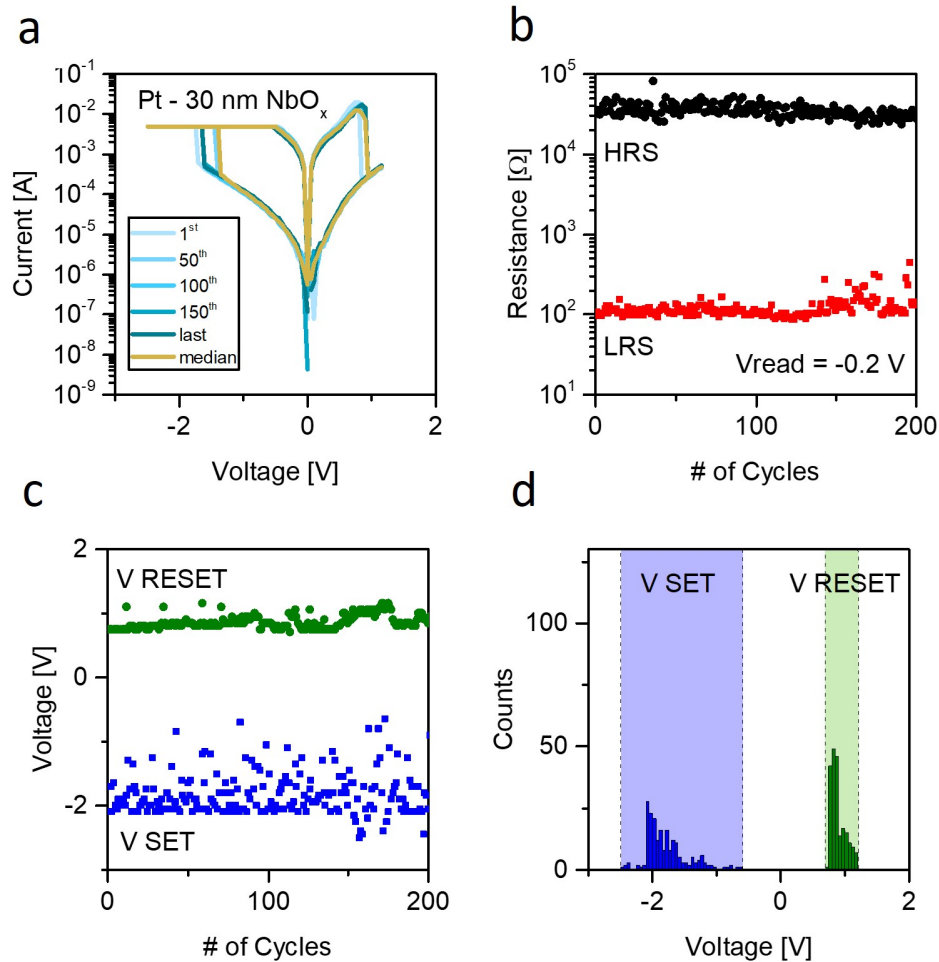
Fig. 3.14 RS behaviour in Pt/30 nm-NbO$_x$/Nb devices.a) Endurance test with exemplary. b) HRS and LRS collected for each cycle at the reading voltage V$_{read}$=−0.2 V. SET and RESET voltages cycle by cycle c) and distributed in histograms d).

In this last section, the RS behaviour of the Pt-terminated devices coupled with the 30 nm NbO$_x$ will be investigated. First of all, the typical the endurance test of a single device will be analysed. Since this is part of a general experiment involving different TE material, the endurance test has been stopped once 200 cycles have been reached, with the possibility of the cell switching between

the HRS and the LRS. In the plot a of Fig. 3.14 the typical *I-V* curves of the endurance test have been reported, at specific sample cycles (the first, the 50th, the 10050th, the 15050th and, the last 20050th cycle). The median has been superimposed as statistical discriminant of the 200 curves showing good superimposition and so, low variability cycle by cycle. Fig. 3.14b shows how the HRS and the LRS distribute cycle by cycle: there is a large bias window characterised by a stable HRS and a less stable LRS, especially in the last part of the experiment, but the cell was still able to switch without any problem. The resistances have been directly read at the $V_{read}=-0.2\,V$, has in the previous experiments. The endurance test was then completed by studying the variability of the SET and the RESET voltages. Figg. 3.14c-d show the high variability in the SET voltage which is however distributed toward the high value $-2\,V$, and the low variability in the RESET voltage close to $1\,V$. It seems that the RESET voltage increases a little bit from the second half of the experiment, and this is reflected in such a way with the high variability in the SET voltage and in the LRS.

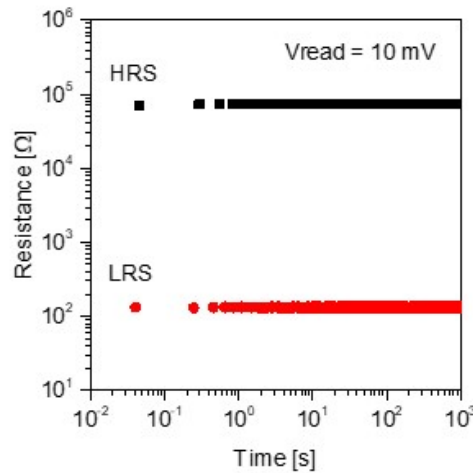Fig. 3.15 Retention experiment for the Pt terminated device under test. Differently from the Au terminated devices analysed in the previous chapter, the test cannot last over 10^3 s.

As analysed for the $60\,nm$ NbO_x devices terminated with Au, in this case, the retention has been studied for the Pt terminated device under test. Differently

from the Au-terminated devices, the retention test for the Pt devices last after 1000 s as shown in Fig. 3.15, meaning the Pt terminated devices have a lower capability to retain their resistance state, but at the same time, the Pt-terminated devices are the only ones working in a good way when the thickness of the oxide is reduced by the half.
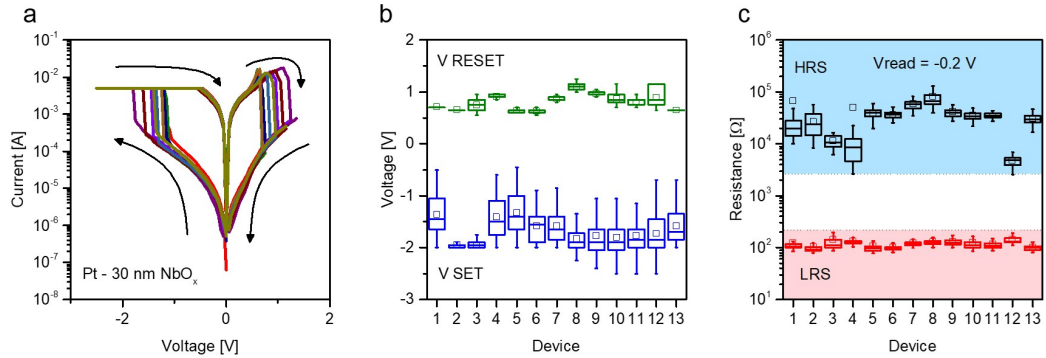
Fig. 3.16 Device-device variability for the 30 nm Pt-terminated devices: a) medians related to 13 endurance tested devices. Box-plot of the SET and RESET voltages b) and the HRS and LRS c) of the same devices.

The device-to-device variability was studied for the 30 nm Pt-terminated devices. Here in the plot, 13 exemplary devices have been analysed. Of the studied devices, only the ones achieved at least 50 cycles have been considered, the medians evaluated for each device and considering all the 50 *I-V* curves are collected in Fig. 3.16a: here it is possible to observe that, apart a variation in the SET and RESET voltages, the curves in the HRS and in the LRS are well superimposed, this is demonstrated by the very small variation in the box-plots related to the LRS in Fig. 3.16c, whilst for the HRS great variation exists. A bias window is present, even if, compared with the one of the single devices is not so large, but the two states can be definitively be distinguished. Fig. 3.16b completes the device-to-device variability analysis showing how the SET and the RESET voltages statistically vary. What is evident, is the large variation in terms of the SET voltage, that distribute almost toward the maximum negative voltage for this experiment that is −2.5 V and that is subjected to a variability of more than 1 V. For the RESET voltage, the maximum allowed voltage to have bipolar switching was set no larger than 1.2 V, to avoid the SET in the positive polarity. The RESET voltage distribution is characterised by a smaller

variability and in mean value is around 1 V, compatible with the one of the Au terminated devices (both oxide thicknesses).

In conclusion, the Pt terminated devices are the only one characterised by good switching properties if the size of the oxide layer is reduced by the half and the TE area is kept constant.

3.7 General design rule for the VCM cell based on NbO$_x$

To conclude the analysis of the different materials used as TE and the different oxide thicknesses, the following conclusions can be deduced:

- For the 60 nm NbO$_x$ devices, Au is the best choice to guarantee endurances over 1000 cycles and retentions of at least 10 000 s.

- For the 30 nm NbO$_x$ devices, Pt is the best choice. For the endurance at least 200 cycle reached, whilst the retention lasts not over 1000 s.

- Ir has an unstable behaviour and probably requires controlled environmental conditions to be properly studied, this means find a proper temperature and moisture range in which these cells can switch.

- TiN and Nb cannot be used to realise bipolar VCM cell having Ohmic contacts on both the electrode interfaces, whilst it is experimentally demonstrated the necessity to have materials and barriers asymmetry in the cell, with an Ohmic contact on one side and a Schottky contact on the other one.

This conclusions do not exclude the possibility to exploit Au and Ir at reduced oxide thicknesses, but on the basis of the previous experiments, it is not possible to use them keeping the TE area constant. For this reason it is necessary to work varying another parameter along side the oxide layer thickness when a scaling of the device must be performed keeping good switching properties.

Chapter 4

Conclusions and Perspectives

In the previous macro chapters memristive devices based on anodic NbO_x have been realised. In the chapter 2 it has been extensively shown how, starting from sputtered Nb on the top of a SiO_2 sample it was possible to grown the oxide layer through the anodic oxidation process and how in its simplicity, this manufacturing procedure was able to nano-metrically control the thickness of the oxide layer by fixing the anodizing voltage, or the voltage use to grow the oxide. Then material characterizations have been performed to study the properties of the grown oxide in terms of chemical, structural and morphological properties, useful for the next description of the switching properties in the NbO_x devices.

In the same chapter, the effect of Au as TE material was studied in the $Au/(60\,nm)NbO_x/Nb$ devices showing through simple test usually performed to preliminary study a memristive device, that the $50{\times}50\,\mu m^2$ devices are characterised by high endurances over 1000 cycles, low operating and symmetrical voltages ($-0.6\,V$ and $0.6\,V$ for the SET and RESET respectively) and good retention ($>10\,000\,s$). In addition, through slow voltage and current sweeps measurements performed on the SET process, it was possible to show quantization effects in terms of the current and so of the associated conductance of the cell. Although, the results on the quantum conductance steps are preliminary andfurther work is necessary to better understand the relationship between quantum conductance effects, involved materials and operating conditions.

In the chapter 3, different TE materials have been compared in order to find a proper selection rule when it comes to select a material for the realisation of

vertical device like the ones proposed. Obviously the conclusions found in this chapter refer to the specific structure obtained when one of the proposed material terminate the anodic NbO_x. In doing this, the first important conclusion concerned the switching capability of the NbO_x, that is only possible when the structure is asymmetric from the contacts point of view, meaning that is preferable an Ohmic contact on one side and a Schottky contact on the other side, otherwise is impossible to make the NbO_x switching and/or doing it in a stable way. The second conclusion is regarding the selection of the material basing on the thickness of the grown oxide layer. For the thicker oxide (60 nm), Au confirmed to be the best choice in terms of RS properties. For the thinner oxide (30 nm), results show that Pt-based devices are characterized by better performances, but with RS properties slightly worst rather than the previous devices.

Among the studied materials, there is the case of Ir, that showed strange and unstable switching behaviour, probably due to the variability in the environmental condition at which this material seems to be sensitive.

To conclude, when the oxide thickness is reduced, is still possible to induce bipolar switching in the NbO_x layer, but if the size of the TE is kept constant, only Pt seems to be the good candidate in the realisation of memristive devices based on NbO_x. In order to achieve a better scaling rule, is necessary to study, jointly to the oxide layer thickness reduction, the TE size one.

4.1 Future perspectives

In the literature it is largely showed that the performances of the RS devices increases with the scaling, being the volume interested by the switching sensibly reduced and at the same time the size of the filament at the basis of the switching contained.[109] In order to implement this feature and at the same time take advantage on the scaling, it is necessary to act reducing the TE area, and the best way is exploiting a different design architecture as the cross-point one. The main advantage of this architecture stays in the fact it is possible to confine the area by inducing the oxidation in a small region that is not directly tested with the tips of the instrument, making in this way possible to measure a small device, but far from the region of the switching, avoiding some damages

or device destruction due to the mechanical action of the tip contact. In this way, it will be possible to test the effect of Au and Pt at reduced dimensions. This design will be useful to study effect in quantization of the conductance, observed in chapter 2, but not perfectly investigated. The idea is to find proper programming conditions to make NbO_x devices switching in stable way in the quantum conductance regime.

If this will be possible, the next step will be the morphological analysis of the channel to finally establish the link between the generation of a quantum point contact and the electrical measurement, and up to now, the exploitation of memristive devices is one of the ways in which it is possible to realise nano-metric structures of so reduced dimensions, being the conventional fabrication techniques unable to satisfy this needing.

Another interesting field that can be investigated starting from the morphological analysis of nano-metric channels, is the study of the superconducting properties of Nb at extreme scaling conditions: it know that Nb is a superconducting material and its superconducting properties are demonstrated to degradate in the passage from the bulk Nb to the 2D one [110]. Up to now, the study of 2D-1D crossover is still under discussion and the exploitation of the memristive devices based on NbO_x can offer the possibility to overcome the limitation in the technology to study the superconducting properties in nano-scaled Nb structures 1D-like. Alongside to the study of the VCM cells based on NbO_x, the study of the ECM effect can be investigated exploiting mobile ions materials such as Ag and Cu (and others), in order to have a complete study of both the main effect related to the REDOX base switching.

References

[1] John Shalf. The future of computing beyond moore's law. *Philosophical Transactions of the Royal Society A*, 378(2166):20190061, 2020.

[2] Jerry Wu, Yin-Lin Shen, Kitt Reinhardt, Harold Szu, and Boqun Dong. A nanotechnology enhancement to moore's law. *Applied Computational Intelligence and Soft Computing*, 2013:2–2, 2013.

[3] Xingqi Zou, Sheng Xu, Xiaoming Chen, Liang Yan, and Yinhe Han. Breaking the von neumann bottleneck: architecture-level processing-in-memory technology. *Science China Information Sciences*, 64(6):160404, 2021.

[4] Jintao Yu, Hoang Anh Du Nguyen, Lei Xie, Mottaqiallah Taouil, and Said Hamdioui. Memristive devices for computation-in-memory. In *2018 Design, Automation & Test in Europe Conference & Exhibition (DATE)*, pages 1646–1651. IEEE, 2018.

[5] Hoang Anh Du Nguyen, Jintao Yu, Lei Xie, Mottaqiallah Taouil, Said Hamdioui, and Dietmar Fey. Memristive devices for computing: Beyond cmos and beyond von neumann. In *2017 IFIP/IEEE International Conference on Very Large Scale Integration (VLSI-SoC)*, pages 1–10. IEEE, 2017.

[6] Leon Chua. Memristor-the missing circuit element. *IEEE Transactions on circuit theory*, 18(5):507–519, 1971.

[7] Leon O Chua and Sung Mo Kang. Memristive devices and systems. *Proceedings of the IEEE*, 64(2):209–223, 1976.

[8] Leon Chua. If it's pinched it'sa memristor. *Semiconductor Science and Technology*, 29(10):104001, 2014.

[9] Dmitri B Strukov, Gregory S Snider, Duncan R Stewart, and R Stanley Williams. The missing memristor found. *nature*, 453(7191):80–83, 2008.

[10] TW Hickmott. Electroluminescence, bistable switching, and dielectric breakdown of nb 2 o 5 diodes. *Journal of Vacuum Science and Technology*, 6(5):828–833, 1969.

[11] Rainer Waser and Masakazu Aono. Nanoionics-based resistive switching memories. *Nature materials*, 6(11):833–840, 2007.

[12] An Chen, Sameer Haddad, Yi-Ching Wu, Tzu-Ning Fang, Zhida Lan, S Avanzino, S Pangrle, M Buynoski, M Rathor, Wei Cai, et al. Non-volatile resistive switching for advanced memory applications. In *IEEE InternationalElectron Devices Meeting, 2005. IEDM Technical Digest.*, pages 746–749. IEEE, 2005.

[13] Chih-Yang Lin, Chen-Yu Wu, Chung-Yi Wu, Chenming Hu, and Tseung-Yuen Tseng. Bistable resistive switching in al2o3 memory thin films. *Journal of the Electrochemical Society*, 154(9):G189, 2007.

[14] DC Kim, S Seo, SE Ahn, D-S Suh, MJ Lee, B-H Park, IK Yoo, IG Baek, H-J Kim, EK Yim, et al. Electrical observations of filamentary conductions for the resistive memory switching in nio films. *Applied physics letters*, 88(20), 2006.

[15] Masanori Hosomi, H Yamagishi, T Yamamoto, Kazuhiro Bessho, Yutaka Higo, Kazutaka Yamane, H Yamada, M Shoji, Hiroaki Hachino, C Fukumoto, et al. A novel nonvolatile memory with spin torque transfer magnetization switching: Spin-ram. In *IEEE InternationalElectron Devices Meeting, 2005. IEDM Technical Digest.*, pages 459–462. IEEE, 2005.

[16] Zhongrui Wang, Huaqiang Wu, Geoffrey W Burr, Cheol Seong Hwang, Kang L Wang, Qiangfei Xia, and J Joshua Yang. Resistive switching materials for information processing. *Nature Reviews Materials*, 5(3):173–195, 2020.

[17] Saied Tehrani, Jon M Slaughter, Mark Deherrera, Brad N Engel, Nicholas D Rizzo, John Salter, Mark Durlam, Renu W Dave, Jason Janesky, Brian Butcher, et al. Magnetoresistive random access memory using magnetic tunnel junctions. *Proceedings of the IEEE*, 91(5):703–714, 2003.

[18] Rainer Waser, Stephan Menzel, and Vikas Rana. Recent progress in redox-based resistive switching. In *2012 IEEE International Symposium on Circuits and Systems (ISCAS)*, pages 1596–1599. IEEE, 2012.

[19] Regina Dittmann, Stephan Menzel, and Rainer Waser. Nanoionic memristive phenomena in metal oxides: the valence change mechanism. *Advances in physics*, 70(2):155–349, 2021.

[20] Felix Cüppers, S Menzel, C Bengel, A Hardtdegen, M Von Witzleben, U Böttger, R Waser, and S Hoffmann-Eifert. Exploiting the switching dynamics of hfo2-based reram devices for reliable analog memristive behavior. *APL materials*, 7(9), 2019.

[21] E Linn, S Menzel, S Ferch, and R Waser. Compact modeling of crs devices based on ecm cells for memory, logic and neuromorphic applications. *Nanotechnology*, 24(38):384008, 2013.

[22] Ilia Valov, Rainer Waser, John R Jameson, and Michael N Kozicki. Electrochemical metallization memories—fundamentals, applications, prospects. *Nanotechnology*, 22(25):254003, 2011.

[23] Daniele Ielmini, Rainer Bruchhaus, and Rainer Waser. Thermochemical resistive switching: materials, mechanisms, and scaling projections. *Phase Transitions*, 84(7):570–602, 2011.

[24] Philip Bartlett, Alexandra I Berg, Marco Bernasconi, Simon Brown, Geoffrey Burr, Cina Foroutan-Nejad, Ella Gale, Ruomeng Huang, Daniele Ielmini, Gabriela Kissling, et al. Phase-change memories (pcm)–experiments and modelling: General discussion. *Faraday discussions*, 213:393–420, 2019.

[25] Kyung Min Kim, Doo Seok Jeong, and Cheol Seong Hwang. Nanofilamentary resistive switching in binary oxide system; a review on the present status and outlook. *Nanotechnology*, 22(25):254002, 2011.

[26] Ilia Valov and Wei D Lu. Nanoscale electrochemistry using dielectric thin films as solid electrolytes. *Nanoscale*, 8(29):13828–13837, 2016.

[27] Rainer Waser. Redox-based resistive switching memories. *Journal of nanoscience and nanotechnology*, 12(10):7628–7640, 2012.

[28] MJ Rozenberg, Maria Jose Sanchez, Ruben Weht, Carlos Acha, Fernando Gomez-Marlasca, and Pablo Levy. Mechanism for bipolar resistive switching in transition-metal oxides. *Physical Review B*, 81(11):115101, 2010.

[29] Wen-Yuan Chang, Yen-Chao Lai, Tai-Bor Wu, Sea-Fue Wang, Frederick Chen, and Ming-Jinn Tsai. Unipolar resistive switching characteristics of zno thin films for nonvolatile memory applications. *Applied Physics Letters*, 92(2), 2008.

[30] Doo Seok Jeong, Herbert Schroeder, and Rainer Waser. Coexistence of bipolar and unipolar resistive switching behaviors in a pt/ tio2/ pt stack. *Electrochemical and solid-state letters*, 10(8):G51, 2007.

[31] MWP Carney, TKN Chary, T Bottiglieri, and EH Reynolds. The switch mechanism and the bipolar/unipolar dichotomy. *The British Journal of Psychiatry*, 154(1):48–51, 1989.

[32] Mario Lanza, H-S Philip Wong, Eric Pop, Daniele Ielmini, Dimitri Strukov, Brian C Regan, Luca Larcher, Marco A Villena, J Joshua Yang, Ludovic Goux, et al. Recommended methods to study resistive switching devices. *Advanced Electronic Materials*, 5(1):1800143, 2019.

[33] Jun Yeong Seok, Seul Ji Song, Jung Ho Yoon, Kyung Jean Yoon, Tae Hyung Park, Dae Eun Kwon, Hyungkwang Lim, Gun Hwan Kim, Doo Seok Jeong, and Cheol Seong Hwang. A review of three-dimensional resistive switching cross-bar array memories from the integration and materials property points of view. *Advanced Functional Materials*, 24(34):5316–5339, 2014.

[34] Daniele Ielmini, Carlo Cagli, Federico Nardi, and Y Zhang. Nanowire-based resistive switching memories: devices, operation and scaling. *Journal of Physics D: Applied Physics*, 46(7):074006, 2013.

[35] M Lanza, G Bersuker, M Porti, Enrique Miranda, M Nafría, and X Aymerich. Resistive switching in hafnium dioxide layers: Local phenomenon at grain boundaries. *Applied Physics Letters*, 101(19), 2012.

[36] HY Lee, PS Chen, TY Wu, YS Chen, CC Wang, PJ Tzeng, CH Lin, F Chen, CH Lien, and M-J Tsai. Low power and high speed bipolar switching with a thin reactive ti buffer layer in robust hfo2 based rram. In *2008 IEEE International Electron Devices Meeting*, pages 1–4. IEEE, 2008.

[37] Andrea Zaffora, Roberto Macaluso, Hiroki Habazaki, Ilia Valov, and Monica Santamaria. Electrochemically prepared oxides for resistive switching devices. *Electrochimica Acta*, 274:103–111, 2018.

[38] A Zaffora, F Di Quarto, H Habazaki, I Valov, and M Santamaria. Electrochemically prepared oxides for resistive switching memories. *Faraday Discussions*, 213:165–181, 2019.

[39] Sungho Kim, Hanul Moon, Dipti Gupta, Seunghyup Yoo, and Yang-Kyu Choi. Resistive switching characteristics of sol–gel zinc oxide films for flexible memory applications. *IEEE Transactions on Electron Devices*, 56(4):696–699, 2009.

[40] Shuang Gao, Xiaohui Yi, Jie Shang, Gang Liu, and Run-Wei Li. Organic and hybrid resistive switching materials and devices. *Chemical Society Reviews*, 48(6):1531–1565, 2019.

[41] Hung-Ju Yen and Guey-Sheng Liou. Solution-processable triarylamine-based high-performance polymers for resistive switching memory devices. *Polymer Journal*, 48(2):117–138, 2016.

[42] Maria Vittoria Diamanti, Riccardo Pisoni, Andrea Cologni, Andrea Brenna, Fernando Corinto, and MariaPia Pedeferri. Anodic oxidation as a means to produce memristive films. *Journal of Applied Biomaterials & Functional Materials*, 14(3):e290–e295, 2016.

[43] Po-Hsun Chen, Chih-Yang Lin, Ting-Chang Chang, Jason K Eshraghian, Yu-Ting Chao, Wei D Lu, and Simon M Sze. Investigating selectorless

property within niobium devices for storage applications. *ACS Applied Materials & Interfaces*, 14(1):2343–2350, 2022.

[44] Suhas Kumar, Noraica Davila, Ziwen Wang, Xiaopeng Huang, John Paul Strachan, David Vine, AL David Kilcoyne, Yoshio Nishi, and R Stanley Williams. Spatially uniform resistance switching of low current, high endurance titanium–niobium-oxide memristors. *Nanoscale*, 9(5):1793–1798, 2017.

[45] Sweety Deswal, Ashok Kumar, and Ajeet Kumar. Nbox based memristor as artificial synapse emulating short term plasticity. *AIP Advances*, 9(9), 2019.

[46] Joshua C Shank, M Brooks Tellekamp, Matthew J Wahila, Sebastian Howard, Alex S Weidenbach, Bill Zivasatienraj, Louis FJ Piper, and W Alan Doolittle. Scalable memdiodes exhibiting rectification and hysteresis for neuromorphic computing. *Scientific reports*, 8(1):12935, 2018.

[47] Suhas Kumar, R Stanley Williams, and Ziwen Wang. Third-order nanocircuit elements for neuromorphic engineering. *Nature*, 585(7826):518–523, 2020.

[48] Melanie Herzig, Martin Weiher, Alon Ascoli, Ronald Tetzlaff, Thomas Mikolajick, and Stefan Slesazeck. Multiple slopes in the negative differential resistance region of nbox-based threshold switches. *Journal of Physics D: Applied Physics*, 52(32):325104, 2019.

[49] Thomas Mikolajick, Melanie Herzig, Stefan Slesazeck, Martin Weiher, Alon Ascoli, and Ronald Tetzlaff. Optimization and application of niobium oxide based memristive ndr devices. In *2021 17th International Workshop on Cellular Nanoscale Networks and their Applications (CNNA)*, pages 1–4. IEEE, 2021.

[50] Alon Ascoli, Martin Weiher, Ronald Tetzlaff, Melanie Herzig, Stefan Slesazeck, and Thomas Mikolajick. Control strategies to optimize graph coloring via m-cnns with locally-active nbo x memristors. In *2021 10th International Conference on Modern Circuits and Systems Technologies (MOCAST)*, pages 1–8. IEEE, 2021.

[51] Melanie Herzig, Martin Weiher, Alon Ascoli, Ronald Tetzlaff, Thomas Mikolajick, and Stefan Slesazeck. Improvement of nbox-based threshold switching devices by implementing multilayer stacks. *Semiconductor Science and Technology*, 34(7):075005, 2019.

[52] Hannes Mähne, Helge Wylezich, Stefan Slesazeck, Thomas Mikolajick, Jozef Vesely, Volker Klemm, and David Rafaja. Room temperature fabricated nbo x/nb 2 o 5 memory switching device with threshold switching effect. In *2013 5th IEEE International Memory Workshop*, pages 174–177. IEEE, 2013.

[53] Thomas Mikolajick, H Wylezich, Hannes Maehne, and Stefan Slesazeck. Versatile resistive switching in niobium oxide. In *2016 IEEE International Symposium on Circuits and Systems (ISCAS)*, pages 381–384. IEEE, 2016.

[54] S Slesazeck, M Herzig, T Mikolajick, A Ascoli, M Weiher, and R Tetzlaff. Analysis of v th variability in nbo x-based threshold switches. In *2016 16th Non-Volatile Memory Technology Symposium (NVMTS)*, pages 1–5. IEEE, 2016.

[55] Helge Wylezich, Hannes Mahne, Jura Rensberg, Carsten Ronning, Peter Zahn, Stefan Slesazeck, and Thomas Mikolajick. Local ion irradiation-induced resistive threshold and memory switching in nb2o5/nbo x films. *ACS applied materials & interfaces*, 6(20):17474–17480, 2014.

[56] Stefan Slesazeck, H Wylezich, and Thomas Mikolajick. Analog memristive and memcapacitive properties of ti/ai 2 o 3/nb 2 o 5/ti resistive switches. In *2017 IEEE 8th Latin American Symposium on Circuits & Systems (LASCAS)*, pages 1–4. IEEE, 2017.

[57] Alon Ascoli, Ronald Tetzlaff, Stefan Slesazeck, Hannes Mähne, and Thomas Mikolajick. Stability analysis supports memristor circuit design. In *2015 IEEE International Symposium on Circuits and Systems (ISCAS)*, pages 1138–1141. IEEE, 2015.

[58] A Ascoli, S Slesazeck, H Mahne, R Tetzlaff, and T Mikolajick. Unfolding principle gives insight into physics behind threshold switching in a nbo memristor. In *2015 International Conference on Memristive Systems (MEMRISYS)*, pages 1–3. IEEE, 2015.

[59] Dong Su Jeon, Tukaram D Dongale, and Tae Geun Kim. Low power ti-doped nbo2-based selector device with high selectivity and low off current. *Journal of Alloys and Compounds*, 884:161041, 2021.

[60] Xinjun Liu, Sharif Md Sadaf, Sangsu Park, Seonghyun Kim, Euijun Cha, Daeseok Lee, Gun-Young Jung, and Hyunsang Hwang. Complementary resistive switching in niobium oxide-based resistive memory devices. *IEEE electron device letters*, 34(2):235–237, 2013.

[61] Ziliang Zhou, Mei Yang, Zhen Fu, Hong Wang, Xiaohua Ma, and Haixia Gao. Electrode-induced polarity conversion in nb2o5/nbox resistive switching devices. *Applied Physics Letters*, 117(24), 2020.

[62] Jamal Aziz, Honggyun Kim, Shania Rehman, Muhammad Farooq Khan, and Deok-kee Kim. Chemical nature of electrode and the switching response of rf-sputtered nbox films. *Nanomaterials*, 10(11):2164, 2020.

[63] Kyooho Jung, Yongmin Kim, Young S Park, Woong Jung, Jungae Choi, Baeho Park, Hyungsang Kim, Wondong Kim, Jinpyo Hong, and Hyunsik Im. Unipolar resistive switching in insulating niobium oxide film and

probing electroforming induced metallic components. *Journal of Applied Physics*, 109(5), 2011.

[64] Lin Chen, Qing-Qing Sun, Jing-Jing Gu, Yan Xu, Shi-Jin Ding, and David Wei Zhang. Bipolar resistive switching characteristics of atomic layer deposited nb2o5 thin films for nonvolatile memory application. *Current Applied Physics*, 11(3):849–852, 2011.

[65] Hyunhee Baek, Chanwoo Lee, Jungkyu Choi, and Jinhan Cho. Nonvolatile memory devices prepared from sol–gel derived niobium pentoxide films. *Langmuir*, 29(1):380–386, 2013.

[66] Ivana Zrinski, Marvin Löfler, Janez Zavašnik, Claudia Cancellieri, Lars PH Jeurgens, Achim Walter Hassel, and Andrei Ionut Mardare. Impact of electrolyte incorporation in anodized niobium on its resistive switching. *Nanomaterials*, 12(5):813, 2022.

[67] Tulina, Rossolenko, Borisenko, Shmytko, Ionov, and Ivanov. Realization of rectifying and resistive switching behaviors of mesoscopic niobium oxide-based structures. *Materials Letters*, 136:404–406, 2014.

[68] Tatyana V Kundozerova, Alexander M Grishin, GB Stefanovich, and AA Velichko. Anodic nb2o5 nonvolatile rram. *IEEE Transactions on electron devices*, 59(4):1144–1148, 2012.

[69] Tatyana V Kundozerova, Genrikch B Stefanovich, and Alexander M Grishin. Binary anodic oxides for memristor-type nonvolatile memory. *physica status solidi c*, 9(7):1699–1701, 2012.

[70] Giuseppe Leonetti, Matteo Fretto, Katarzyna Bejtka, Elena Sonia Olivetti, Fabrizio Candido Pirri, Natascia De Leo, Ilia Valov, and Gianluca Milano. Resistive switching and role of interfaces in memristive devices based on amorphous nbo x grown by anodic oxidation. *Physical Chemistry Chemical Physics*, 25(21):14766–14777, 2023.

[71] JM Albella, I Montero, O Sanchez, and JM Martínez-Duart. Theoretical approach for the constant voltage stage in anodic oxidation. *Journal of the Electrochemical Society*, 133(5):876, 1986.

[72] G Ramírez, SE Rodil, S Muhl, D Turcio-Ortega, JJ Olaya, M Rivera, E Camps, and L Escobar-Alarcón. Amorphous niobium oxide thin films. *Journal of non-crystalline Solids*, 356(50-51):2714–2721, 2010.

[73] DM Lakhiani and LL Shreir. Crystallization of amorphous niobium oxide during anodic oxidation. *Nature*, 188(4744):49–50, 1960.

[74] Runzhe Tao, Ruzica Todorovic, Jingjing Liu, Randall J Meyer, Andrew Arnold, Weronika Walkosz, Peter Zapol, Alexander Romanenko, Lance D Cooley, and Robert F Klie. Electron energy-loss spectroscopy study of metallic nb and nb oxides. *Journal of Applied Physics*, 110(12), 2011.

[75] M Grundner and J Halbritter. Xps and aes studies on oxide growth and oxide coatings on niobium. *Journal of Applied Physics*, 51(1):397–405, 1980.

[76] Claudio Nico, T Monteiro, and Manuel PF Graça. Niobium oxides and niobates physical properties: Review and prospects. *Progress in Materials Science*, 80:1–37, 2016.

[77] Enrique Miranda, Gianluca Milano, and Carlo Ricciardi. Compact modeling of the iv characteristics of zno nanowires including nonlinear series resistance effects. *IEEE Transactions on Nanotechnology*, 19:297–300, 2020.

[78] Gianluca Milano, Michael Luebben, Zheng Ma, Rafal Dunin-Borkowski, Luca Boarino, Candido F Pirri, Rainer Waser, Carlo Ricciardi, and Ilia Valov. Self-limited single nanowire systems combining all-in-one memristive and neuromorphic functionalities. *Nature communications*, 9(1):5151, 2018.

[79] Yuan Liu, Jian Guo, Enbo Zhu, Lei Liao, Sung-Joon Lee, Mengning Ding, Imran Shakir, Vincent Gambin, Yu Huang, and Xiangfeng Duan. Approaching the schottky–mott limit in van der waals metal–semiconductor junctions. *Nature*, 557(7707):696–700, 2018.

[80] Carlos Moncasi, Gauthier Lefèvre, Quentin Villeger, Laetitia Rapenne, Hervé Roussel, Ahmad Bsiesy, Carmen Jiménez, and Mónica Burriel. Structural defects improve the memristive characteristics of epitaxial la0. 8sr0. 2mno3-based devices. *Advanced Materials Interfaces*, 9(23):2200498, 2022.

[81] James H Stathis. Percolation models for gate oxide breakdown. *Journal of applied physics*, 86(10):5757–5766, 1999.

[82] Krzysztof Szot, Wolfgang Speier, Gustav Bihlmayer, and Rainer Waser. Switching the electrical resistance of individual dislocations in single-crystalline srtio3. *Nature materials*, 5(4):312–320, 2006.

[83] SB Lee, HK Yoo, Seo Hyoung Chang, LG Gao, BS Kang, M-J Lee, CJ Kim, and TW Noh. Time-dependent current-voltage curves during the forming process in unipolar resistance switching. *Applied Physics Letters*, 98(5), 2011.

[84] Abhishek A Sharma, Ilya V Karpov, Roza Kotlyar, Jonghan Kwon, Marek Skowronski, and James A Bain. Dynamics of electroforming in binary metal oxide-based resistive switching memory. *Journal of Applied Physics*, 118(11), 2015.

[85] Doo Seok Jeong, Herbert Schroeder, Uwe Breuer, and Rainer Waser. Characteristic electroforming behavior in pt/tio2/pt resistive switching cells depending on atmosphere. *Journal of applied physics*, 104(12), 2008.

[86] H Habazaki, T Matsuo, H Konno, K Shimizu, S Nagata, K Matsumoto, K Takayama, Y Oda, P Skeldon, and GE Thompson. Influence of silicon species on the electric properties of anodic niobia. *Electrochimica acta*, 48(23):3519–3526, 2003.

[87] JPS Pringle. The anodic oxidation of superimposed metallic layers: theory. *Electrochimica Acta*, 25(11):1423–1437, 1980.

[88] JA Davies, B Domeij, JPS Pringle, and F Brown. The migration of metal and oxygen during anodic film formation. *Journal of the Electrochemical Society*, 112(7):675, 1965.

[89] Min-Kyu Song, Ji-Hoon Kang, Xinyuan Zhang, Wonjae Ji, Alon Ascoli, Ioannis Messaris, Ahmet Samil Demirkol, Bowei Dong, Samarth Aggarwal, Weier Wan, et al. Recent advances and future prospects for memristive materials, devices, and systems. *ACS nano*, 17(13):11994–12039, 2023.

[90] Stephan Menzel and Ji-Hyun Hur. Modeling the vcm-and ecm-type switching kinetics. *Resistive Switching: From Fundamentals of Nanoionic Redox Processes to Memristive Device Applications*, pages 395–436, 2016.

[91] Sheng-Yu Wang, Chin-Wen Huang, Dai-Ying Lee, Tseung-Yuen Tseng, and Ting-Chang Chang. Multilevel resistive switching in ti/cuxo/pt memory devices. *Journal of Applied Physics*, 108(11), 2010.

[92] Tae-Hyeon Kim, Sungjoon Kim, Kyungho Hong, Jinwoo Park, Yeongjin Hwang, Byung-Gook Park, and Hyungjin Kim. Multilevel switching memristor by compliance current adjustment for off-chip training of neuromorphic system. *Chaos, Solitons & Fractals*, 153:111587, 2021.

[93] Sang-Jun Choi, Jung-Hyun Lee, Hyung-Jin Bae, Woo-Young Yang, Tae-Wan Kim, and Ki-Hong Kim. Improvement of cbram resistance window by scaling down electrode size in pure-gete film. *IEEE electron device letters*, 30(2):120–122, 2008.

[94] Gianluca Milano, Masakazu Aono, Luca Boarino, Umberto Celano, Tsuyoshi Hasegawa, Michael Kozicki, Sayani Majumdar, Mariela Menghini, Enrique Miranda, Carlo Ricciardi, et al. Quantum conductance in memristive devices: fundamentals, developments, and applications. *Advanced Materials*, 34(32):2201248, 2022.

[95] Rolf Landauer. Conductance from transmission: common sense points. *Physica Scripta*, 1992(T42):110, 1992.

[96] Giuseppe Leonetti, Matteo Fretto, Fabrizio Candido Pirri, Natascia De Leo, Ilia Valov, and Gianluca Milano. Effect of electrode materials on resistive switching behaviour of nbox-based memristive devices. *Scientific Reports*, 13(1):17003, 2023.

[97] Ilia Valov and Tohru Tsuruoka. Effects of moisture and redox reactions in vcm and ecm resistive switching memories. *Journal of Physics D: Applied Physics*, 51(41):413001, 2018.

[98] Cong Ye, Jiaji Wu, Gang He, Jieqiong Zhang, Tengfei Deng, Pin He, and Hao Wang. Physical mechanism and performance factors of metal oxide based resistive switching memory: a review. *Journal of Materials Science & Technology*, 32(1):1–11, 2016.

[99] Benedict Ofuonye, Jaseun Lee, Minjun Yan, Changwoo Sun, Jian-Min Zuo, and Ilesanmi Adesida. Electrical and microstructural properties of thermally annealed ni/au and ni/pt/au schottky contacts on algan/gan heterostructures. *Semiconductor science and technology*, 29(9):095005, 2014.

[100] William M Haynes. *CRC handbook of chemistry and physics*. CRC press, 2014.

[101] LPBa Lima, JA Diniz, I Doi, and J Godoy Fo. Titanium nitride as electrode for mos technology and schottky diode: Alternative extraction method of titanium nitride work function. *Microelectronic Engineering*, 92:86–90, 2012.

[102] Bharti Singh and BR Mehta. Relationship between nature of metal-oxide contacts and resistive switching properties of copper oxide thin film based devices. *Thin Solid Films*, 569:35–43, 2014.

[103] Raymond T Tung. The physics and chemistry of the schottky barrier height. *Applied Physics Reviews*, 1(1), 2014.

[104] Wangping Wu, Zhaofeng Chen, and Liangbing Wang. Oxidation behavior of multilayer iridium coating on niobium substrate. *Protection of Metals and Physical Chemistry of Surfaces*, 51:607–612, 2015.

[105] An Chen. Area and thickness scaling of forming voltage of resistive switching memories. *IEEE electron device letters*, 35(1):57–59, 2013.

[106] Alexander C Kozen, Zachary R Robinson, Evan R Glaser, Mark Twigg, Thomas J Larrabee, Hans Cho, SM Prokes, and Laura B Ruppalt. In situ hydrogen plasma exposure for varying the stoichiometry of atomic layer deposited niobium oxide films for use in neuromorphic computing applications. *ACS applied materials & interfaces*, 12(14):16639–16647, 2020.

[107] E Sciri and R Chabicovsky. 2.19 conduction phenomena in nb-nb2o5-au thin film structures fabricated by various techniques. *Vacuum*, 27(4):299–304, 1977.

[108] Zhaoping Shi, Ji Li, Jiadong Jiang, Yibo Wang, Xian Wang, Yang Li, Liting Yang, Yuyi Chu, Jingsen Bai, Jiahao Yang, et al. Enhanced acidic water oxidation by dynamic migration of oxygen species at the ir/nb2o5-x catalyst/support interfaces. *Angewandte Chemie International Edition*, 61(52):e202212341, 2022.

[109] Mohammed A Zidan, John Paul Strachan, and Wei D Lu. The future of electronics based on memristive systems. *Nature electronics*, 1(1):22–29, 2018.

[110] Nicola Pinto, S Javad Rezvani, Andrea Perali, Luca Flammia, Milorad V Milošević, Matteo Fretto, Cristina Cassiago, and Natascia De Leo. Dimensional crossover and incipient quantum size effects in superconducting niobium nanofilms. *Scientific reports*, 8(1):4710, 2018.

Appendix A

Quantum Conductance steps observation

In the chapter 2 the possibility to observe quantum conductance steps through slow voltage and current measurements is shown. Nevertheless, this possibility has not been investigated in the detail. Here, further exemplary curves are shown demonstrating the possibility of the observation, but on the other hand, even the difficulty into program the devices under test to achieve a specific conductance output.
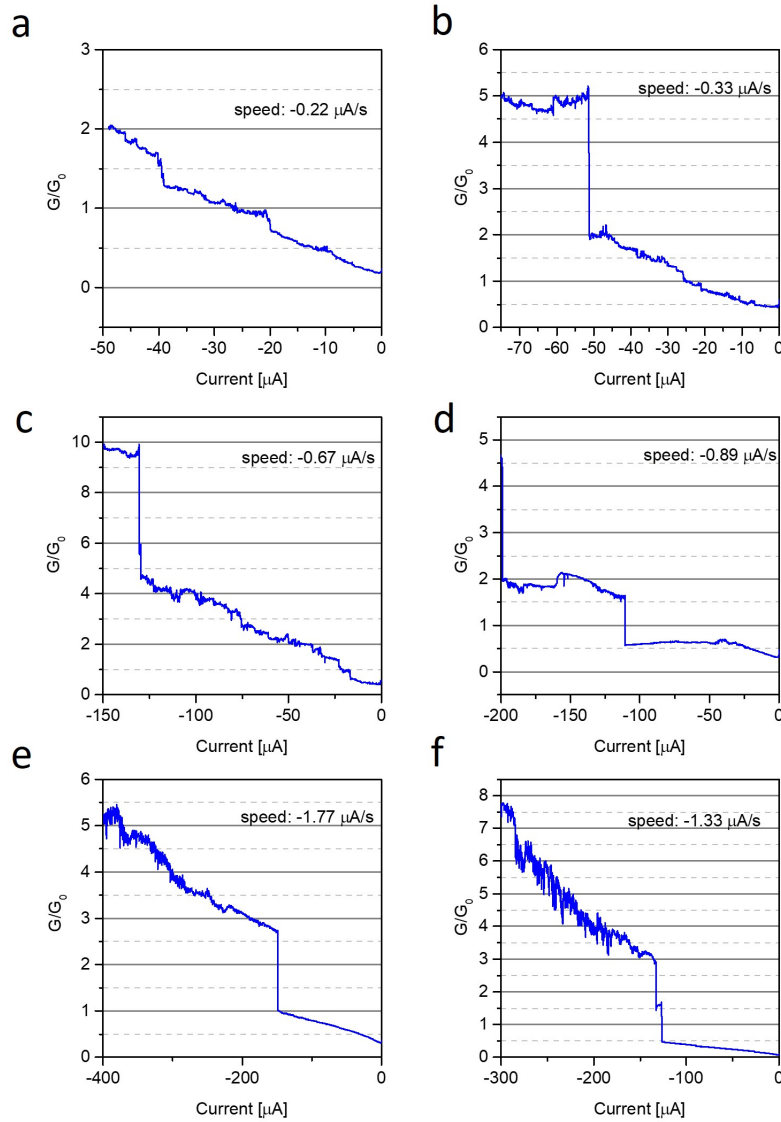
A.1 Slow current measurements

Fig. A.1 Slow current measurement at different maximum current in the SET phase: a)$-50\,\mu A$, b)$-75\,\mu A$, c)$-150\,\mu A$, d)$-200\,\mu A$, e)$-300\,\mu A$, and f)$-400\,\mu A$.

Fig. A.1a-f show the electrical response in terms of conductance when the devices under test are driven with different slow current stimuli during the SET operation. Here six different maximum currents are set for the experiment: $-50\,\mu A$, $-75\,\mu A$, $-150\,\mu A$, $-200\,\mu A$, $-300\,\mu A$, and $-400\,\mu A$. The sweep

speeds reported on the plots are fixed by the limitation in the instrument (Keithley 4200A scs parameter analyzer) which allows the acquisition of 4096 point for a single measurement run, so that, the corresponding speed is expected to reduce as soon the maximum current is reduced (in absolute value). This opens to different problems:

- the observation of quantum conductance steps is easier for lower sweep speeds

- for low sweep speeds few multiples of G_0 are accessible

- not clear step are always observables

- the process of quantum steps observation does not follow a real trend and can be considered almost random

A.2   Slow Voltage measurements

In this section similar measurements will be proposed, this time focusing the attention on the Voltage input and the possible conductance response of the Au terminated devices. This time, the investigation will be done for both the SET and the RESET process since the control of the exploited voltages stimuli are compatible with the SET and the RESET voltages of the devices.

A.2.1   Slow SET process
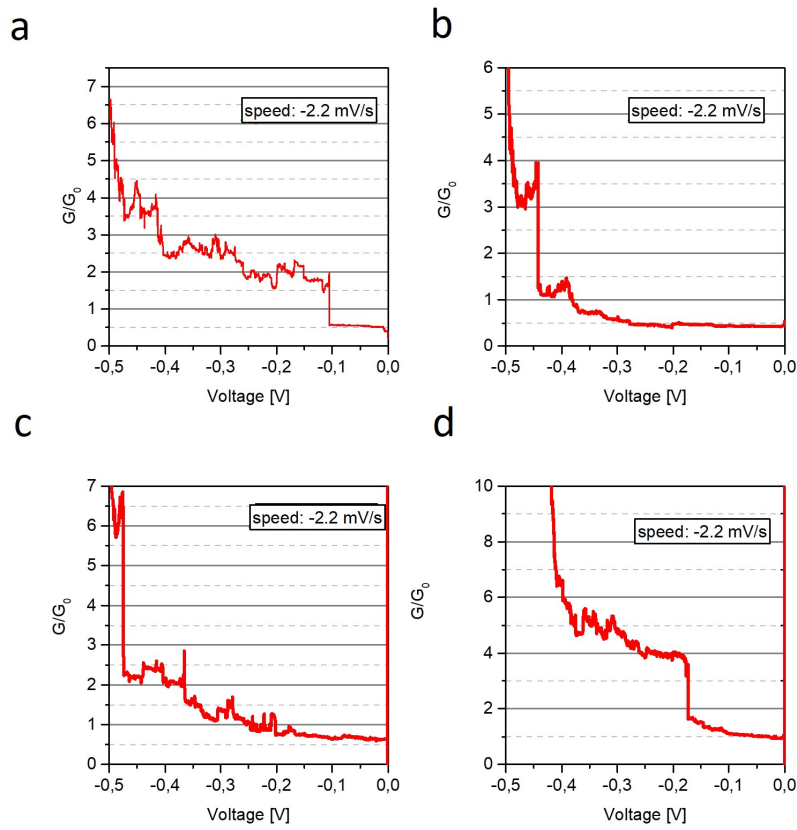

Fig. A.2 Exemplary curves related to a slow voltage experiment carried out during the SET operation assuming a maximum negative voltage of $-0.5\,\mathrm{V}$.

Similar problem are encountered even for the slow voltage experiment. As Fig. A.2 shows, even if the maximum applied voltage is the same and the corresponding voltage sweep speed is fixed, the observation of quantum conductance steps follows a random distribution.

A.2.2   Slow RESET process

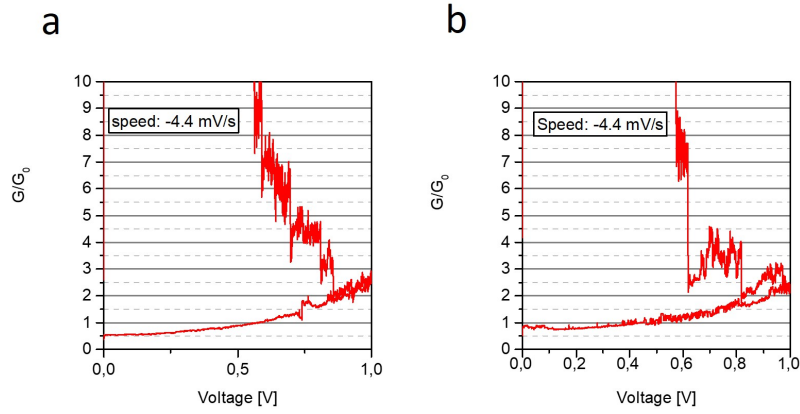a   b

Fig. A.3 Slow RESET process assuming a maximum voltage of 1 V.

For the slow RESET process a maximum positive voltage of 1 V is set up, considering the limitation in the instrument and the maximum number of acquirable points, the sweep speed in this case is doubled with respect to the one in the SET operation. Even in this case the observation of some steps in conductance is visible, but the measurements are really noisy.

To resume, the slow voltage and current measurements can be exploited to drive the Au-terminated devices with the main purpose of quantum steps observation. Nevertheless, this analysis should be intended to be only qualitative and not quantitative because the quantum steps observation follows an almost random distribution, in this sense we can talk about the probability of observation.